Monitoring of Subsea Tidal Energy Transmission Cable in the Minas Passage

by

Sean Campbell

Submitted in partial fulfilment of the requirements
for the degree of Masters of Applied Science

at

Dalhousie University
Halifax, Nova Scotia
December 2016

To my parents for all of their support

Table of Contents

List of Tables

List of Figures

Abstract

This study presents an analysis of measurements made from an orientation sensor placed in the subsea end of two tidal power subsea transmission cables deployed in the Minas Passage at the Fundy Ocean Research Centre for Energy tidal power test site. Monitoring the ends of the cables is important to ensure the stability of the ends seabed in the strong tidal environment. Movement of the cable ends could result in cable damage or reduced lifespan of the cables causing setbacks for operations at the tidal energy the test site. The sensor package was tested prior to deployment with the subsea transmission cables to determine the accuracy and expected variation of the orientation and accelerometer measurements. With this understanding of the expected variation of the sensor under static conditions, thresholds were selected to identify movement and changes of orientation of the cable abandonment terminations. Data collected from the sensor packages in the deployed cables indicates that the abandonment terminations of the two cables were stable on the seabed over the data collection period. Accelerometer measurements collected from one of the two cables indicated an impact to the abandonment termination but did not correspond to a change in orientation measurements.

List of Abbreviations and Symbols Used

Abbreviations

AHRS	Attitude and heading reference system
BOTDA	Brillouin Optical Time Domain Analysis
BOTDR	Brillouin Optical Time Domain Reflectometry
EMEC	European Marine Energy Centre
FBG	Fiber Bragg Grating
FORCE	Fundy Ocean Research Centre for Energy

Symbols

a	Acceleration (m/s^2)
a_{LCS}	Acceleration in sensor local coordinates (m/s^2)
a_{Earth}	Acceleration in earth coordinates (m/s^2)
A_x	Acceleration in x-axis (m/s^2)
A_y	Acceleration in y-axis (m/s^2)
A_z	Acceleration in z-axis (m/s^2)
d	Difference in measurements
$\bar{d}$	Mean of difference of measurements
DCM	Directional Cosine Matrix
g	Gravitational acceleration (m/s^2)
i	Cartesian x-axis unit vector
IRB	Accelerometer in-run bias stability (m/s^2)
j	Cartesian y-axis unit vector
k	Cartesian z-axis unit vector

n	Number of samples
q	Quaternion
s	Standard deviation of difference in measurements
SB	Accelerometer start up bias (m/s^2)
t	Time (s)
ΔT	Change in Temperature (°C)
U_A	Accelerometer uncertainty (m/s^2)
v_B	Brillouin frequency (Hz)
v_f	Final velocity (m/s)
v_i	Initial velocity (m/s)

Greek Symbols

$\Delta\varepsilon$	Change in Strain
θ	Pitch angle (degrees)
ϕ	Roll angle (degrees)
ψ	Yaw angle (degrees)

Acknowledgements

I would like to extend my thanks to my supervisors Dr. Darrel Doman and Dr. Dominic Groulx, for all of their support and guidance throughout this research. I also would also like thank my committee members Dr. Robert Bauer and Dr. Jan Haelssig.

This research was made possible by the funding and support of the Fundy Ocean Research Centre for Energy. Thanks are also due to Tony Wright and all of the staff at the Fundy Ocean Research Centre for Energy, who supplied their time and support throughout this research.

Most of all I would like to thank my family and girlfriend, Lesley Seto, for all of their support and patience throughout my research.

Chapter 1 Introduction

The Bay of Fundy in Nova Scotia, Canada, is a site with large potential for tidal current energy generation. Fig. 1.1 depicts a map of Nova Scotia and the Bay of Fundy which experiences tide changes as high as 15 m (Tarbotton et al., 2006). These high tides result in a large amount of potential energy to be extracted with in-stream tidal turbines. The potential extractable energy is estimated to be 2.5 GW by Karsten et al. (2008) and 2.725 GW in the background analysis for the Canadian Ocean Energy Atlas Project (Tarbotton et al., 2006).

In Nova Scotia, the Fundy Ocean Research Centre for Energy (FORCE) was established as a test site for in-stream tidal energy technology. The FORCE test site is located in the Minas Passage, labeled in Fig. 1.1, in the Bay of Fundy where the depth averaged current can reach as high as 3.6 m/s (Karsten et al., 2008). These high currents can cause concern for subsea assets deployed in the Minas Passage. A report by the European Marine Energy Centre (EMEC) (2015) reviewing the integrity of subsea cables deployed at the EMEC tidal energy test site identifies high tidal currents causing cable abrasion due to vibrations and instability on the seabed as the main sources of risk to subsea tidal power transmission cables.

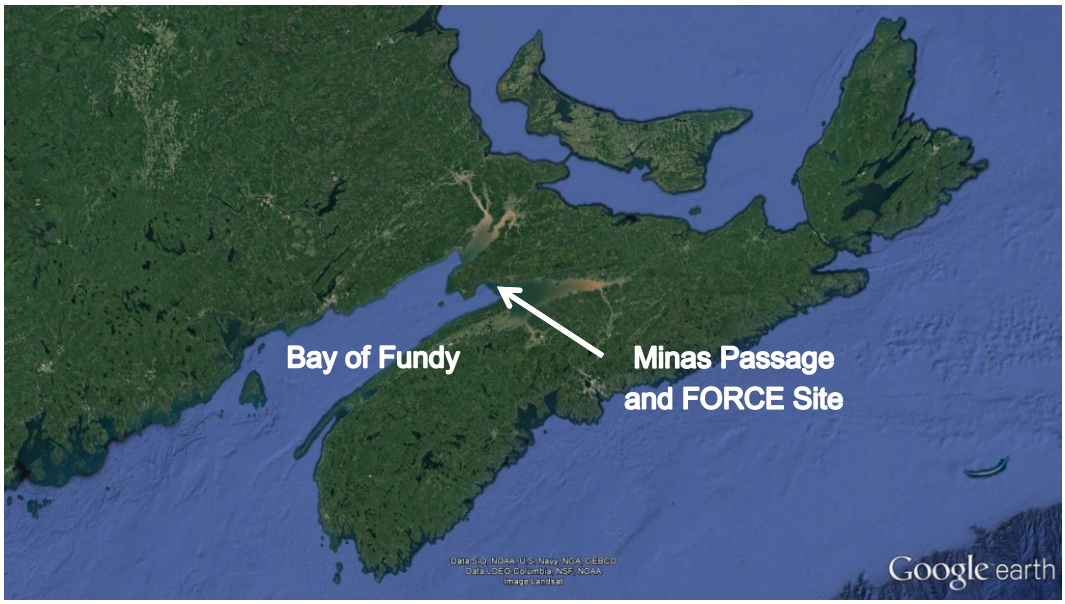

Figure 1.1 Bay of Fundy, Nova Scotia, Canada (Google Earth, 2016).

In order to transmit the electrical energy generated by in-stream tidal turbines to shore, FORCE has procured and deployed four subsea cables at the test site. Prior to connecting the cables to a tidal turbine FORCE has chosen to monitor the subsea end of the cables to determine how these cable ends behave once deployed on the seafloor prior to being connected to a tidal turbine.

1.1. Background

Due to the high currents at the FORCE test site and the bathymetry of the sea floor, there is concern that subsea transmission cables could move or be damaged following deployment. The cables have been deployed years before they will be connected to a turbine. As a result the subsea end of the cable is left on the sea floor connected to a ground anchor. The nature of the bedrock seafloor in the Minas Passage prevents the opportunity to trench and bury the cable to constrain it (AECOM, 2009). Inability to bury the cable leaves the cable with greater freedom to move on the sea floor than if it were buried. If left unmonitored, the state of the cable end could remain unknown until retrieval of the cable at the time of interconnection with a turbine. If the cable were to be damaged, this would result in increased costs and delays for FORCE and turbine operators that could setback development of tidal turbines in the Minas Passage. A system to monitor the cable end would allow FORCE to measure any motion and behavior of the cable end helping to ensure the cable is not damaged prior to mobilizing a turbine installation and interconnection operation.

The four cables that FORCE has deployed at the test site have the following specifications:

- 143 mm outer diameter
- 39.2 kg/m mass
- Three phase 34.5 kV cable for transmission of electrical power generated by tidal turbines;
- Two Layers of galvanized steel wire armour for protection of the cable against impacts and abrasion;

- Polypropylene string serving surrounding the outside of the cable;
- Maximum straight pull tension: 86 kN;
- Minimum bend radius under tension: 2.2 m;
- Twelve single mode fiber optic cable for data transmission from turbines or instrumentation;
- Four low voltage conductors for transmission of power to low voltage instruments.

A cross section of the cable is depicted in Fig. 1.2, labeling the cable components.

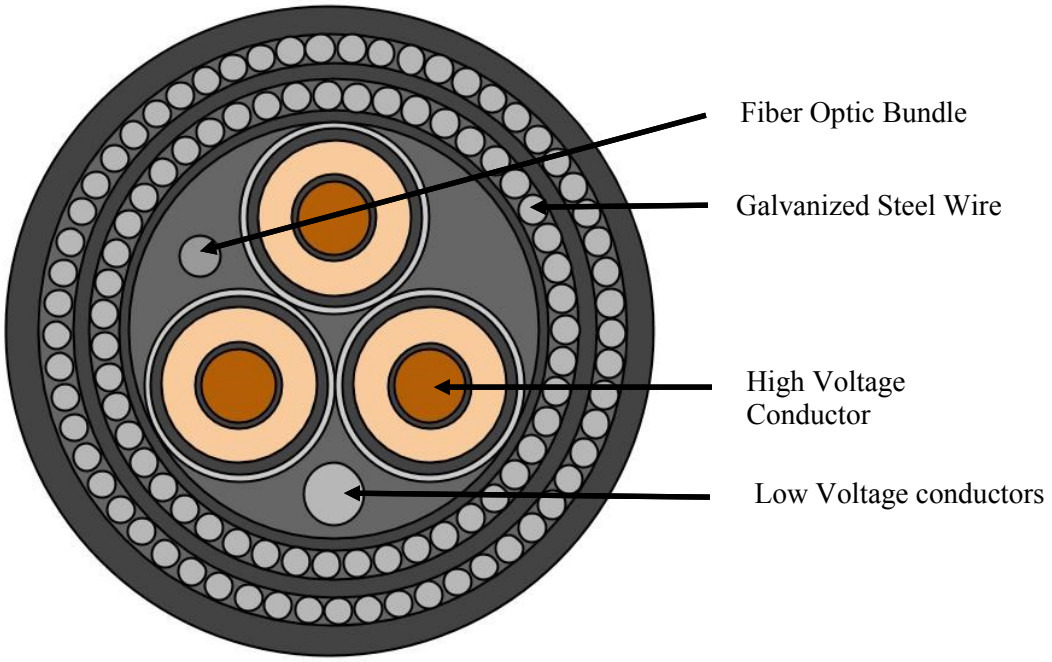

Figure 1.2 Diagram showing the cross section of FORCE subsea cable.

In order to monitor the cable after deployment and prior to connection to a turbine, FORCE procured a sensor package. The sensor package was developed by OceanWorks International and is shown in Fig. 1.3. The package was developed using commercially, available off-the-shelf components. The instruments included in this package are a 3-Axis

Attack Heading Reference System (AHRS) sensor and a microphone. The AHRS sensor includes on-board magnetometers, accelerometers, and gyroscopes. The sensor outputs 3-axis accelerations and orientation in Euler angles and quaternions. Two identical sensor packages were produced. The two sensor packages were originally intended by OceanWorks to be installed together at the subsea terminated cable end of one of the FORCE transmission cables with one sensor package acting as a redundant backup. Following changes to the design of the cable abandonment terminations and cable deployment plan, the two sensor packages were separated and installed at two of the four subsea cable terminations.

Figure 1.3 Photograph of sensor package (from author).

The instrumentation package transfers data to a computer at the FORCE substation, where the transmission cables are connected to the Nova Scotia electrical grid. The data is transferred via the fiber optics in the subsea transmission cables.

The AHRS sensor selected by OceanWorks is the SBG Systems IG-500 A. Common applications of this sensor are flight analysis, car motion analysis, buoy motion analysis, and ROV orientation.

The sensor package is secured inside the cable abandonment termination. The termination seals the subsea end of the cable to prevent water intrusion to the conductors and shielding. The termination also serves as a means to connect the cable to a turbine at the time of interconnection.

In order to detect and monitor movement of the subsea cable end, the data collected from the AHRS must be analyzed. This includes analysis of the orientation output and acceleration output of the sensor.

1.2. Problem Description

The subsea end, of the transmission cables deployed by FORCE in the Minas Passage have the potential to move along the sea floor and be damaged. In order to ensure the cables remain stable and undamaged, an instrumentation package which outputs acceleration and orientation is secured to the subsea termination of the cable ends. Using the data collected from the sensor, it is possible to monitor the state of the cable end prior to preparing a turbine connection to it.

1.3. Research Objectives

The objectives of this research are:

- Evaluate and verify the measurements from the AHRS sensor deployed with the FORCE cable.
- Develop a methodology to detect movement, changes in orientation, and accelerations of the device from datasets collected from the sensor.
- Analyse the retrieved data from the instrument deployed with the FORCE cables and monitor the cable for movement and changes in orientation.

To achieve these objectives, the accuracy of the measurements from the AHRS sensor has been evaluated. The orientation measurements were evaluated by rotating the sensor through known change in angle about each axis. The acceleration measurements were

evaluated by moving the sensor along a known inclined plane. The expected variation of the sensor outputs over longer periods of time was measured.

A method to parse the data collected from the sensor was implemented and evaluated. Once deployed, the sensor collected large datasets. This data needs to be parsed to identify events of movement, orientation change, or accelerations due to impacts.

Using the implemented method, the datasets collected from the deployed cable were analysed, allowing the deployed cable to be monitored for movements that may lead to damage.

Chapter 2 Literature Review

Monitoring the condition of subsea assets is important to maintenance planning and operations for marine industries. This chapter will present a review of methods and sensor types utilized to monitor a variety of subsea assets. In addition, the use of sensors that measure acceleration and orientation to detect movement is also presented.

2.1. Monitoring of Subsea Components

A challenge in the offshore oil and gas industry is monitoring the structural health of subsea assets due to the inaccessibility inherent to their location (Thivend, 2010). Jin et al. (2003) identifies that structural health monitoring using distributed strain sensing is effective to ensure the reliable operation of a pipeline, especially when all the factors leading to failure are unknown. Structural health monitoring can be completed using MEMS accelerometers or strain gauges. Fiber optic strain measurement can be used as a reliable source for strain measurement of subsea pipelines (Thivend, 2010). Zhao et al. (2012) details a monitoring system for a pipeline using a distributed Brillouin optical fiber technique. The method detects free spans due to scour along the pipeline by monitoring heat transfer that differs for pipeline spans in sediment and in water. Free spans of a pipeline occur when current flow uncovers sediment above and below a section of pipeline. This results in higher stress on the pipeline and the chance of vortex induced vibration from current flow past the pipeline. Pipeline failure has both economic and environmental costs, therefore a system to monitor pipeline structural health is significant to pipeline maintenance (Zhao et al., 2012). Roberts (2007) describes the use of fiber optic strain sensors to measure strain along a pipeline. King et al. (2011) identifies the problem of predicting response of subsea riser structures to adverse weather conditions such as hurricanes in the Gulf of Mexico. Monitoring equipment can help to describe the response of these structures and develop an integrity management program. Brower et al. (2012) also describes a pipeline in the Gulf of Mexico that utilizes a fiber optic sensing system to sense temperature, strain, and pressure along the pipeline length. Amara-Madi et al. (2013) describes a sensor system for monitoring a pipeline which uses a gyroscope, an accelerometer and a magnetometer to track the inertial motion of the pipe. The MEMS sensors offer an alternative to fiber optic sensors which are complex and difficult to deploy and power for deep sea environments.

The sensor system was demonstrated to operate in the conditions found in deep sea environments and provide temperature and motion data of a pipeline.

In addition to structures such as pipelines, the condition of subsea pumps can also be monitored (Jones et al., 2014). A fiber optic sensing system was used to monitor strain on the pump bearings, operating temperatures, and vibration of the motor housing. The system gives warning of developing problems with the equipment and allows the operators to prepare spare parts and minimize equipment downtime.

Similar to the need for monitoring the status of subsea power cables there is also a need for monitoring the status of umbilical cables used by remote operated vehicles. Andreassen et al. (2005) investigated the use of a Fiber Bragg grating (FBG) optical sensor to monitor the temperature of a remote operated vehicle cable. The sensor was proven suitable for monitoring a dynamic cable during operation.

2.2. Monitoring of Subsea Cables

The EMEC (2015) Sub-sea Life Cycle Study is the most comprehensive study on tidal power transmission cables to date. The study identifies wearing of the servings of the subsea cables in areas where suspensions and significant strumming were expected to occur. Suspensions occur when a cable is suspended between two uneven points on the seabed. Strumming can occur in suspended lengths of a cable where irregular flow around the cable cause cable movement. Cable movement at the contact points of the suspensions results in mechanical wear of the cable, reducing the lifespan. This poses the largest risk for damage to the cable and reduction in lifespan (EMEC, 2015). Findings on damage due to instability of the cables on the seabed were inconclusive, although moderate wear was observed on the cables in areas where some movement was predicted. The EMEC (2015) report direct monitoring to collect detailed data on cable movement.

Subsea cables have been monitored using fiber optic sensors. Brillouin optical time domain reflectometry (BOTDR) and Brillouin optical time domain analysis (BOTDA) are described by Mufti (2009) as sensors that utilize Brillouin scattering of back reflected light due to the refractive index of the sensing fiber. Brillouin scattering is a function of strain

and temperature allowing measurements of these two quantities. Eq. (2.1) describes this relationship where v_{B0} is the Brillouin frequency at a known strain and temperature, ΔT is the change of temperature, and $\Delta\varepsilon$ is the change of strain. The coefficients $\frac{\partial F}{\partial T}$ and $\frac{\partial F}{\partial \varepsilon}$ are dependent on the particular fiber material.

$$v_B = v_{B0} + \frac{\partial F}{\partial T}\Delta T + \frac{\partial y}{\partial \varepsilon}\Delta\varepsilon \tag{2.1}$$

BOTDR requires a single laser source at one end of the sensing fiber. BOTDA requires two laser sources at either end of the sensing fiber. The BOTDA arrangement provides a stronger signal and less detection problems than BOTDR (Mufti, 2009). These sensors are useful for monitoring power transmission cables which already have fiber bundles for data transmission embedded in them. The existing fibers that are in the bundle can be used as sensing fibers. BOTDR and BOTDA sensors are also known as distributed temperature and strain sensors (DTSS). Svoma et al. (2009) show that monitoring a subsea cable for off-shore wind turbine power transmission using DTSS can provide measurements of temperature with a resolution of 1 °C along the cable. Using the same technology to detect strain, operators can monitor cables for excessive movement. These measurements allow operators to assess cable condition, ageing, and reliability.

In addition to monitoring power transmission cables for tidal power, monitoring subsea power cables has become important for offshore windfarms operations to ensure a stable and reliable means of power transmission (Fromme et al., 2011). Tayama et al. (1995) shows optical fibers were utilized to monitor a 6.6 kV power transmission cable for damage. The sensing fibers were placed in three positions to determine the optimal placement for sensing cable damage: The bedding layer between the two armor layers, among the inner armor steel wires, and among the outer amour steel wires. It was determined that optimal placement of the sensing wires is in the bedding layer of the cable (Tayama et al., 1995). A similar study was also conducted for a 66 kV power transmission cable (Nishimoto et al., 1995). In the study, a commercial power cable was deployed and allowed for the location of damage along the cable to be detected within an 8 m resolution along the length of the cable. A BOTDR sensor was also used to measure inner cable temperature and outside strain damage of a power transmission cable in the Bohai Sea of

China. The initial strain distribution along a 70 m section of the cable was measured as a reference. Change in the strain measurement was used to determine cable sink along the seafloor. (Jiang et al., 2009).

A BOTDR system was proposed by Zhao et al. (2014) as real time monitoring system for a 110 kV cable measuring temperature and strain. The system offers a spatial resolution of 1 m for the distributed strain and temperature measurements. The system indicated that the condition of the cable was stable and that the effect of scouring and sediment movement is small with cable lay topography having a larger influence on the strain measured by the BOTDR system.

A BOTDA sensor was used to measure strain along a submarine power transmission cable during a cable lay and recovery operation (Kurashima et al., 1991). The sensor was used to determine residual strain in the cable following both the cable lay and recovery.

2.3. Comparison of Fibre Optic Strain Sensors

As detailed in sections 2.1 and 2.2 fibre optic strain sensors have been used to monitor subsea cables as well as other subsea components such as pipelines. The three varieties of fiber optic sensors used to monitor these components are BOTDR sensors, BOTDA sensors, and FBG sensors. Depending on the application a different sensor may be more advantageous to use. If the location where strain needs to be measured is known, then an FBG sensor would be appropriate as it measures strain at a single point. If strain measurements must be made over a long distance and the points of interest along this length are unknown or varying a distributed sensor, either BOTDR or BOTDA, is best(Mufti, 2009). BOTDR and BOTDA are similar as both utilise the principal of Brillion scattering to make strain measurements (Ohno et al., 2001). BOTDR requires the connection to only a single end of the sensing fiber. However, BOTDA requires a connection to both ends of the sensing fiber increasing the power of the signal (Mufti, 2009). If it is possible to connect either fiber end BOTDA would be preferable to use in order to reduce detection problems. In the application of monitoring the FORCE cables a distributed sensor would be appropriate to detect changes in strain along the full length of the cable. One end of the FORCE cable will be deployed into the Minas Passage leaving the shore end of the cable

available for connection to instrumentation. In this case a BOTDR sensor could be used. Although a BOTDR sensor could be used to measure movement along the length of the FORCE transmission cables, the use of fiber optic sensing technology is not as widespread or as readily available, so other solutions must also be considered such as the use of MEMS sensors used by Amara-Madi et al. (2013) detailed in section 2.1.

2.4. Accelerometers and Orientation Sensors Used in Subsea and Marine Applications

Accelerometers and orientation sensors have other applications for marine and subsea use such as buoys as well as remotely operated or unmanned underwater vehicles. Williams et al. (2013) describes the use of an AHRS on a surface buoy for alignment of current measurement from a moored current meter. Readings from the current meter are altered by buoy tilt caused by waves. The orientation measurements from the AHRS are used to translate the current measurement to the earth frame. Earle et al. (1998) also demonstrates the use of an inertial measurement unit (IMU) to provide earth frame reference of buoy orientation as an alternative to more expensive mechanical orientation measurement devices. Solid state angular rate sensors were used by Steele et al. (1998) as a low cost alternative for the measurement of pitch and roll. Kennedy et al. (2015) utilized IMU sensors for a low cost wave measurement buoy. The IMU sensors were shown to accurately measure wave height and sea state information.

MEMS sensors can also provide low cost solutions for underwater robots. Joordens et al. (2008) utilizes an IMU as a low cost navigation sensor for underwater robotics platforms. AHRS sensors are cost effective and small sized sensors for inertial navigation systems in unmanned underwater vehicles where GPS navigation is not possible due to deep water environments (Hwang et al., 2011). IMU sensors allow for high accuracy navigation systems to be used on low cost and small size underwater vehicles (Correia et al., 2003). An IMU sensor provides heading direction for an underwater inspection robot (Heo et al., 2012).

2.5. Accelerometer and Orientation Sensor Studies

An area of research that makes use of accelerometers, IMUs, or AHRS sensors used to detect and characterize movement is human fall detection. Bourke et al. (2007) uses tri-axial accelerometers to detect falls by elderly individuals. The accelerometers are mounted on the trunk and the thigh of the user. Simulated falls and activities of daily living were performed. The resultant signal from the tri-axial accelerometers, calculated using Eq. (2.2) were obtained from the root square sum of the three axial acceleration signals from the sensor.

$$A_R = \sqrt{{A_x}^2 + {A_y}^2 + {A_z}^2} \tag{2.2}$$

Using the datasets collected, a threshold was determined to differentiate falls from activities of daily living. When the acceleration threshold of 3.52 g at the trunk is exceeded, a fall is detected. Activities of daily living were not found to exceed this threshold. The study concluded that by placing a tri-axial sensor on the trunk of an individual, the simulated falls can be detected at a 100% rate by detecting when the resultant accelerometer signal exceeds the threshold.

In a similar study by Zhang et al. (2013), an AHRS is attached to the wrist and falls along with activities of daily living are simulated. Changes in pitch and roll attitude as well as acceleration, as shown in Eq. (2.2), are used to detect falls. Using the orientation and acceleration data, falls are able to be identified more accurately than using only an acceleration threshold analysis. A sliding window is used when analysing the acceleration, pitch, and roll angles because the maximum change of each parameter will not always occur in the same sample group. It was determined that simulated falls and activities of daily life were detected with 98.2% accuracy in comparison to 81.6% accuracy when using only an acceleration threshold to detect falls versus activities of daily life. Activities that may result in large accelerations such as jumping can be differentiated from falls when considering the pitch and roll orientation in addition to acceleration.

Kangas et al. (2008) considered the use of a tri-axial accelerometer mounted to the wrist, waist, or head. Four different parameters were used to detect falls during activities of daily

life were considered, sum total acceleration vector, dynamic sum acceleration vector, vertical acceleration, and impact velocity. The sum total acceleration is calculated as in shown in Eq. (2.2). The dynamic sum acceleration is calculated using the same equation but the acceleration data is processed by a high pass filter using a second order Butterworth filter with a cut off frequency of 0.25 Hz. Velocity is determined by integrating the acceleration signal at the time of impact.

Bourke et al. (2010) identified that detection that considers impact acceleration, velocity, and posture angle results in fewer false positive fall detections. Posture angle is calculated in Eq. (2.3) using the angle that the vertical *z*-axis component of acceleration is inclined to the gravitational vector.

$$\phi = \cos^{-1}(g_z(t)) \tag{2.3}$$

Velocity is determined by integrating the resultant acceleration from the three tri-axial acceleration signals and subtracting the static acceleration due to gravity as shown in Eq. (2.4).

$$V = \int_{t_i}^{t_f}(A_R(t) - g)dt \tag{2.4}$$

Using impact acceleration, velocity and posture angle resulted in detection of 0.94 false positives per day but with a sensitivity of 94.6% meaning some falls were not detected. Methods which consider only impact acceleration or impact acceleration and velocity achieved a sensitivity of 100% but also resulted in a greater number of false positives.

Chao et al. (2009) consider a cross product of the acceleration signals from a tri-axial accelerometer and compare it to the acceleration magnitude as shown in Eq. (2.2). The acceleration cross product is shown in Eq. (2.5). Where A is the acceleration components (a_x, a_y, a_z) measured by the accelerometer and B is a reference acceleration components (b_x, b_y, b_z) when the subject is standing. When the subject is standing A and B are parallel and the cross product AC is equal to 0. When the subject is lying A and B are perpendicular and Ac is equal to 1.

$$AC = |A \times B| \tag{2.5}$$

2.6. Summary

There have been several studies on monitoring the structural health of subsea cables utilizing distributed fiber optic sensing of strain and temperature. Distributed fiber optic sensors have also been used to monitor other subsea structures, notably pipelines. The use of these sensors has been demonstrated to reduce inspection cost and aid in planning of maintenance over the life cycle of the subsea asset. The use of accelerometers and MEMS based IMU or AHRS sensors for monitoring subsea structures is limited. However, these sensor are unable to measure along the entire length of a cable or pipeline like distributed sensors.

Despite the limitation AHRS and IMU sensors are used for marine and subsea application in unmanned underwater vehicles and buoys. For both applications, the sensors are capable of providing orientation data in reference to the earth and track motion such as speed or displacement. Buoy displacement is used to measure wave height, and displacement and speed are used in navigation systems of underwater vehicles.

Orientation sensors and tri-axis accelerometers have also been demonstrated to detect motion events in the biomedical field. These sensors are used in fall detection systems capable of determining when an individual has fallen based on acceleration and orientation data collected from sensors worn by the individual. Using the orientation and acceleration data, falls can be differentiated from regular daily activities. Similarly the AHRS mounted at the end of the abandonment termination of the FORCE subsea cables could be used to detect motion events.

The use of distributed Brillouin strain and temperature sensors to monitor subsea cables in the past has been limited. The use of these sensors has the advantage of utilising the optical fibers already embedded into subsea transmission cables as the sensing element and obtaining measurements at all points along the fiber. Distributed sensing would allow for measurement of movement along the entire length of the cable as opposed to only the cable end. An AHRS, however, is commercially available off the shelf sensor which can be used to monitor movement of the cable abandonment termination at the subsea cable end. The data collected from a AHRS can characterize the three-dimensional orientation of the

abandonment termination, as opposed to a distributed strain sensor that only provides a difference in measured strain at points along the cable.

Chapter 3 Equipment

A sensor package was designed for FORCE by OceanWorks International to monitor the transmission cable ends. The sensor package is mounted at the subsea end of the cable inside the cable abandonment terminations that seal the subsea end of the cable when deployed to the seafloor. The cable abandonment termination was designed with space in the end to secure the sensor package. The package includes the SBG IG-500A AHRS unit, a microphone, and media converter that transmits the data from the AHRS unit and microphone along two of the fiber optic lines in the cable. The fiber optic lines are connected to a shore station computer which retrieves the data from the AHRS unit and the microphone. This chapter will present the details of the equipment that was used to monitor the subsea ends of the FORCE transmission cables as well as details of the deployment of the cables with sensor packages at the FORCE cable berths

3.1. Cable Abandonment Termination

The cable abandonment termination seals the subsea end of the cable. The subsea transmission cables at the FORCE site were deployed in advance of the installation of any tidal turbines. The abandonment termination prevents water from intruding into the cable shielding and sheeting, corrosion of the cable conductors, and serves as a means of cable recovery and connection at the time of cable retrieval and turbine installation. The end of the abandonment termination is secured to ground tackle which is weighed down to the seafloor with clump weights and provides a wire to hook with a grapple in order to recover the cable.

The cable abandonment termination is composed of three sections that are fabricated from 18” schedule 40 steel pipe. The sections are flanged and bolted together. The end of the termination provides room to mount the sensor package. Figure 3.1 shows the sensor package inside the end cap of the cable abandonment termination. The endcap provides 330 mm of space between the termination wall and ends of the high voltage conductors to install the sensor package along rails which are welded inside the endcap. At the end of the termination the sensor package can easily be connected to the low voltage power conductors and optical fibers.

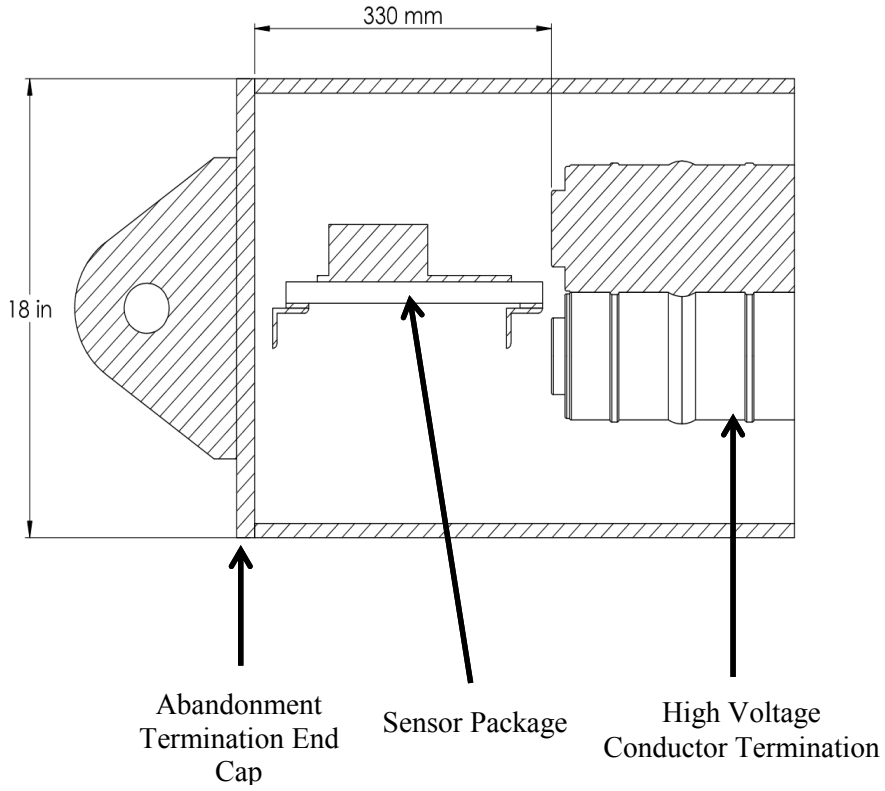

Figure 3.1 Schematic of the sensor package inside of the cable abandonment termination.

3.2. Sensor Package

The sensor package contains components to track movement and disturbances of the cable abandonment termination. The package contains the following components listed in Table 3.1.

Table 3.1 Sensor package components

SBG Systems IG-500A AHRS
ElCOMMTECH 1022S-AT/DX3-M2FC Fiber Optic Digital 2 Channel Audio Transmitter & RS-232 Data Transceiver
FSC-S15-12U power supply
Audio-Technica ES947 condenser microphone

The instruments are attached to a steel plate that is fastened inside the abandonment termination. The FSC-S15-12U power supply provides power to the other components of

the package. The power supply takes 120 VAC power input from the shore station unit and outputs 12 VDC. The transmitter/transceiver receives data from the SBG Systems IG-500A and outputs the data to the shore station unit via a fiber optic connection through the transmission cable. The ES947 microphone was installed in addition to the IG-500A sensor, shown in Fig. 3.2, to record any sound that may occur due to movement of the cable abandonment termination or impacts to the termination by debris in the water column and seafloor.

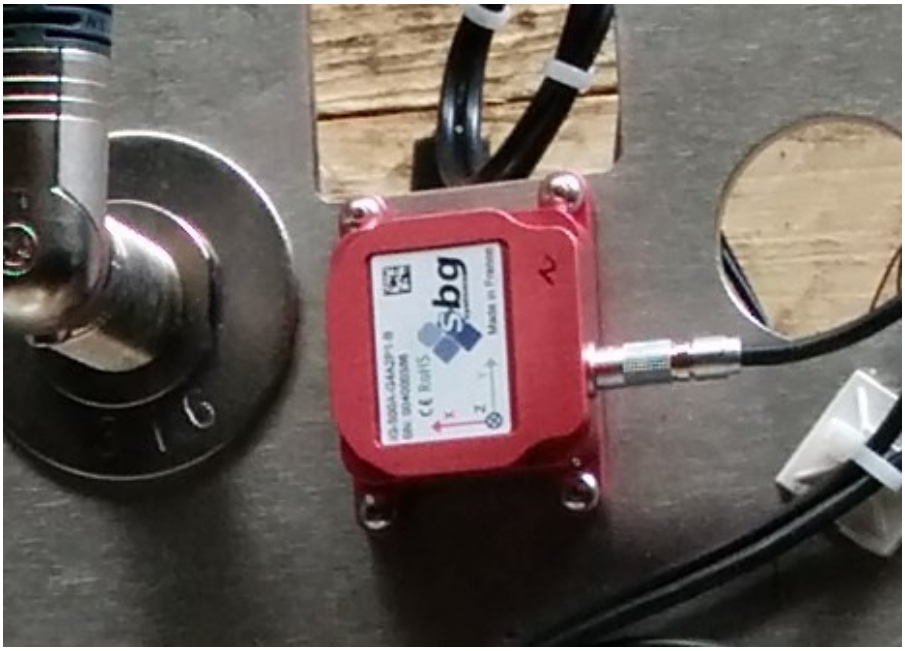

Figure 3.2 Photograph of SBG Systems IG-500A mounted on sensor package (from author).

3.2.1. SBG Systems IG-500A

The IG-500A AHRS is included in the sensor package in order to detect and measure accelerations and changes of orientation of the terminated end of the cable. The AHRS unit outputs orientation data and acceleration in three axes. The analysis of these inputs to monitor movement of the FORCE transmission cable ends is the main focus of this research. The unit uses the outputs from three gyroscopes, three magnetometers, and three accelerometers with an Extended Kalman Filter to output the 3D orientation of the sensor. Table 3.2 lists the specifications for the IG-500A AHRS unit

Table 3.2 SBG systems IG500A specifications

Roll/Pitch (Dynamic)	2.0° RMS
Heading (Dynamic)	2.0° RMS
Resolution	< 0.05°
Sensing range	360° in all axes
Maximum output rate	100 Hz
Shock limit	1000 g (powered); 2000 g (Unpowered)
Operating vibration	3 g RMS (20 Hz to 2 kHz)
Accelerometer measurement range	± 5 g
Accelerometer bias at start-up	± 5 mg
Accelerometer in-run stability bias	± 0.06 mg
Accelerometer noise density	0.25 mg/√Hz
Available data	Euler angles, quaternions, acceleration, device status

As shown in Table 3.2, the orientation output is available from the sensor unit in the form of Euler angles and quaternions. Euler angles are defined as a sequence of rotations from a fixed frame. There are three rotations about the *x*, *y*, and z axes. The three rotations are denoted as roll (ϕ) about the *x*-axis, pitch (θ) about the *y*-axis, and yaw (ψ) about the *z*-axis. A diagram of the Euler angle rotations is shown in Fig. 3.3. Euler angles provide a simple method to visualize the rotation of the device about a fixed reference frame. The Euler angles can be used to calculate the directional cosine matrix (DCM). Equation 3.1 demonstrates the formula for calculating the DCM using the yaw, pitch, and roll angles. A DCM can be used to transform one coordinate reference frame to another, for example, a local coordinate system to an earth fixed coordinate system.

$$DCM = \begin{pmatrix} \cos\psi & -\sin\psi & 0 \\ \sin\psi & \cos\psi & 0 \\ 0 & 0 & 1 \end{pmatrix} \begin{pmatrix} \cos\theta & 0 & \sin\theta \\ 0 & 1 & 0 \\ -\sin\theta & 0 & \cos\theta \end{pmatrix} \begin{pmatrix} 1 & 0 & 0 \\ 0 & \cos\phi & -\sin\phi \\ 0 & \sin\phi & \cos\phi \end{pmatrix} \quad (3.1)$$

Alternatively quaternions can also be used to represent the orientation of the unit. Quaternions represent an axis-angle rotation of angle θ, about an axis with unit vector *v*, where *v* is given in Eq. (3.2).

$$v = v_x i + v_y j + v_z k \tag{3.2}$$

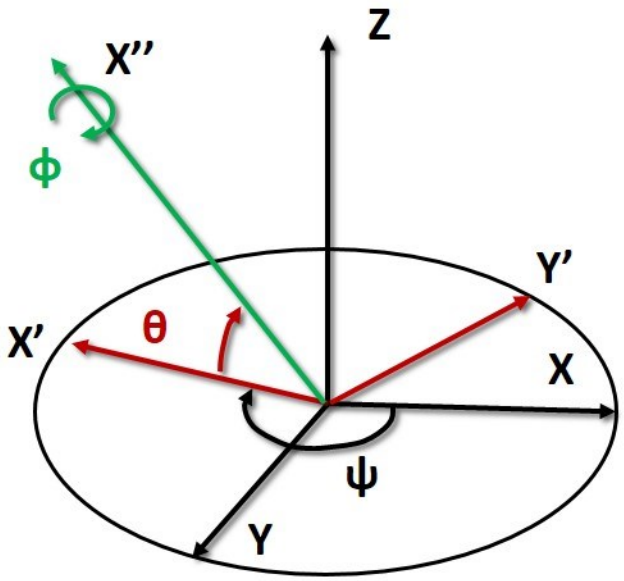

Figure 3.3 Diagram of Euler angle rotations.

The components of the quaternion are as shown in Eqs. (3.3), (3.4), (3.5), and (3.6).

$$q_o = \cos\frac{\theta}{2} \tag{3.3}$$

$$q_1 = v_x \mathrm{i} \sin\frac{\theta}{2} \tag{3.4}$$

$$q_2 = v_y \mathrm{j} \sin\frac{\theta}{2} \tag{3.5}$$

$$q_3 = v_z \mathrm{k} \sin\frac{\theta}{2} \tag{3.6}$$

A unit quaternion, Eq. (3.7) can be used to rotate a vector, *u,* as shown in Eq. (3.8). Where q^{-1} is the complex conjugate of *q*.

$$\|q\| = \sqrt{q_0^2 + q_1^2 + q_2^2 + q_3^2} = 1 \tag{3.7}$$

$$u = quq^{-1} \tag{3.8}$$

Quaternions are not as easy to visualize, however, using quaternions to represent orientation can be less computationally demanding and the issue of gimbal lock does not arise unlike with the use of Euler angles. The conversion of quaternions to a DCM is shown in Eq. (3.9).

$$DCM = \begin{pmatrix} 2{q_0}^2 + 2{q_1}^2 - 1 & 2q_1q_2 - 2q_0q_3 & 2q_0q_2 + 2q_1q_3 \\ 2q_1q_2 + 2q_0q_3 & 2{q_0}^2 + 2{q_2}^2 - 1 & 2q_2q_3 - 2q_0q_1 \\ 2q_1q_3 - 2q_0q_2 & 2q_2q_3 + 2q_0q_1 & 2{q_0}^2 + 2{q_3}^2 - 1 \end{pmatrix} \quad (3.9)$$

When using Euler angles to represent the orientation of the sensor gimbal lock occurs when the pitch (θ) of the sensor approaches $-\frac{\pi}{2}$ or $\frac{\pi}{2}$. When gimbal lock occurs the Euler angle output is no longer able to properly represent changes in the orientation of the sensor. By using quaternions in the calculation of the DCM gimbal lock is avoided.

The Euler angles represent a series of rotations of the sensor coordinate system from a Earth fixed reference frame in the order about the sensor *z*-axis, then *y*-axis, and then *x*-axis or ψ, θ, then ϕ. The origin of the coordinate system of the sensor is depicted in Fig. 3.4. For the earth fixed reference frame the *x* axis is aligned to magnetic north. The *z* axis is aligned with gravity. The *y* axis is aligned 90° from the *x*-axis pointing east therefore the coordinate system maintains a right handed convention. This is also referred to as a North, East, Down coordinate system.

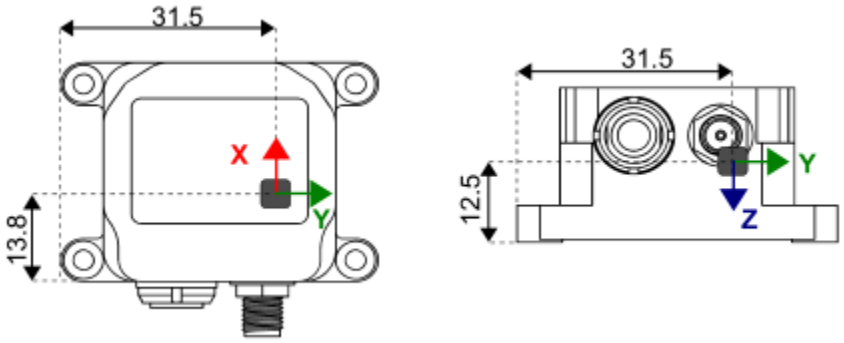

Figure 3.4 Local coordinate system origin of the IG-500A AHRS (SBG Systems, 2015).

In order to translate vectors measured by the sensor, such as acceleration, from the sensor coordinate system to the fixed reference coordinate system, the DCM shown in Eq. (3.1) or (3.9) is used. For example, Eqs. (3.10) and (3.11) show the translation of the

accelerations measured in the local coordinate system of the sensor to the accelerations in the fixed earth coordinate system.

$$a_{Earth} = DCM \cdot a_{LCS} \tag{3.10}$$

$$\begin{bmatrix} a_x \\ a_y \\ a_z \end{bmatrix}_{Earth} = DCM \cdot \begin{bmatrix} a_x \\ a_y \\ a_z \end{bmatrix}_{LCS} \tag{3.11}$$

Using the inverse of the DCM, a vector can be translated from the earth frame back the local coordinate system of the sensor as shown in Eq. (3.12).

$$a_{LCS} = DCM^{-1} \cdot a_{Earth} \tag{3.12}$$

The inverse of the DCM is the transposed matrix shown in Eq. (3.13).

$$DCM^{-1} = DCM^{T} \tag{3.13}$$

3.3. Shore Station

The shore station unit consists of an uninterrupted power supply, a power unit, a media converter, a rack mounted computer and monitor. The power unit provides 220 VAC to be connected to the power supply of the sensor package. The media converter provides the input for the fiber optics which transmits data to and from the sensor package over the subsea cable. The back panel of the shore station unit is shown in Fig. 3.5. The pilot cable connector connects the power supply, and the Tx and Rx FC fiber optic connectors connect to the corresponding connectors of the sensor package power supply. The rack computer runs the SBG systems software to monitor and collect data from the IG-500A sensor and record sound from the ES947 microphone.

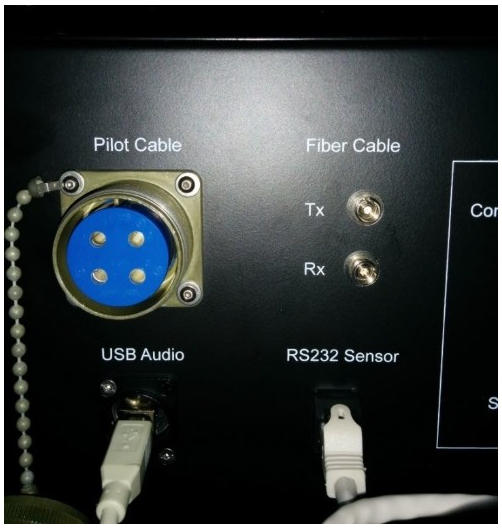

Figure 3.5 Photograph of shore station unit back panel (from author).

3.4. Installation and Deployment

Prior to the deployment of the four subsea cables to the FORCE site, the two sensor packages were installed in the cable abandonment terminations of two of the cables. The low voltage conductors were connected to the sensor package power supply and two optical fibers were connected to the transmit (Tx) and receive (Rx) ports of the sensor package media converter. Temporary power connections were made over the low voltage conductors and temporary fusion splices were made on the fibers of shore end of the cables to ensure the sensor package was transmitting data over the subsea cables to the shore station unit.

The four tidal turbine berths at the FORCE site are labeled A, B, C, and D. A cable was deployed to each berth. Similarly the cables are labelled according to the berth they are deployed to. Cable A is deployed to berth A, Cable B is deployed to berth B, etc. The sensor packages were installed to the cables that were deployed at berth A and C. In Fig. 3.6 the cables are shown as they were deployed to the FORCE site. Figure 3.7 provides a closer view of berths A and C.

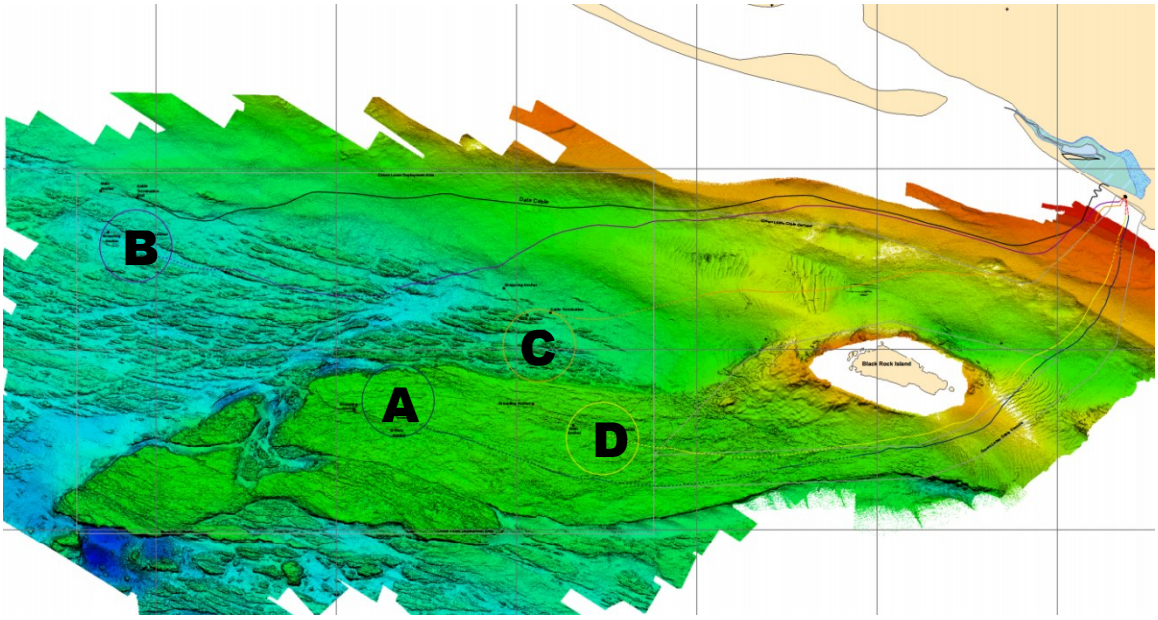

Figure 3.6 As laid survey of subsea cables deployed at the FORCE site (Prepared by Seaforth Engineering for FORCE, 2015).

A zoomed in section of the area where berths A, C and D are located is shown in Fig. 3.7.

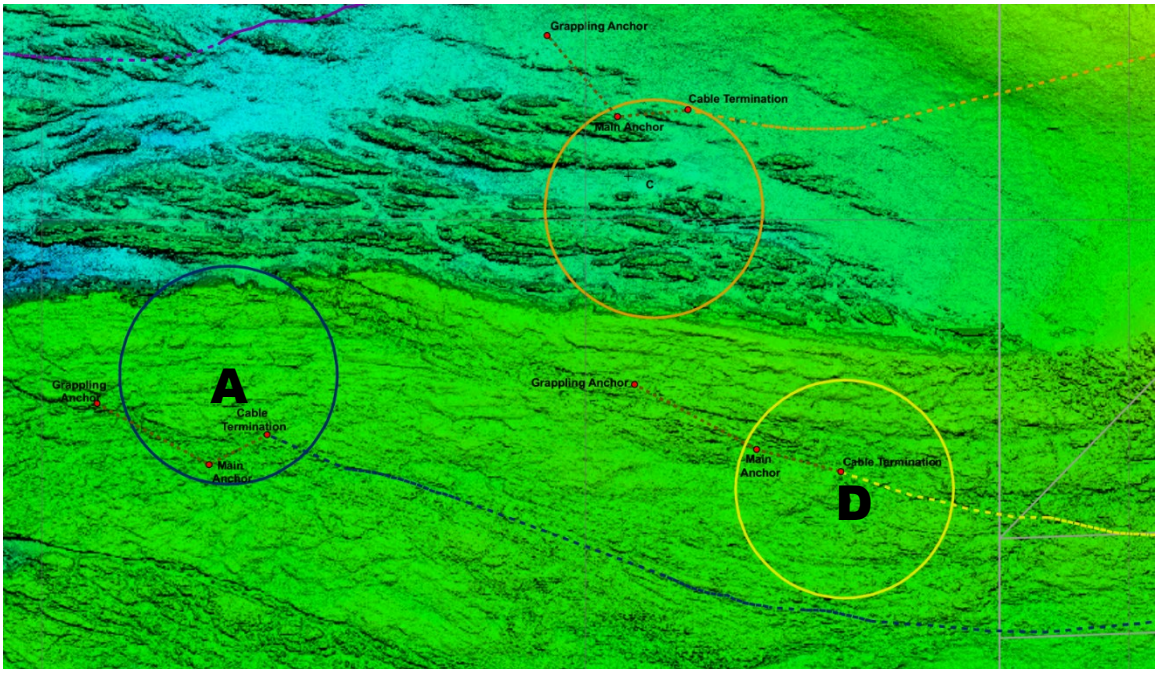

Figure 3.7 FORCE berth sites A, C, and D (Prepared by Seaforth Engineering for FORCE, 2015).

The seabed of site A consists of a flat volcanic bedrock surface (AECOM, 2009). Site C is placed in an area of sedimentary bedrock with exposed bedrock ridges and regions of gravel, cobbles, and boulders (AECOM, 2009).

Following the deployment of the cables completed on October. 28, 2-14, the shore station unit was installed at the FORCE substation. The substation is located approximately 2 km from the point where the subsea cables make landfall at the FORCE site. At the substation the high voltage conductors are connected to the Nova Scotia power grid. The fiber optic bundles and low voltage conductors are also terminated at the substation. The low voltage conductors and optical fibers were connected between the sensor package and the shore station unit, providing power to and data transmission from the sensor package.

3.5. Summary

The subsea end of the four FORCE transmission cables are sealed by the cable abandonment termination. The sensor packages are secured inside the abandonment terminations. The IG-500Ain the sensor package transmits orientation data as Euler angles or quaternions and tri-axial acceleration data. Following the deployment of the cables to the FORCE site tidal turbine berths, this data is used to monitor the cable ends.

Chapter 4 Measurements

Prior to the deployment of the sensor plate mounted in the cable abandonment termination, measurements from the sensor package were taken in a laboratory. To determine the accuracy in the measurements of yaw, roll, and pitch angle, the sensor package was rotated by a set change in angle. The sensor package was also rolled along an inclined plane. The measurements from the IG-500A AHRS accelerometers were compared against theoretical and simulated values. These measurements are used to determine the accuracy of the measurements that will be taken from the sensor package when it is deployed in the cable abandonment termination to determine the behavior of the cable end on the sea floor. This chapter presents the analysis of measurement taken to determine the sensor package orientation and accelerometer accuracy.

4.1. Orientation Measurements

In order to determine how the IG-500A AHRS behaves when mounted to the sensor plate as a part of the complete sensor package, a series of static measurements were collected. The measurements will be used to determine the uncertainty of the yaw, pitch, and roll measurements for the IG-500A. These measurements can be compared to the accuracy specifications provided by SBG Systems.

To perform the measurements, the sensor plate was mounted in the vice of a Bridgeport mill rotary table shown in Fig. 4.1. The orientation of the IG-500A sensor relative to the rotary table is demonstrated in Fig. 4.2. To measure changes in the yaw angle (ψ) the sensor plate was mounted in the chuck vice of the rotary table lying horizontal to the ground such that rotations are made around the sensor's z-axis. To measure changes in the roll angle (ϕ) the sensor plate was mounted in the chuck vice of the rotary table with the table held perpendicular to the ground such that rotations are made around the sensor's x-axis. To measure changes in the pitch angle (θ) the sensor plate was mounted in the chuck vice of the rotary table with the table also held perpendicular to the ground such that rotations are made around the sensor's y-axis. The rotary table dial is scaled to be adjusted in increments of 2 degree minutes or 0.033°. The rotary table allows the sensor to be rotated a set change in angle in each of the yaw, roll, and pitch planes. The sensor plate was rotated in the yaw

plane by increments of 90°, 45°, 10°, and 1°; rotated in the pitch plane by increments of 10° and 1°; and rotated in the roll plane by increments of 90°, 10°, and 1°. Data was collected from the IG-500A at a frequency of 50 Hz for these measurements. The change of angle performed on the rotary table will be compared to the change of angle measured by the sensor.

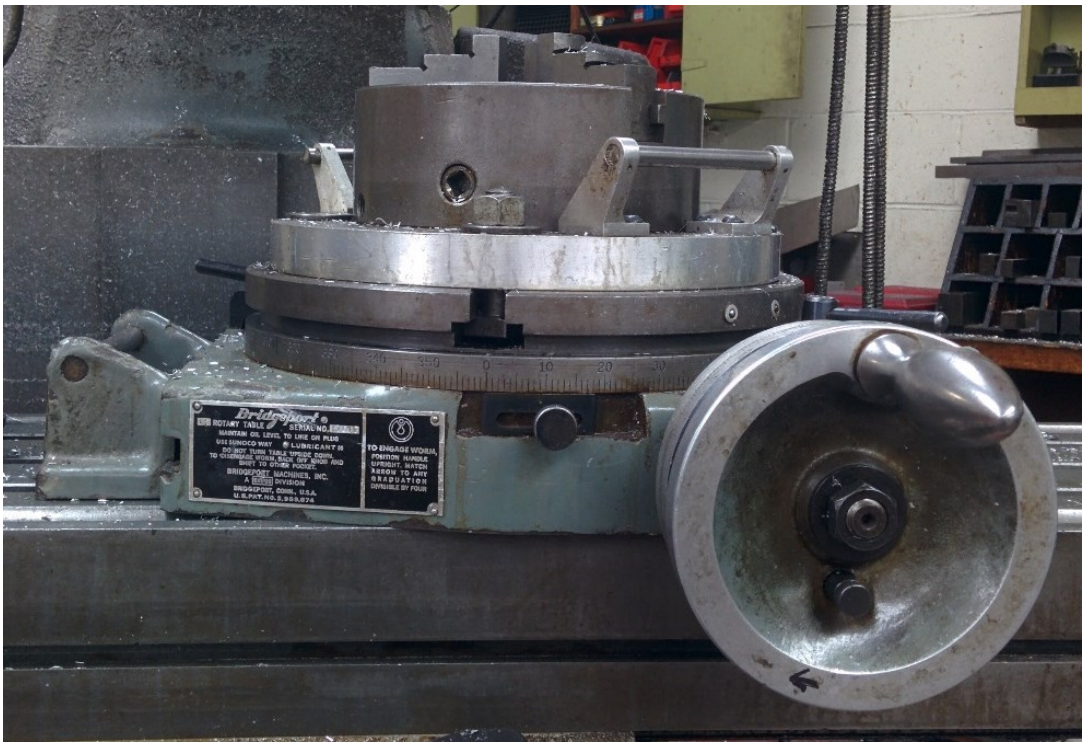

Figure 4.1 Photograph of rotary table (from author).

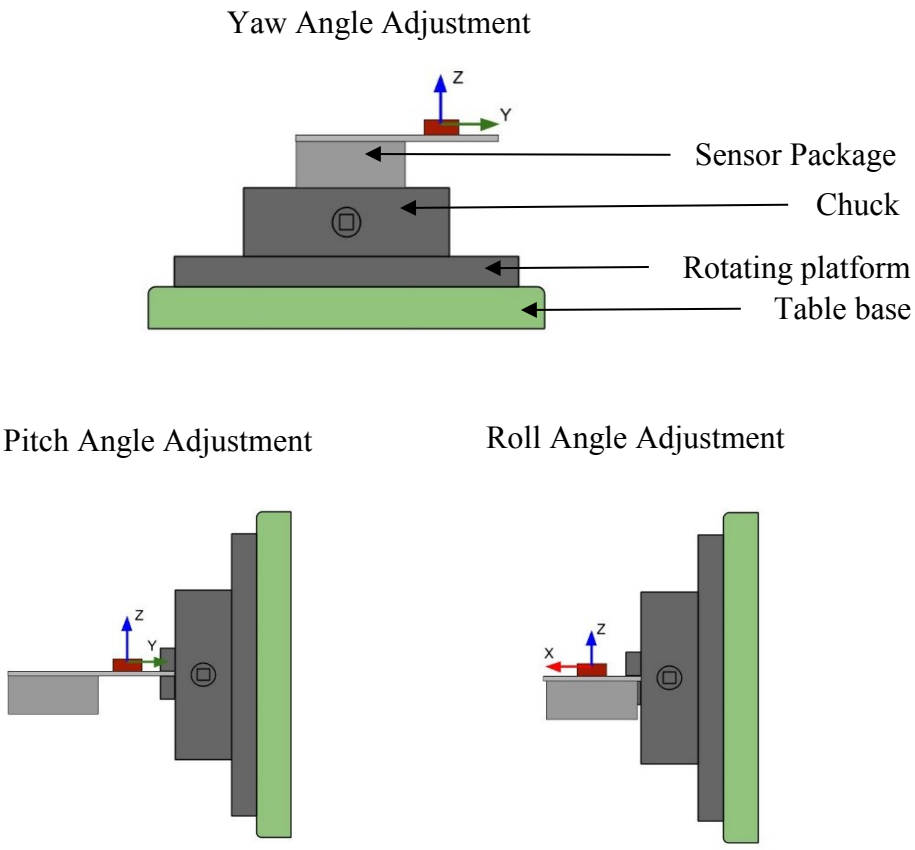

Figure 4.2 Sensor plate mounted in rotatory table for pitch, roll, and yaw measurement.

Bland et al. (1986) present a method for comparing measurements made from two different instruments. The difference between the two measurements was calculated to determine a mean difference and standard deviation of the difference. Using the mean and standard deviation, 95% of the measured difference (d) is expected to fall between the interval shown in Eq. (4.1), where $\overline{d}$ is the mean, s is the standard deviation, and 1.96 is the z-score for a 95% confidence level. When using a smaller sample size the appropriate t-distribution value is used in place of the z-score. Bland et al. (1986) refer to the limits of this interval as the limits of agreement.

$$\overline{d} - 1.96s \; < \; d \; < \bar{d} + 1.96s \tag{4.1}$$

Bland et al. (1986) also consider the uncertainty of the mean and limit of agreement shown in Eqs. (4.2) and (4.3).

$$Standard\ error\ of\ \overline{d} = \sqrt{\frac{s^2}{n}} \tag{4.2}$$

$$Standard\ error\ of\ \overline{d} \pm 1.96s = \sqrt{\frac{3s^2}{n}} \tag{4.3}$$

The limits of agreement are estimated based on the sample of measurements made to determine the difference. Using standard error, the uncertainty of the limit of agreement is determined. Using this method, the agreement between the change in angles measured by the IG-500A sensor and the rotary table can be evaluated.

4.1.1. Yaw angle measurement

The yaw angle (ψ) measures the angle about the z axis of the IG-500A AHRS. The sensor package was mounted horizontally in the rotary table vice with the rotary table lying horizontal. The sensor package was rotated through angle changes in steps of 90°, 45°, 10°, and 1°.

The measurements taken for rotating the sensor package in steps of 90° are shown in Fig. 4.3. The sensor package was placed and secured in the vice of the rotary table. Data was collected from the sensor at a sample rate of 50 Hz. The sensor package was left static in order to collect the steady signal of the yaw angle in its current orientation. A 50 sample average was recorded from the sensor. After several seconds, the sensor package was rotated by 90° using the hand dial of the rotary table. Once again, the package was left steady to collect a steady signal from the yaw angle for 50 samples. The average value of the 50 samples of the yaw angle signal during the steady period was used to take the difference from 50 sample average during the previous steady period and compare against 90° change of angle of the rotary table. This procedure was continued twelve times to collect measurements of the twelve yaw angle step changes. This procedure was used to measure changes of 90° as well as 45°, 10°, and 1°.

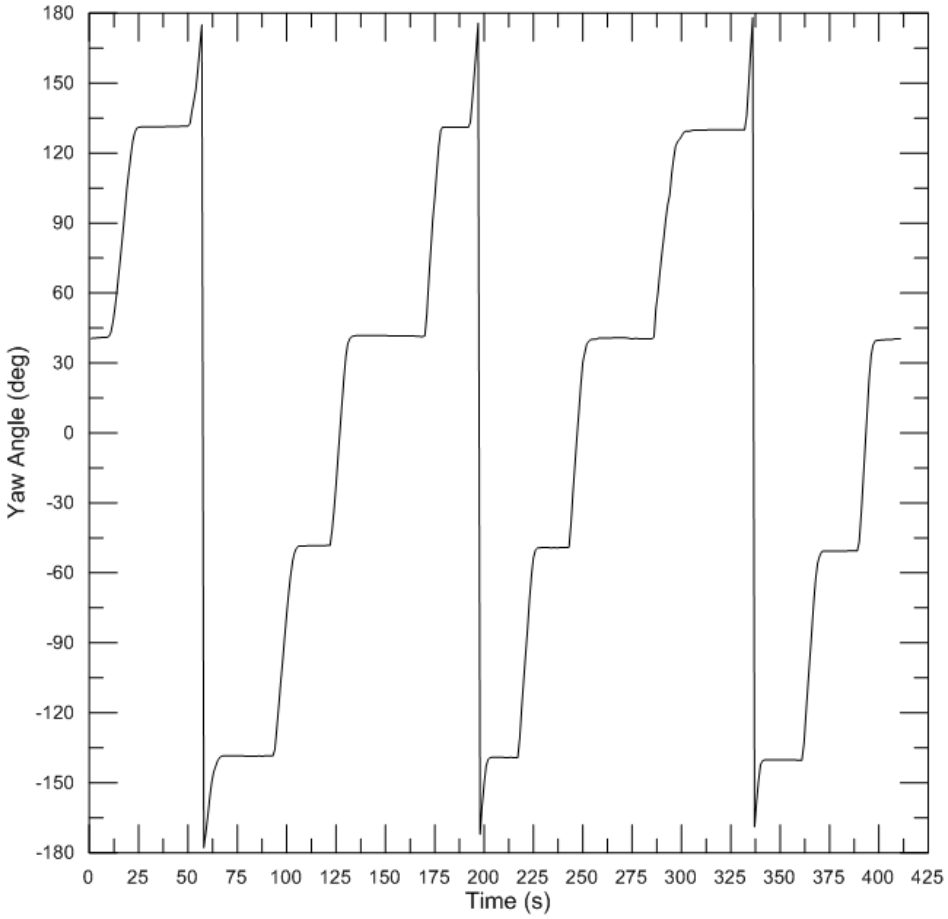

Figure 4.3 Yaw angle measurement in steps of 90°.

The measured step changes for steps of yaw orientation of 1° are shown in Fig. 4.4. Each data point in the plot represents a change of angle measured from the sensor during a 1° rotation on the rotary table. For step changes of 1°, fifteen steps were measured using the procedure described at the beginning of section 4.1.1. Figure 4.4 displays the data points for these fifteen measurements. The 95% confidence uncertainty of the measured difference of angle due to the 2.0° RMS accuracy of the sensor for 50 samples is 1.1° as calculated using a *t*-distribution value of 2.009 and the standard error in Eq. (4.2). The error bars for each data point indicate the sensor accuracy and sample precision error uncertainty of ±1.1°. The solid line indicates the reference change of angle performed on the rotary table of 1° and the dashed line is the sample mean change of angle measured by the IG-500A.

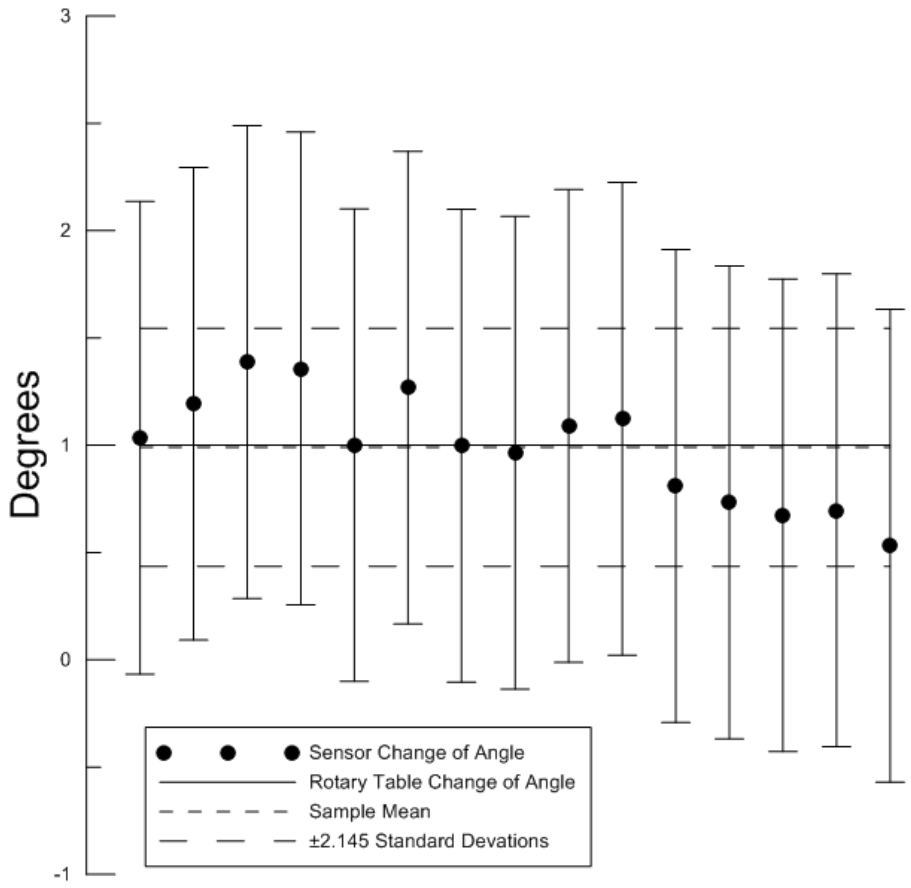

Figure 4.4 Change of yaw angle measured by sensor for rotary table steps of 1°.

Table 4.1 lists the values that are shown in Fig. 4.4. The sample mean value was determined to be 0.99° with a 95% confidence uncertainty of ±0.14. The sample mean varied little from the reference change of angle with a difference of 0.01° or a percent difference of 0.93%. However, the maximum outlier measured was 0.53° with a much greater difference of 0.47° or a percent difference of 46.83%. The fifteen sample changes of angle are bound by 2.145 standard deviations from the sample mean with 95% confidence from 1.55° to 0.44°. This corresponds to a difference of -0.56° to + 0.55° from the 1° reference measurement or a maximum percent difference of 56.41%. Although the relative difference is large, the measured changes of angle agree within a range of approximately 1°.

Table 4.1 Values for change of yaw angle measured by sensor for rotary table steps of 1°

Total number of data points	15

Reference change of angle (deg)	1.0
Mean change of angle (deg)	0.99
Standard deviation	0.26
Uncertainty (deg)	0.14
Maximum outlier difference (deg)	0.47
Limit of agreement (deg)	±0.55
Limit of agreement uncertainty (deg)	±0.25

Figure 4.5 displays the values collected for a step change of 10°. Each data point in the plot represents a change of angle measured from the sensor during a 10° rotation on the rotary table. The error bars for each data point indicate the sensor accuracy and sample precision error uncertainty of the measurements. The sample precision error was greater during the 10° rotary table steps due to variation in the yaw angle measured by the sensor over the 50 sample average. The maximum error measured is ±1.3° due to the larger precision error. Twelve data points were collected using the procedure explained at the beginning of section 4.1.1 utilising a step of 10° measured on the hand dial of the rotary table. The values depicted in Fig. 4.5 are listed in Table 4.2. The sample mean was determined to be 10.11° with a 95% confidence uncertainty of ±0.81°. Again, the mean change of angle varied only a small amount from the reference angle with a difference of 0.11° or a percent difference from the reference of 0.11%. However the maximum outlier measured a greater difference from the reference of 1.90° or a percent difference of 18.98%. The twelve sample changes of angle are bound by 2.201 standard deviations from the sample mean with 95% confidence from 12.92° to 7.31°. This corresponds to a difference of -2.69° to + 2.92° from the 10° reference measurement or a maximum percent difference of 26.93%. With an increased change in angle, the percent difference in the measurement is less than observed for a 1° change in angle. However, the range of agreement between the rotary table and sensor measurements was greater with a range of approximately 6°.

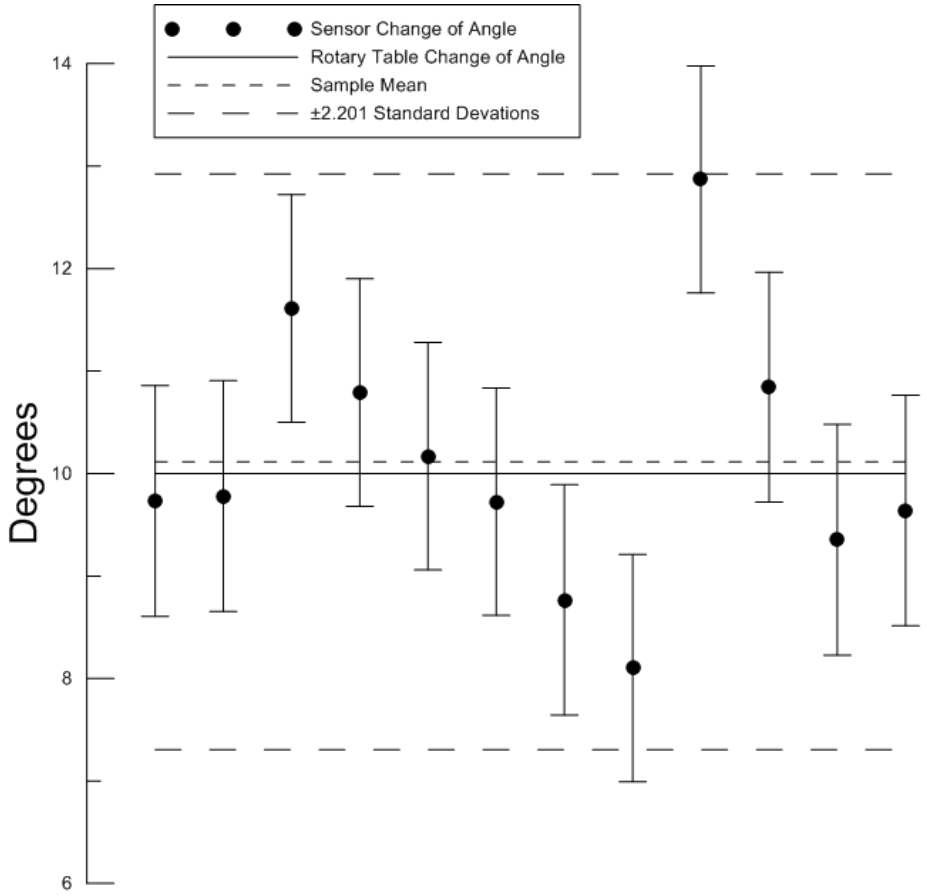

Figure 4.5 Change of yaw angle measured by sensor for rotary table steps of 10°.

Table 4.2 Values for change of yaw angle measured by sensor for rotary table steps of 10°

Total number of data points	12
Reference change of angle (deg)	10.0
Mean change of angle (deg)	10.11
Standard deviation	1.28
Uncertainty (deg)	0.81
Maximum outlier difference (deg)	1.90
Limit of agreement (deg)	±2.81
Limit of agreement uncertainty (deg)	±1.40

Figure 4.6 displays the values collected for the step of change 45°. Each data point in the plot represents a change of angle measured from the sensor during a 45° rotation on the rotary table. The error bars for each data point indicate the sensor accuracy and sample precision error uncertainty of ±1.1°. The precision errors of the 50 sample means were smaller for the rotary table steps of 45° in comparison to the rotary table 10° step measurements Nine data points were collected using the procedure explained at the

beginning of section 4.1.1, utilising a step of 45° measured on the hand dial of the rotary table. The values depicted in Fig. 4.6 are listed in Table 4.3. Again, the mean change of angle varied only a small amount from the reference angle with a difference of 0.29° or a percent difference of 0.65% from the reference. This is a greater difference measured in comparison to the step changes of 1° and 10°. However, the maximum outlier measured a difference from the reference of 0.79° or a percent difference from the reference of 1.75%. Although this is a greater difference measured for the 1° step, it is smaller than the difference measured in the 10° step. The twelve sample changes of angle taken fall within an interval of 2.306 standard deviations from the sample mean change of 44.70° with a confidence of 95%. This is an interval of 45.30° to 44.11° as shown on Fig. 4.6.

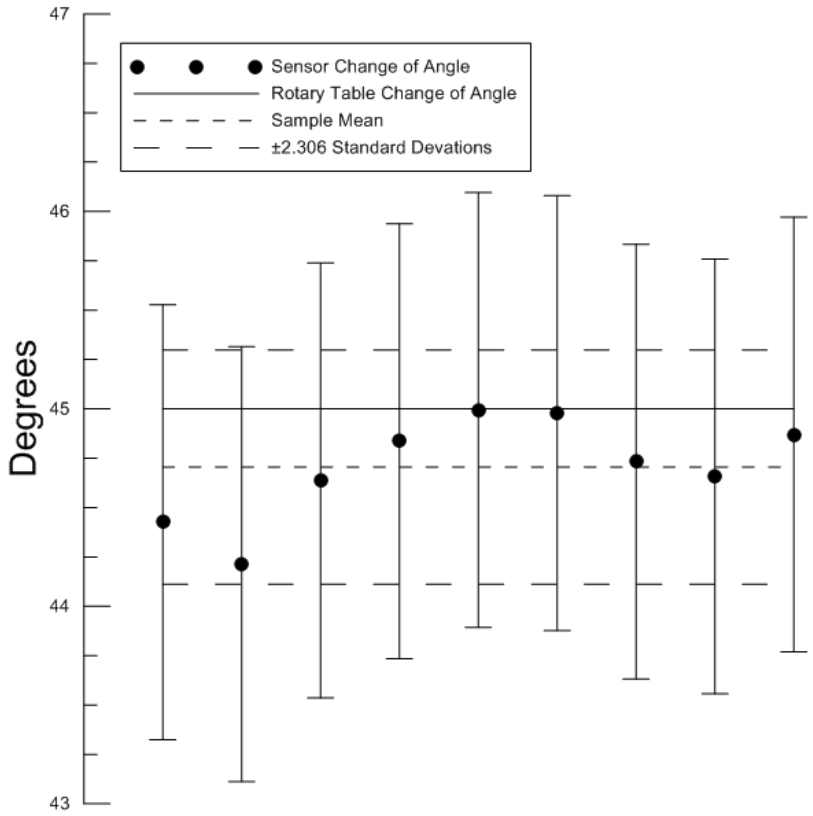

Figure 4.6 Change of yaw angle measured by sensor for rotary table steps of 45°.

Table 4.3 Values for change of yaw angle measured by sensor for rotary table steps of 45°

Total number of data points	9
Reference change of angle (deg)	45.0
Mean change of angle (deg)	44.70
Standard deviation	0.26
Uncertainty (deg)	0.20
Maximum outlier difference (deg)	0.79
Limit of agreement (deg)	±0.59
Limit of agreement uncertainty (deg)	±0.34

Figure 4.7 displays the values collected for the step change of 90°. Each data point in the plot represents a change of angle measured from the sensor during a 90° rotation on the rotary table. The error bars for each data point indicate the sensor accuracy and sample precision error uncertainty of ±1.1°. Again, the precision error of the sample means collected for the rotary table steps of 90° are smaller than those measured in the 10° rotary table step measurements. The accuracy error of the sensor is the main contributor to the error in the changes of yaw angle measured by the sensor. Twelve data points were collected using the procedure explained at the beginning of section 4.1.1, utilising a step of 90° measured on the hand dial of the rotary table. The values depicted in Fig. 4.7 are listed in Table 4.4. The mean change of angle varied a small amount from the reference angle with a difference of 0.03° or a percent difference of 0.03%. This is the smallest difference measured in comparison to the step changes of 1°, 10°, and 45°. The maximum outlier measured a difference from the reference of 0.54° or a percent difference form the reference of 0.60%. This is also a smaller difference measured than the 10° and 45° step. The twelve measured changes of angle fall between 2.201 standard deviations from the sample mean change of 89.97° with a confidence of 95%. This is an interval of 90.93° to 89.02° illustrated as dashed lines in Fig. 4.7.

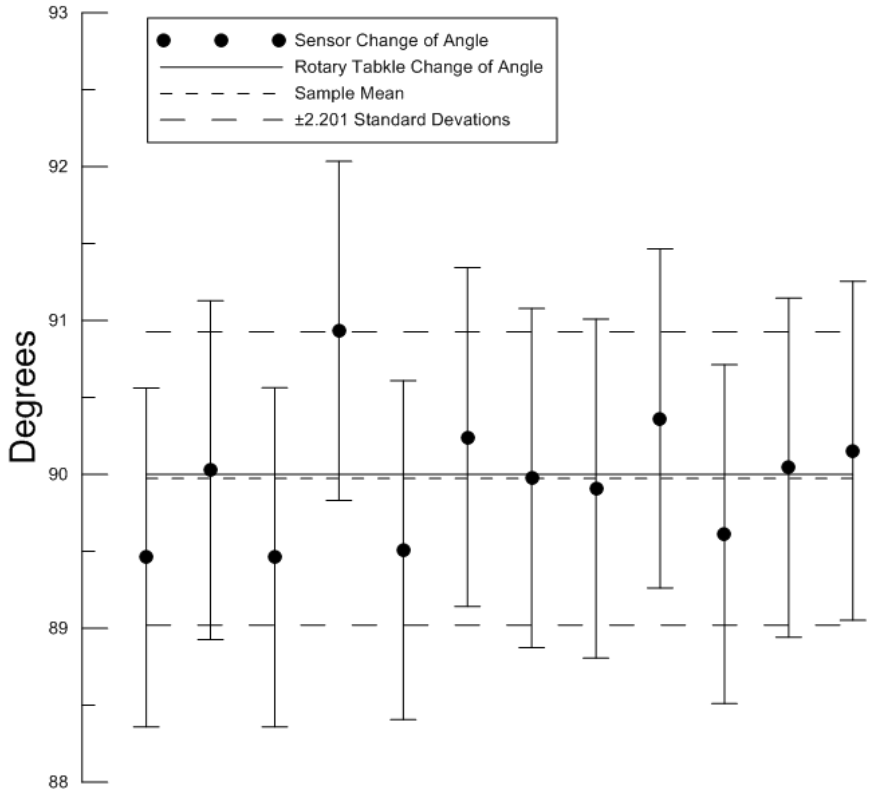

Figure 4.7 Change of yaw angle measured by sensor for rotary table steps of 90°.

Table 4.4 Values for change of yaw angle measured by sensor for rotary table steps of 90°

Total number of data points	12
Reference change of angle (deg)	90.0
Mean change of angle (deg)	89.97
Standard deviation	0.43
Uncertainty (deg)	0.28
Maximum outlier difference (deg)	0.54
Limit of agreement (deg)	±0.95
Limit of agreement uncertainty (deg)	±0.48

The largest limit of agreement for the yaw orientation measurement 2.81° ± 1.40° during the measurement of a 10° angle change. The sensor relies on magnetometer measurements as a yaw heading which are affected by soft iron effects due to the sensors proximity to the steel plate of the sensor package and the steel of the rotary table used to perform the rotation. Due to this the yaw measurement will be expected to be less accurate than the pitch and roll measurements.

4.1.2. Pitch angle measurement

The pitch angle (θ) measures the angle about the y axis of the IG-500A AHRS. The sensor package was mounted in the rotary table vice parallel to the ground with the rotary table mounted vertically perpendicular to the ground such that rotations are made about the sensor y-axis. The sensor package was rotated through angle changes in steps of 10° and 1°. Larger changes of angle were not measured as they were for yaw angle (ψ) in order to avoid the IG-500A from measuring angles which cross through the -90° to 90° range. The range of measurement for pitch angle is -90° to 90° for the IG-500A as gimbal lock occurs when the IG-500A approaches these pitch angles as descried in section 3.2. The measurements taken for rotating the sensor package in four steps of 10° are shown in Fig. 4.8.

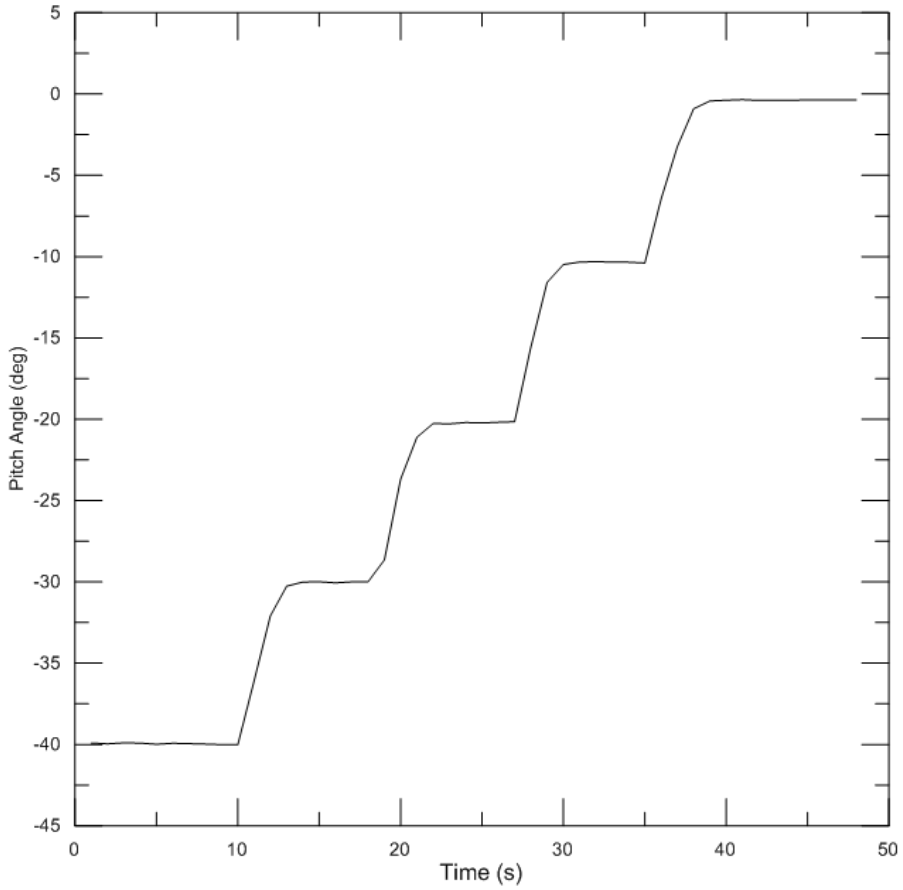

Figure 4.8 Pitch angle measurement in steps of 10°.

The measured step changes for steps of pitch orientation of 1° are shown in Fig. 4.9. Each data point in the plot represents a change of angle measured from the sensor during a 1°

rotation on the rotary table. The error bars for each data point indicate the combined sensor accuracy and sample precision error uncertainty of ±1.1°. For step changes of 1°, fifteen steps were measured using the procedure described at the beginning of section 4.1.1. Figure 4.9 displays lines for the reference change in angle of 1° and the dashed lines for the upper and lower limits of agreement. Table 4.5 lists the values that are shown in Fig. 4.9. The mean value of change of angle varied little from the reference change of angle with a difference of 0.01° or a percent difference of 0.64%. The maximum outlier measured was 0.73° with a greater difference of 0.27° or a percent difference from the reference of 27.06%. The fifteen measured changes of angle fall within 2.145 standard deviations from the sample mean of 1.01° with a confidence of 95%. This is an interval of 1.28° to 0.73° illustrated as the dashed line in Fig. 4.9. This corresponds to a maximum difference of 0.28° from the reference measurement of 1° made on the rotary table, a percent difference of 27.81%.

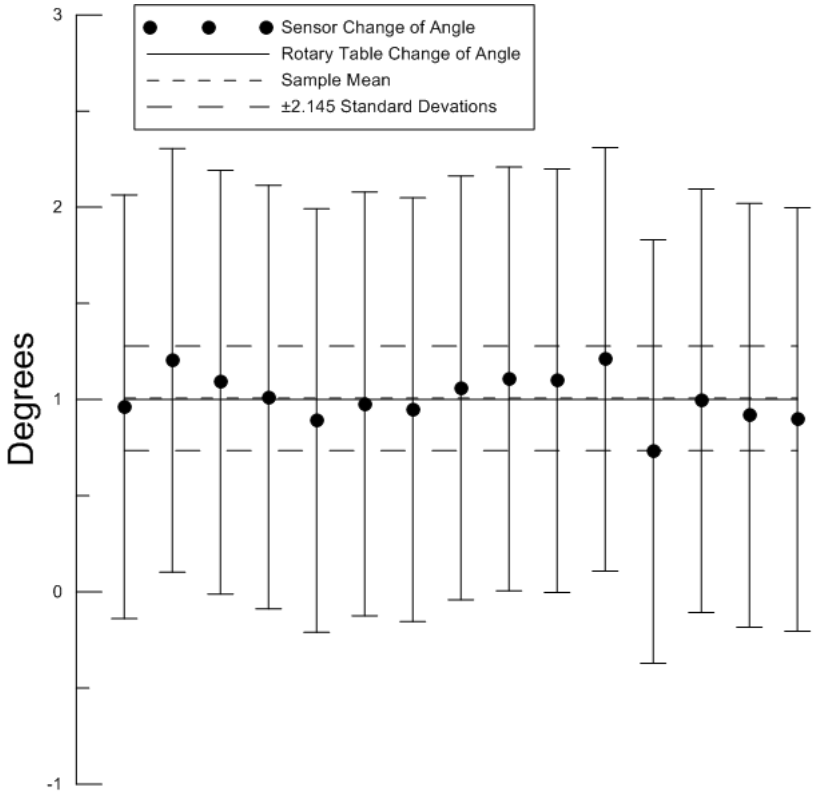

Figure 4.9 Change of pitch angle measured by sensor for rotary table steps of 1°.

Table 4.5 Values for change of pitch angle measured by sensor for rotary table steps of 1°

Total number of data points	15
Reference change of angle (deg)	1.0
Mean change of angle (deg)	1.01
Standard deviation	0.13
Uncertainty (deg)	0.07
Maximum outlier difference (deg)	0.27
Limit of agreement (deg)	±0.27
Limit of agreement uncertainty (deg)	±0.12

Figure 4.10 displays the values collected for the step change 10°. Each data point in the plot represents a change of angle measured from the sensor during a 10° rotation on the rotary table. The error bars for each data point indicate the combined sensor accuracy and sample precision error uncertainty of ±1.1°. Twelve data points were collected using the procedure explained at the beginning of section 4.1.1 using a step of 10° measured on the hand dial of the rotary table. The values depicted in Fig. 4.10 are summarised in Table 4.6. The mean change of angle varied a small amount from the reference angle with a difference of 0.09° or a percent difference of 0.91%. This is greater than the difference measured in comparison to the step changes of 1°. The maximum outlier measured a difference from the reference of 0.32° or a percent difference of 3.23%. This is also a greater difference measured than for the 1° step. The twelve measured changes of angle fall between 2.201 standard deviations from the sample mean of 9.91° with a confidence of 95%. This is an interval of 10.16° to 9.65° shown by the long dashed lines in Fig. 4.10. This corresponds with a maximum difference of 0.35° from the reference change of angle of 10° made on the rotary table, a percent difference of 3.46%.

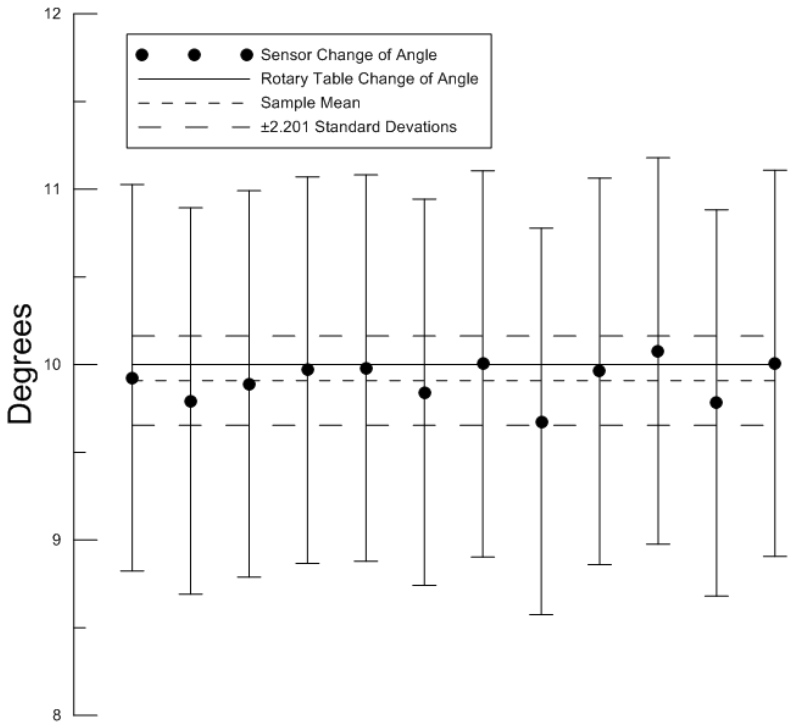

Figure 4.10 Change of pitch angle measured by sensor for rotary table steps of 10°.

Table 4.6 Values for change of pitch angle measured by sensor for rotary table steps of 10°

Total number of data points	12
Reference change of angle (deg)	10.0
Mean change of angle (deg)	9.91
Standard deviation	0.12
Uncertainty (deg)	0.07
Maximum outlier difference (deg)	0.32
Limit of agreement (deg)	±0.25
Limit of agreement uncertainty (deg)	±0.13

Similar limits of agreement for changes of pitch angle of 1° and 10° were found to be 0.27 ± 0.12° and 0.25 ± 0.13° respectively. As expected the pitch angle limits of agreement are smaller than those found for yaw angle.

4.1.3. Roll angle measurement

The roll angle (ϕ) measures the angle about the *x*-axis of the IG-500A AHRS. Like the procedure for measuring the pitch angle the sensor package was mounted in the rotary table vice parallel to the ground with the rotary table mounted vertically perpendicular to the ground. The sensor package is mounted in the chuck vice of the rotary table such that rotations are made about the sensor *x*-axis. The sensor package was rotated through angle

changes in steps of 90°, 10°, and 1°. The measurements taken for rotating the sensor package in four steps of 10° are shown in Fig. 4.11.

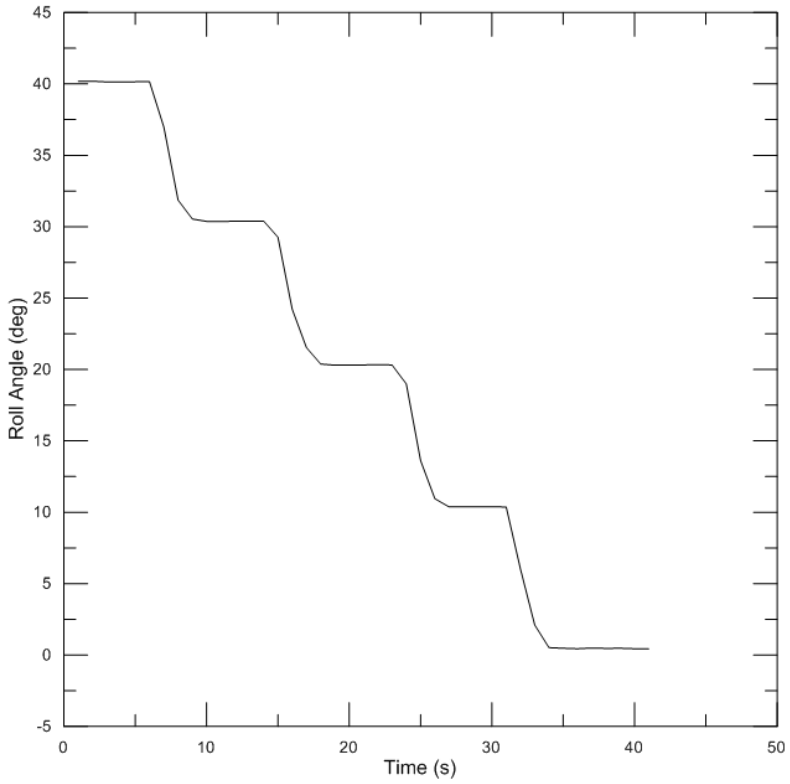

Figure 4.11 Roll angle measurements in steps of 10°.

The measured step changes for steps of pitch orientation of 1° are shown in Fig. 4.12. Each data point in the plot represents a change of angle measured from the sensor during a 1° rotation on the rotary table. The error bars for each data point indicate the combined sensor accuracy and sample precision error uncertainty of ±1.1°. For step changes of 1°, fifteen steps were measured using the procedure described at the beginning of section 4.1.1. Figure 4.12 displays lines for the reference change in angle of 1° and the dashed lines for the upper and lower uncertainty. Table 4.7 lists the values that are shown in Fig. 4.12. The mean value of change of angle varied little from the reference change of angle with a difference of 0.02° or a percent difference of 1.58%. The maximum outlier measured was 0.78° with a greater difference of 0.22° or a percent difference from the reference of 22.19%. This is a similar value to the difference measured for a step of 1° in pitch angle. The fifteen sample changes of angle fall between 2.145 standard deviations from the sample mean of 1.02° with a confidence of 95%. This is an interval of 1.26° to 0.77° shown by the long dashed

lines in Fig. 4.12. This varies by a maximum of 0.26° from the reference change of angle of 1° made on the rotary table, a percent difference of 25.66%.

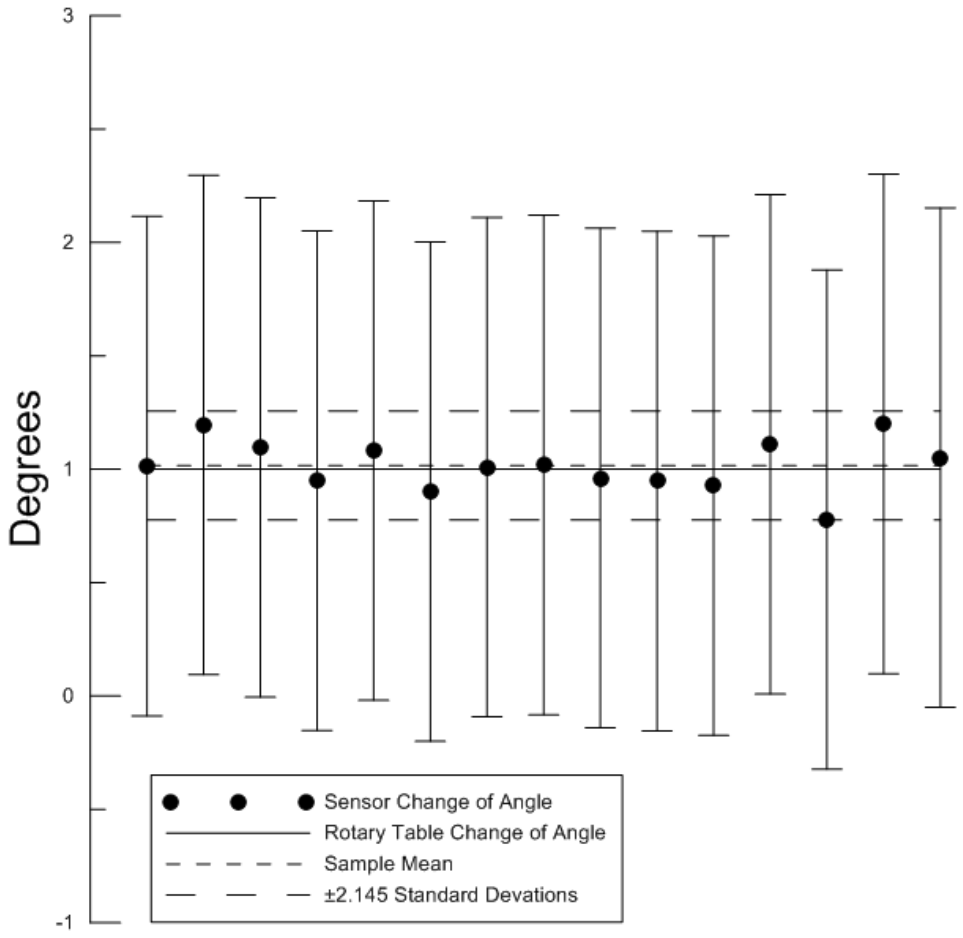

Figure 4.12 Change of roll angle measured by sensor for rotary table steps of 1°.

Table 4.7 Values for change of roll angle measured by sensor for rotary table steps of 1°

Total number of data points	15
Reference change of angle (deg)	1.0
Mean change of angle (deg)	1.02
Standard deviation	0.11
Uncertainty (deg)	0.06
Maximum outlier difference (deg)	0.22
Limit of agreement (deg)	±0.24
Limit of agreement uncertainty (deg)	±0.11

Figure 4.13 displays the values collected for the step change 10°. Each data point in the plot represents a change of angle measured from the sensor during a 10° rotation on the rotary table. The error bars for each data point indicate the combined sensor accuracy and sample precision error uncertainty of ±1.1°. Twelve data points were collected using the procedure explained at the beginning of section 4.1.1 using a step of 10° measured on the hand dial of the rotary table. The values depicted in Fig. 4.13 are summarised in Table 4.8. The mean change of angle varied a small amount from the reference angle with a difference of 0.04 or a percent difference of 0.36%. This is greater than the difference measured in comparison to the step changes of 1°. The maximum outlier measured a difference from the reference of 0.24° or a percent difference of 2.41%. This is a lesser difference measured than for the 1° step. The twelve sample changes of angle fall between 2.201 standard deviations from the sample mean of 9.96° with a 95% confidence. This is an interval of 10.21° to 9.72°, as illustrated by the long dashed lines in Fig. 4.13. This gives a maximum difference of 0.27° from the reference change of angle of 10° made on the rotary table.

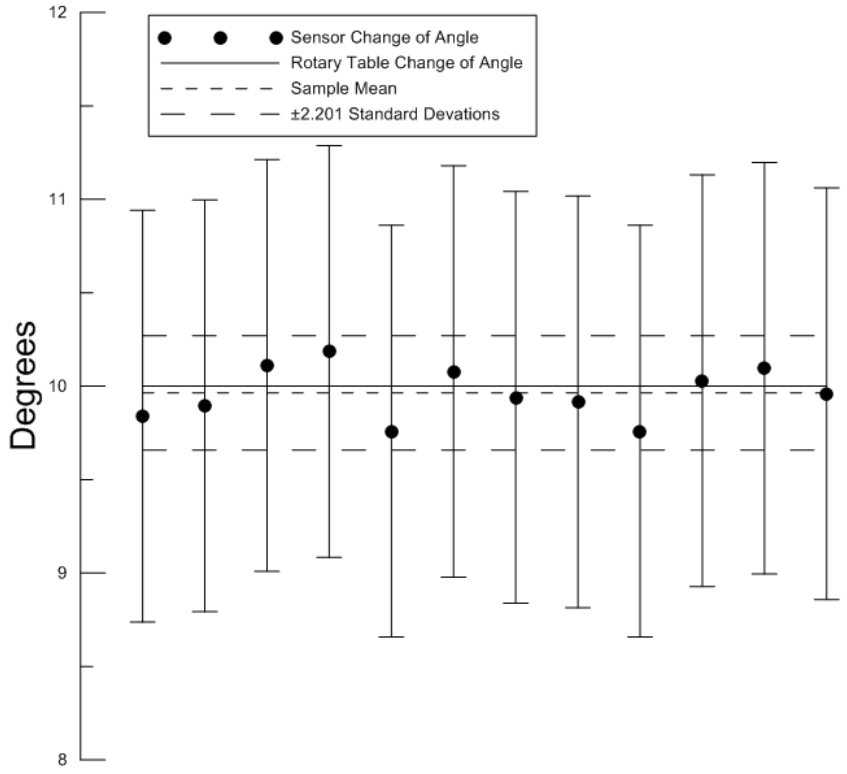

Figure 4.13 Change of roll angle measured by sensor for rotary table steps of 10°.

Table 4.8 Values for change of roll angle measured by sensor for rotary table steps of 10°

Total number of data points	12
Reference change of angle (deg)	10.0
Mean change of angle (deg)	9.96
Standard deviation	0.14
Uncertainty (deg)	0.09
Maximum outlier difference (deg)	0.24
Limit of agreement (deg)	±0.31
Limit of agreement uncertainty (deg)	±0.15

Figure 4.14 displays the values collected for the step change 90°. Each data point in the plot represents a change of angle measured from the sensor during a 90° rotation on the rotary table. Twelve data points were collected using the procedure explained at the beginning of section 4.1.1 using a step of 90° measured on the hand dial of the rotary table. The values depicted in Fig. 4.14 are summarised in Table 4.9. The mean change of angle varied a small amount from the reference angle with a difference of 0.11 or a percent difference of 0.12%. This is greater than the difference measured in comparison to the step changes of 1° and 10°. The maximum outlier measured a difference from the reference of 0.61° or a percent difference from the reference of 0.67%. This is also greater than the difference measured for the 1° and 10° step. The twelve measured changes of angle fall between 2.201 standard deviations from the mean of 89.89°. This is an interval of 90.49° to 89.30° shown by the long-dashed lines in Fig. 4.14. The maximum difference from the reference change of angle of 90° made on the rotary table is 0.70°, a percent difference of 0.78%.

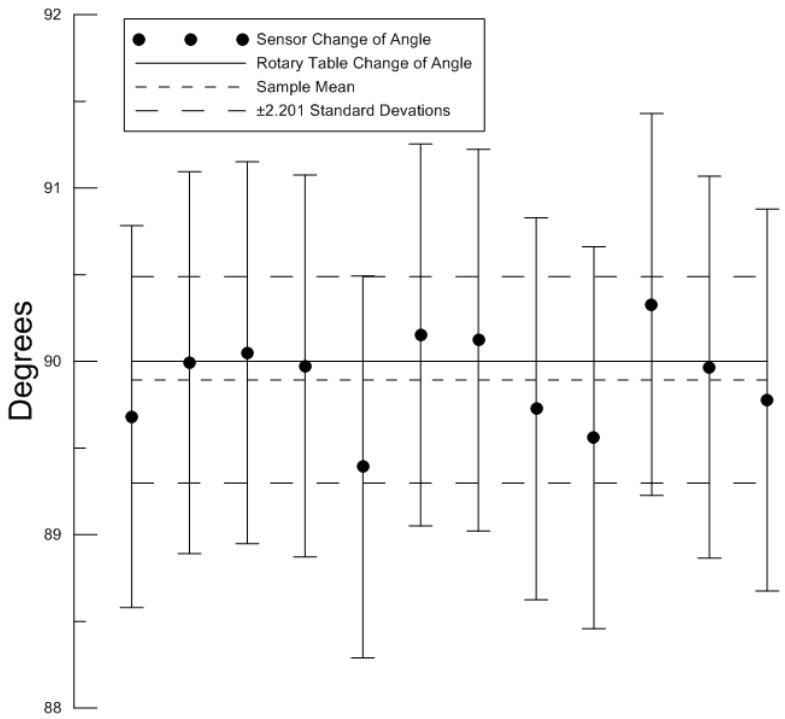

Figure 4.14 Change of roll angle measured by sensor for rotary table steps of 90°.

Table 4.9 Values for change of roll angle measured by sensor for rotary table steps of 90°

Total number of data points	12
Reference change of angle (deg)	90.0
Mean change of angle (deg)	89.89
Standard deviation	0.27
Uncertainty (deg)	0.17
Maximum outlier difference (deg)	0.61
Limit of agreement (deg)	±0.59
Limit of agreement uncertainty (deg)	±0.30

Similar limits of agreement for changes of roll angle of 1° and 10° were found of 0.24 ± 0.12° and 0.31 ± 0.15° respectively. These values are similar to the limits of agreement found for the pitch angle for the same change of angle. The limits of agreement increased to 0.59 ± 0.30 ° for the larger change of angle of 90°. As expected the roll angle limits of agreement are also smaller than those found for yaw angle.

4.1.4. Agreement

The uncertainties calculated for each step angle change for yaw, pitch, and roll demonstrate the accuracy of the orientation measurements retrieved from the IG-500A mounted in the sensor package. The uncertainties measured for yaw, pitch, and roll are summarised in

Tables 4.10, 4.11, and 4.12. The SBG systems specifications indicate that the yaw measurement can be influenced by a ferromagnetic environment due to the readings from sensor's magnetometers. For the yaw angle the greatest uncertainty was found in the measurement of a 10° change in angle. This could have been influenced by a distortion in the magnetic field from the rotary table which is constructed primarily of steel, a ferromagnetic material. In comparison the uncertainties of the pitch and roll angle are much smaller. The pitch and roll angles do not rely on the device's internal magnetometers, instead using only the internal accelerometers and gyroscopes. Comparing the uncertainties found for roll, a greater error was found in the 90° measurement in comparison to the 1° and 10 ° measurement. When using the rotary table to conduct the change in angle a larger shift may introduce more error due to the backlash in the gears in the rotary mechanism of the table.

Figure 4.15 displays the yaw angle measurements as a difference from the reference change of angle for all changes of 90°, 45°, 10°, and 1°. It shows that the mean difference measured by the IG-500A in comparison to the rotary table is 0.04°. With a confidence of 95% the differences in the measured angle fall between 2.012 standard deviations from the mean, a range from -1.35 ± 0.35°to 1.42 ± 0.35° with an uncertainty of ± 0.35°. It also shows that three of forty-eight measured changes of angle fall beyond this interval. The largest outlier is -2.87° which was collected from the reference change of angle of 10° shown in Fig. 4.5.

Figure 4.16 displays the pitch angle measurements as a difference from the reference change of angle for changes of 10° and 1°. The figure shows that the mean difference between the change of angle measured by the rotary table and the IG-500A is 0.04°. The differences in the measured change of angle falls between 0.30 ± 0.089° and -0.23 ± 0.089° which is 2.056 standard deviations from the mean with a confidence of 95%. It also shows that one measured change of angle exceeded this interval with a difference from the reference of 0.32°, 0.02° above the upper limit of the interval.

Figure 4.17 displays the roll angle measurements as a difference from the reference change of angle for all changes of 90°, 10°, and 1°. The figure shows the mean difference between the change of angle measured by the rotary table and the IG-500A is 0.04°. With a 95%

confidence, the differences in the measured change of angle fall between 0.41 ± 0.10° and -0.34 ± 0.10° which is 2.024 standard deviations from the mean. It also shows that two measured changes of angle fall outside of this interval with a maximum outlier of 0.61°, a difference from the upper limit of the interval of 0.20°.

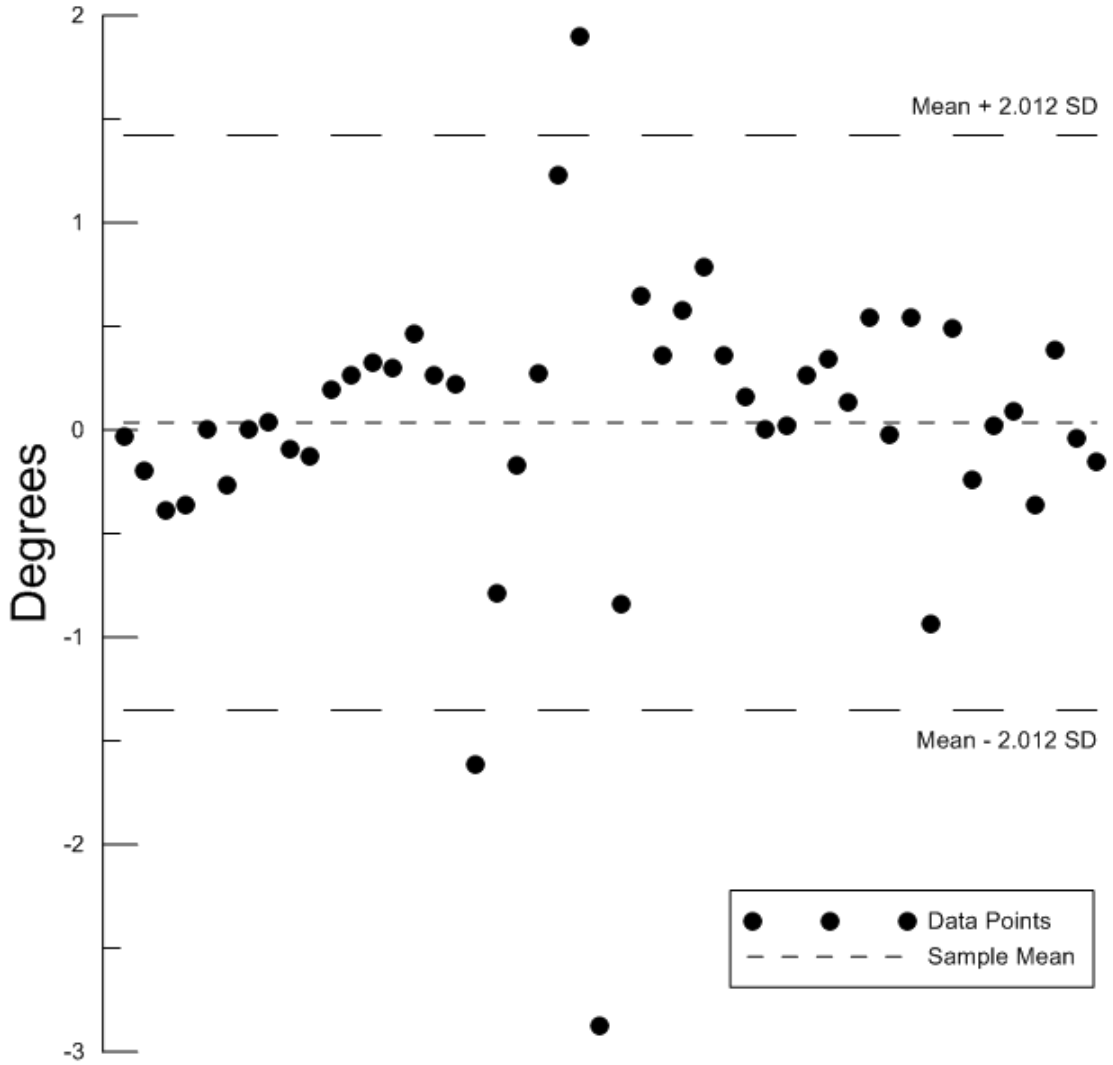

Figure 4.15 Difference in change of yaw angle measured by sensor from rotary table.

Table 4.10 Yaw angle uncertainty

Yaw total difference mean (deg)	0.04
Difference mean ± 2.012 standard deviations (deg)	±1.39
Limit of agreement uncertainty (deg)	±0.35

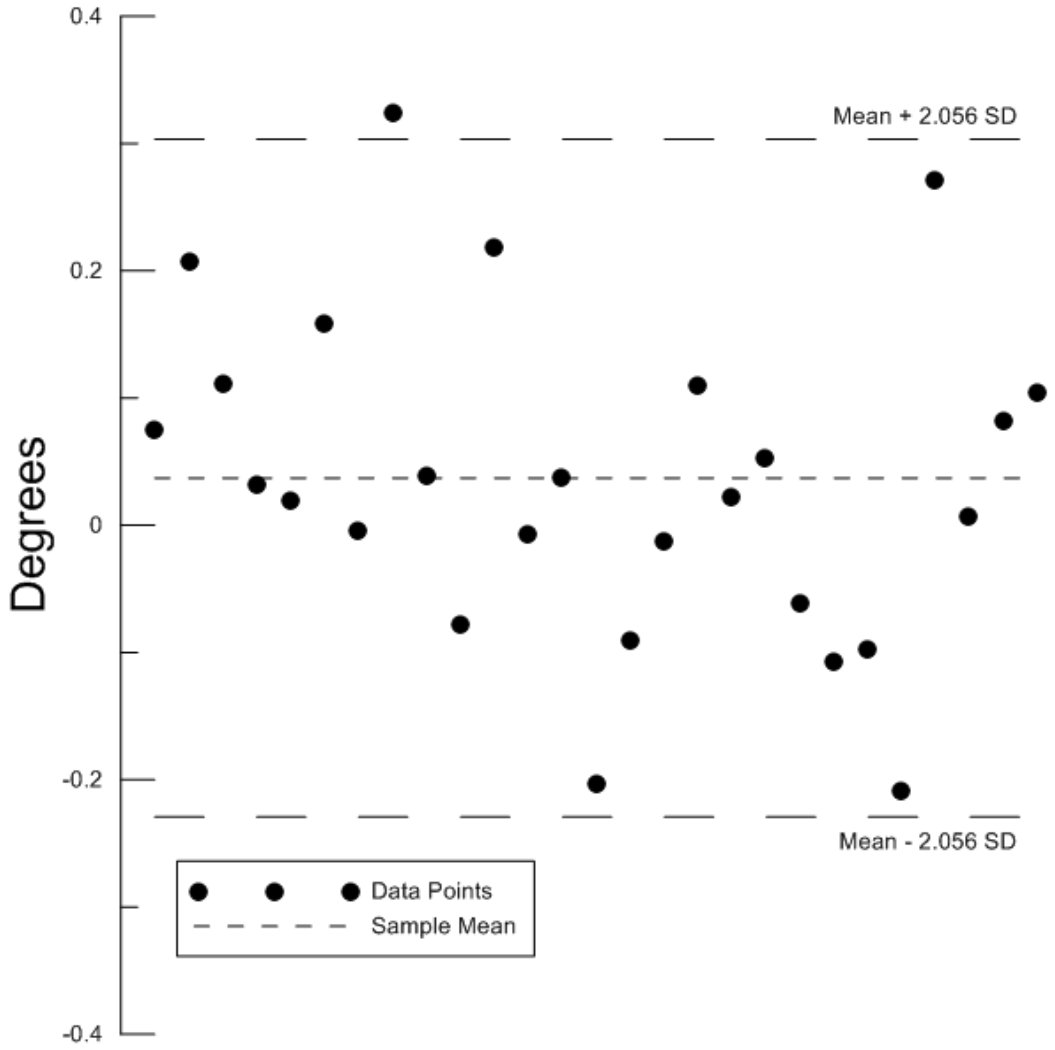

Figure 4.16 Difference in change of pitch angle measured by sensor form rotary table.

Table 4.11 Pitch angle uncertainty

Pitch total difference mean (deg)	0.04
Difference mean ±2.056 standard deviations (deg)	±0.27
Limit of agreement uncertainty (deg)	±0.09

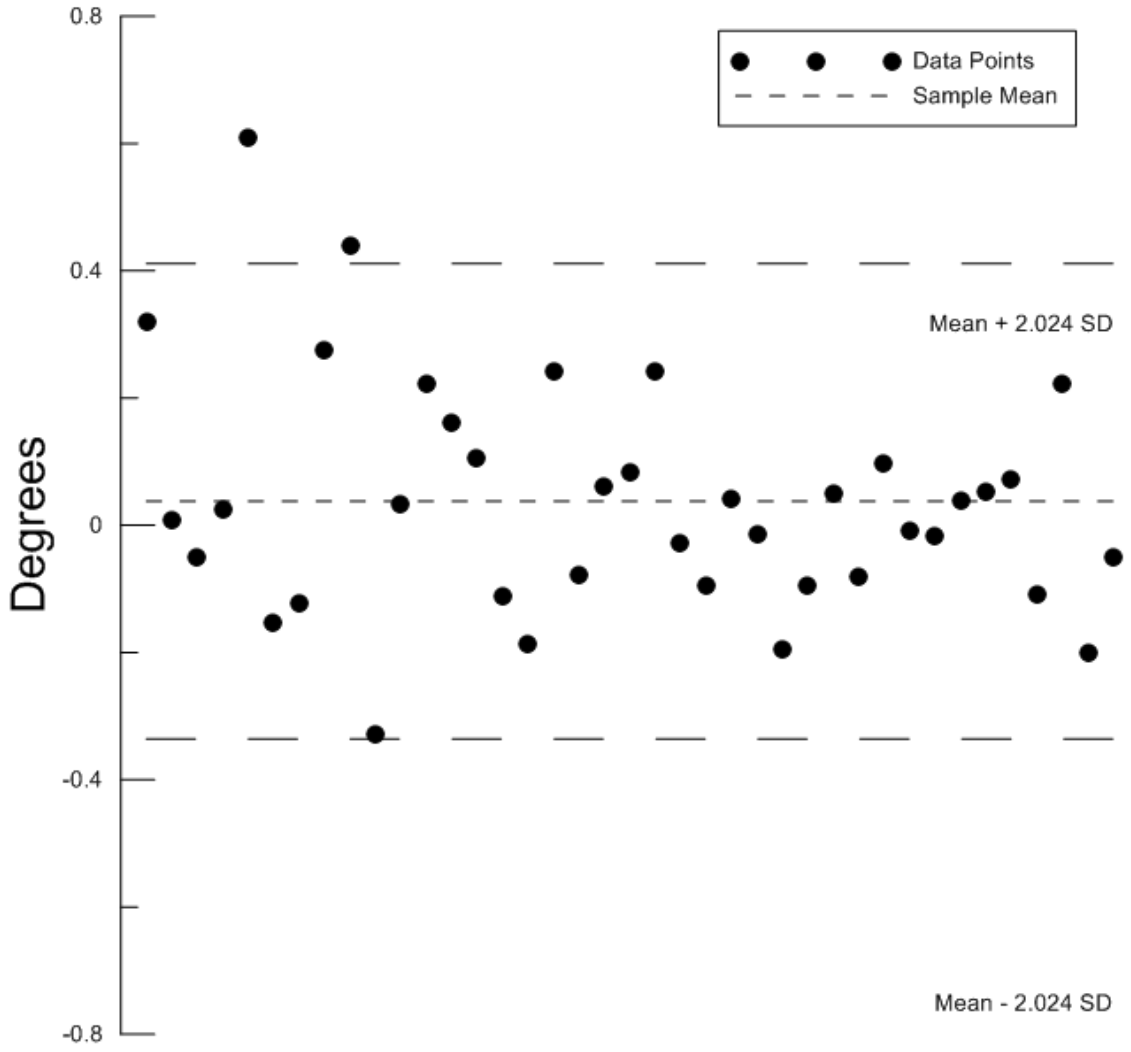

Figure 4.17 Difference in change of roll angle measured by sensor from rotary table.

Table 4.12 Roll angle uncertainty

Roll total difference mean (deg)	0.04
Difference mean ±2.024 standard deviations (deg)	±0.37
Limit of agreement uncertainty (deg)	±0.10

The limits of agreement for pitch, roll, and yaw were determined using the collected measurements from all changes in angle. The pitch and roll angle measurement was found to agree within a smaller interval than the yaw angle. Inaccuracies in the yaw angle are expected due to the IG-500A sensor being mounted to the sensor plate which is made of ferromagnetic material leading to errors in the yaw reading due to soft iron effects.

4.2. Inclined Slope Measurements

Using the accelerometer output from the IG-500A, the velocity of the sensor package can be determined by integrating the accelerometer data. The accuracy of the velocity measurement is expected to be affected by noise in the accelerometer measurement. The sensor package was mounted on to a dolly, shown in Fig. 4.18, and rolled down an inclined track of known length and incline. The track is constructed from two 1.52 m lengths of steel 1" x 1/8" angle bar and inclined at an angle of 20°. Using kinematic equations and a Simulink model of the system, a final velocity is calculated and compared to the velocity calculated from the IG-500A measured accelerometer output.

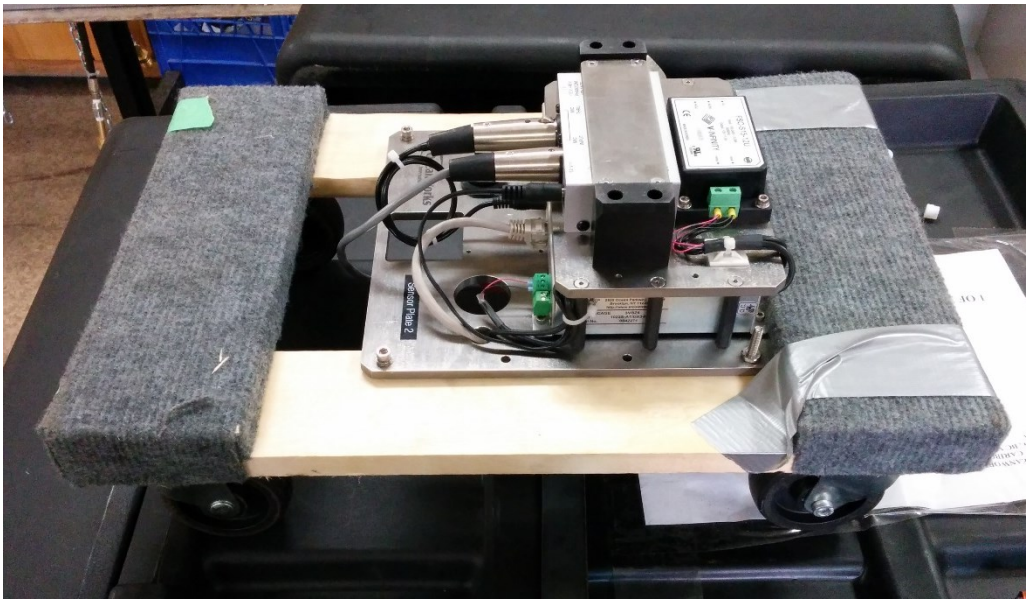

Figure 4.18 Photograph of sensor package mounted to dolly (from author).

In addition to the orientation output of the IG-500A AHRS, the acceleration output is also used to monitor movement of the sensor package. The tri-axial accelerometer of the sensors has the bias errors listed in Table 4.13 in units of mili-gravity.

Table 4.13 Accelerometer Bias

Accelerometer bias at start-up	SB	± 5 mg
Accelerometer in-run stability bias	IRB	± 0.06 mg

Using the accelerometer errors listed in Table 4.13 the uncertainty of the accelerometer measurement is determined to be ± 5 mg or ± 0.05 m/s^2 according to Eq. (4.4).

$$U_A = \sqrt{SB^2 + IRB^2} \tag{4.4}$$

The sensor package was placed at the beginning of the track and left to roll freely. This procedure was repeated eleven times to capture data for eleven runs to be compared to the theoretical result from the kinematic equations and the Simulink model.

Using kinematic equations, the theoretical final velocity of the sensor pack left to roll down the inclined plane under the force of gravity is calculated in Eq. (4.5). As shown in Fig. 4.19, the length of the track is 1.52 m. However, the distance covered by sensor package from the origin of the IG-500A local coordinate system as shown in Fig. 3.4 is 1.07 m. Equation (4.5) gives a theoretical final velocity of 2.67 m/s.

$$v_f{}^2 = v_i{}^2 + 2ad \tag{4.5}$$

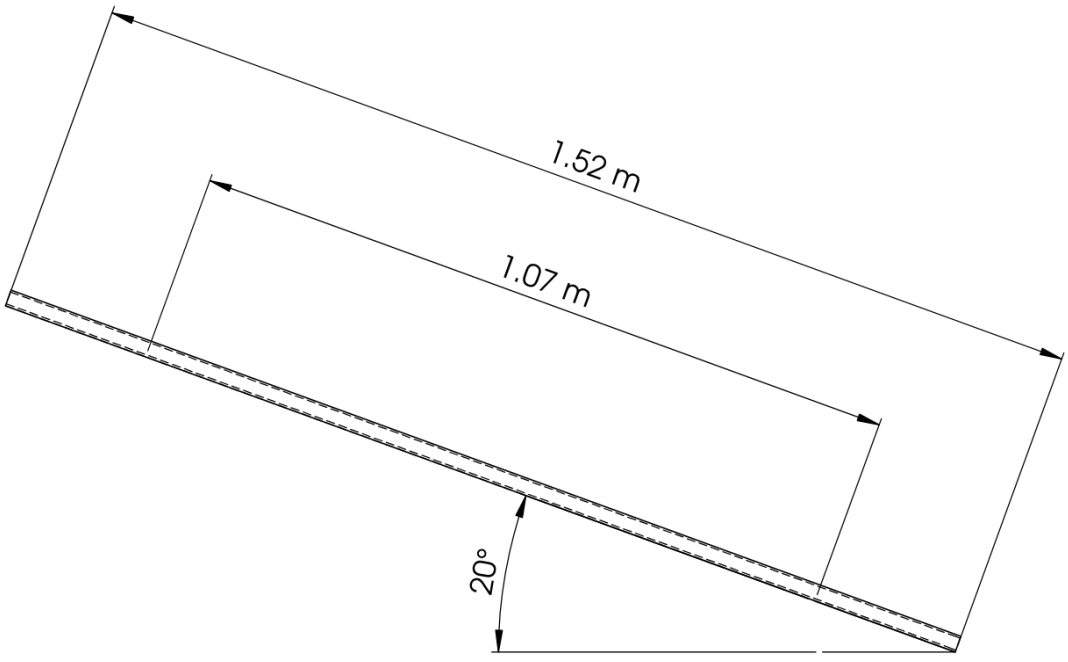

Figure 4.19 Schematic of inclined slope track.

The acceleration outputs from the IG-500A sensor are used to calculate the velocity of the sensor package and compared to the theoretical result calculated in Eq. (4.5). The acceleration output from the first run in the *x, y,* and, *z*-axis is shown in Figure 4.20 for a single test. Data was collected from the sensor package at a sample rate of 50 Hz. In the *y*-axis acceleration, the increases in acceleration followed by a rapid decrease at 0.8 s, indicated by the vertical line in Fig. 4.20, marks the time at which the cart collided with the stop at the end of the track. Figure 4.21 depicts the acceleration, velocity, and the theoretical final velocity calculated in Eq. (4.5) for a single test. The final velocity measured for the cart before the cart collides with the stops is 2.67 m/s. The figure shows that the sensor package does not reach the predicted final velocity at the time it hits the stops and the acceleration signal increases.

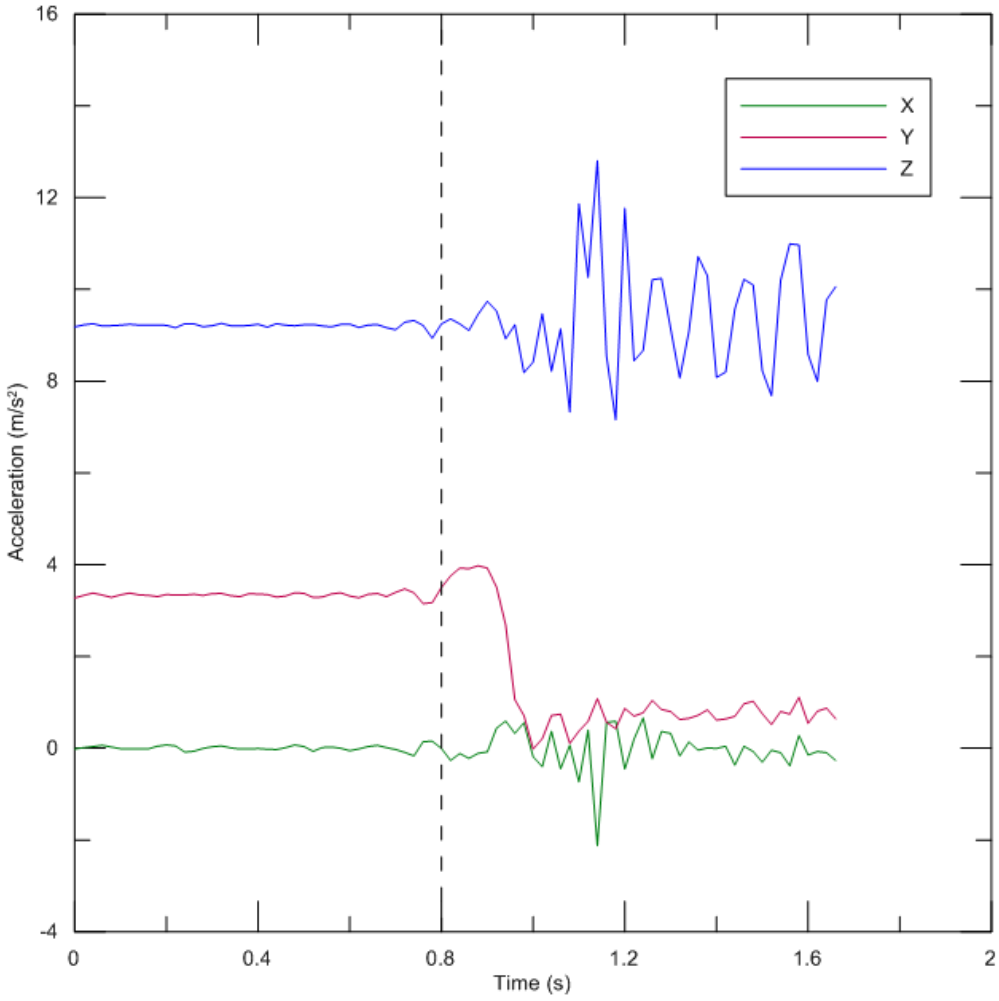

Figure 4.20 Accelerometer signal during incline test.

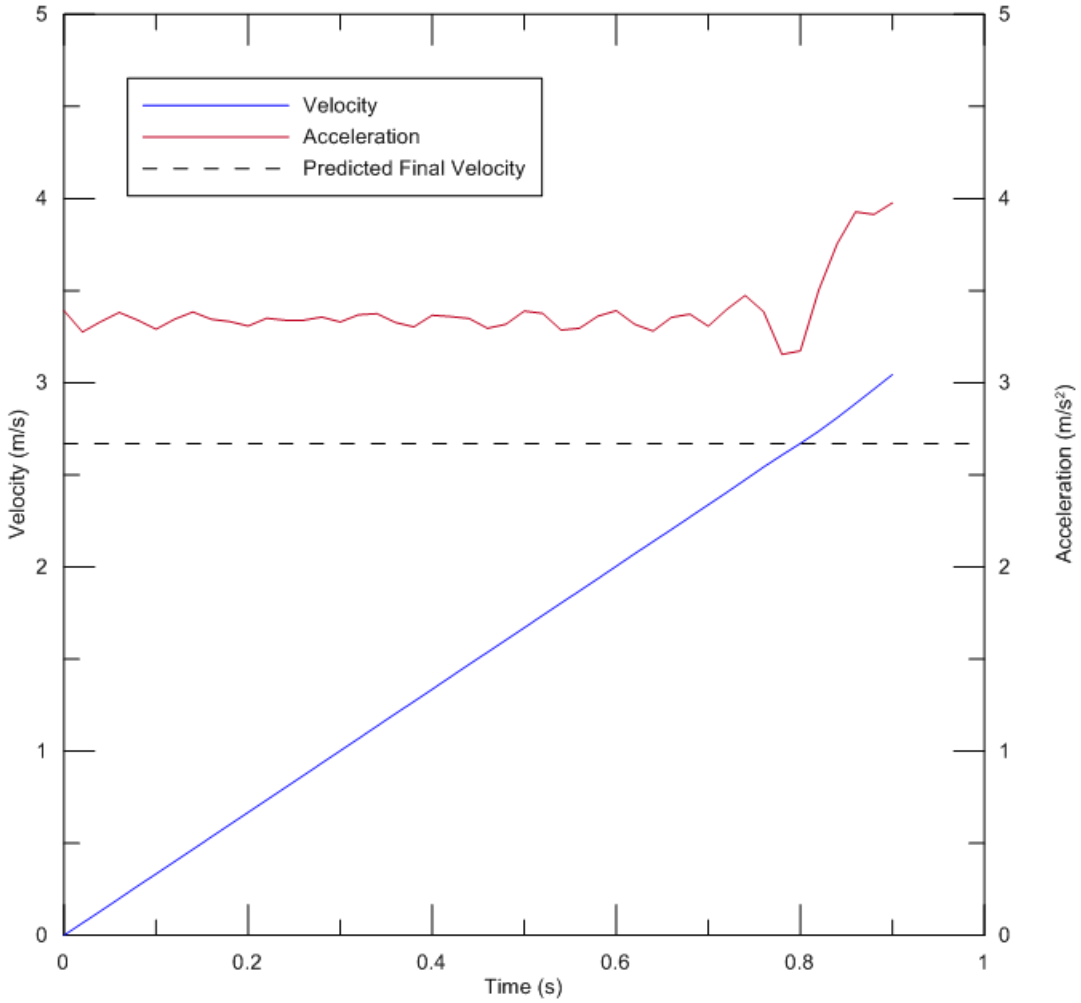

Figure 4.21 Velocity during incline test.

The velocities from the measured acceleration output for all eleven runs are compared in Fig. 4.22. The maximum final velocity observed occurred during Run 3 and was 2.72 m/s and the minimum final velocity occurred during Run 11 and was 2.61 m/s.

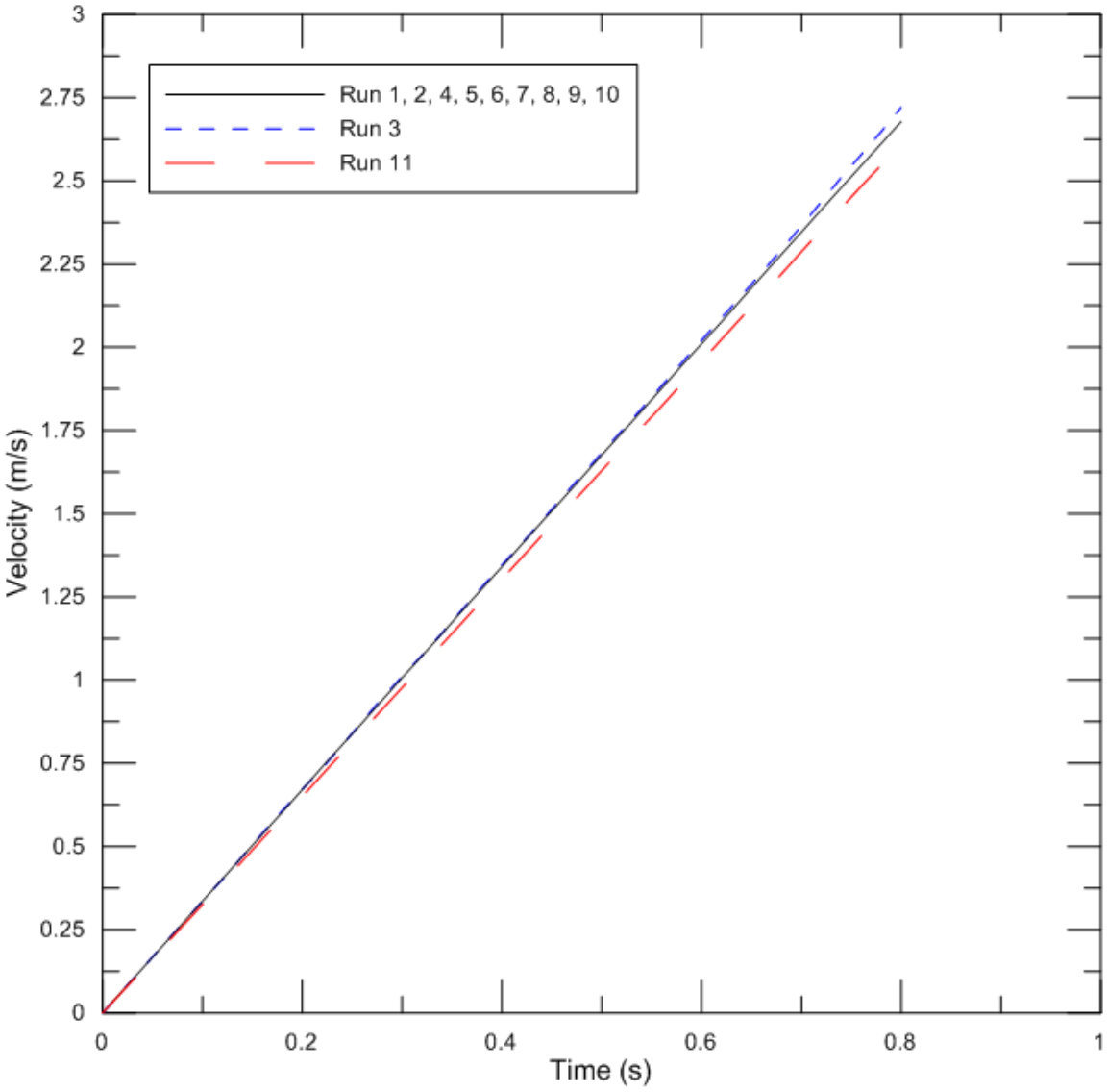

Figure 4.22 Velocities of incline tests.

A Simulink model of the sensor package being rolled along the inclined plane was utilised to account for the presence of rolling resistance encountered during the trials. Figure 4.23 shows the schematic of the Simulink model. The resistances are represented in the model by the variable *c* labeled as damping in Fig. 4.23. The mass (*m*) of the sensor package mounted onto the wheel dolly is 4.781 kg and the damping coefficient (*c)* is -0.01. The damping coefficient was selected to fit the experimental data. The gravitational constant used is 3.35 m/s^2, which corresponds to an angle of 20°.

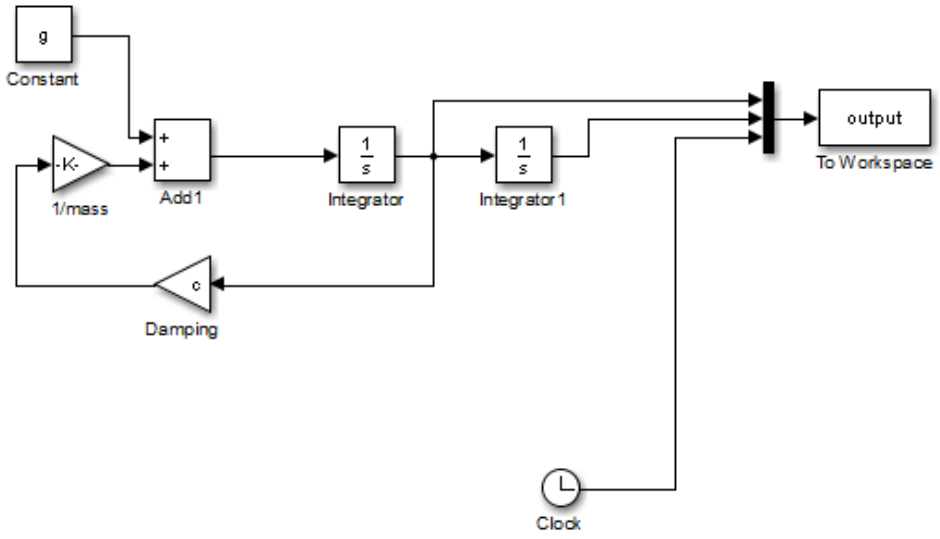

Figure 4.23 Simulink model of sensor package on inclined slope.

In Fig. 4.24 the velocity measured from run 1 of the incline tests is compared to the results from the Simulink model. As time increases the measured velocity decreases in comparison to the model. The model predicts 2.57 m/s while the measured value is 2.50 m/s. The cart experiences friction when rolling down the inclined ramp that varies as the speed of the cart increases and the surface of the ramp changes in roughness. Friction is compensated for in the model using a linear damping coefficient (*c)* which brings the final velocity to a similar value. The integrated velocity from the measured acceleration agrees with the predicted velocity. However, over longer time periods the errors in the acceleration measurement would be expected to decrease the accuracy of the integrated velocity.

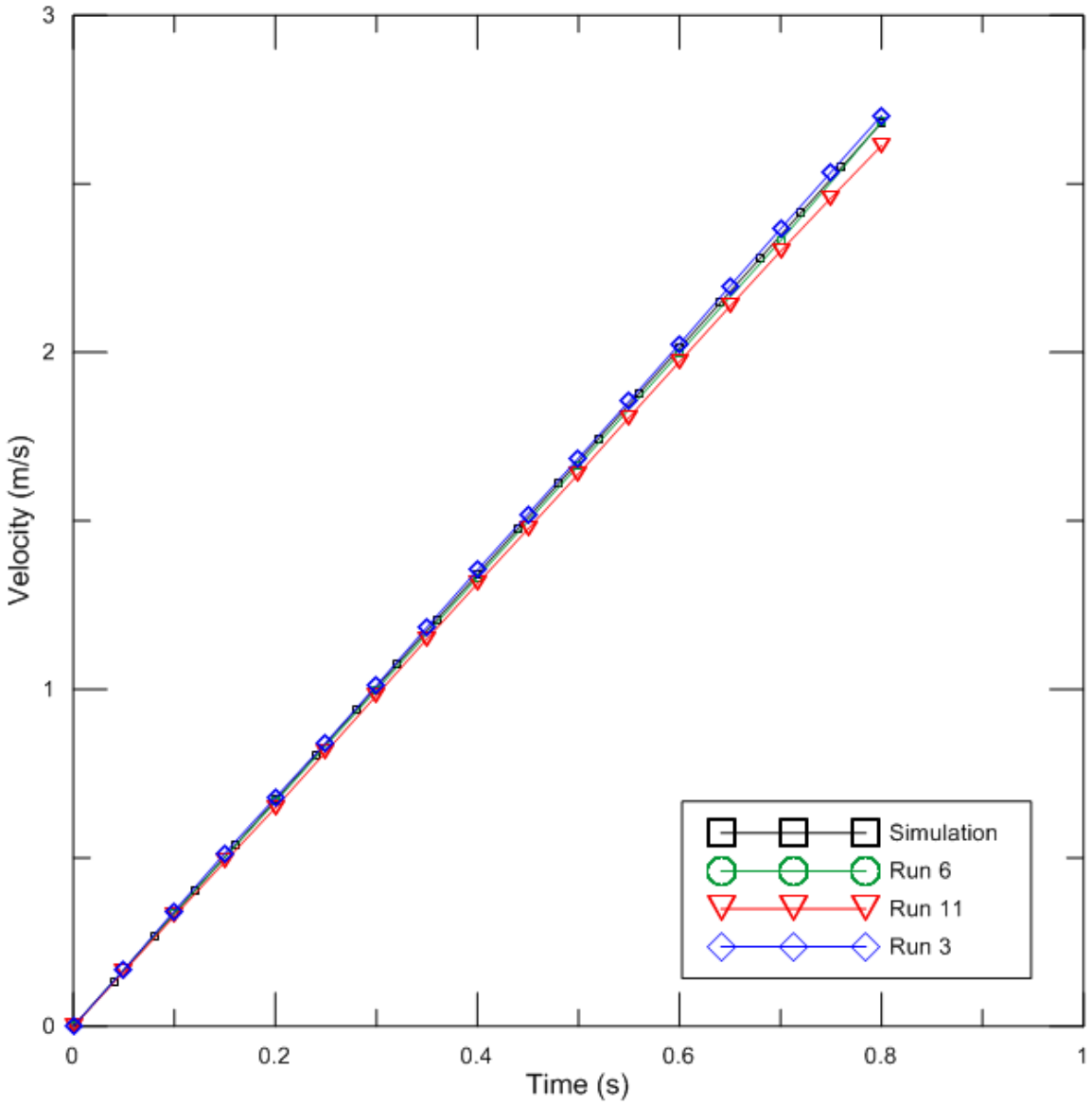

Figure 4.24 Comparison of simulation and incline measurement.

4.3. Summary

The orientation measurements made using the rotary table determined that the pitch, roll, and yaw angle agree closely with the changes of angle measured by the rotary table. The yaw angle showed a greater difference. The yaw angle relies on the sensor's internal magnetometers, which are influenced by the ferromagnetic environment due to being mounted to the sensor plate and secured in the rotary chuck. When the sensor is mounted in the cable abandonment termination, the yaw readings will also be influenced by soft iron effects due to the steel construction abandonment termination.

The sensor package was also rolled down an inclined ramp to compare the velocity calculated from the acceleration output against a theoretical value. Using a Simulink model that accounts for friction encountered by the sensor package as it rolled down the incline, this error was reduced. These measurements as well as the orientation measurements were made over short time periods (approximately 1 s for acceleration measurements and 40 s to 125 s for the orientation measurements). They characterize the accuracy of measurements made in a small window of time. The sensor package will be taking measurements over long periods of times when deployed in the cable abandonment terminations. Therefore, it is also necessary to determine the stability of the measurements over these much longer time periods. The sensor outputs can be expected to be affected by bias instabilities over a longer period of time.

Chapter 5 Event Identification

5.1. Objectives and Overview

In order to use the data collected from the IG-500A in the sensor package to detect movement and changes in the orientation of the cable abandonment termination, the characteristics of the signals from the sensor must be understood while the sensor package is at rest. The values of acceleration and orientation are read from the sensor and compared against a baseline measurement collected from the sensor when it is first connected to the shore station unit. This initial reading is considered the initial resting position of the cable abandonment termination. The collected data is parsed to detect changes in the acceleration and orientation data relative to this baseline to determine if the sensor package has recorded movement of the cable abandonment termination. It is necessary to differentiate changes in the orientation and acceleration data due to error and noise from changes due to movement and change in the cable abandonment orientation.

5.1.1. Variation of AHRS measurements

Data was collected from the IG-500A with the sensor package left at rest for 14 hours to measure variation in the IG-500A sensor signals. SBG Systems (2012) notes that the bias instability of the measurements from the sensor's internal gyroscopes affect the pitch and roll orientation measurements. Over a long period of time a random walk effect of slow changes in the gyroscope bias are expected to be observed (SBG Systems, 2015). The orientation output of the sensor in yaw, pitch, and roll angles as well the tri-axial acceleration output are presented to determine the maximum and minimum values of the signal while the sensor is at rest. The data was recorded at a frequency of 10 Hz.

5.1.1.1. Acceleration Measurements

The acceleration in the *x*, *y*, and *z* axis of the IG-500A during the 14 hour period is shown in Figs. 5.1, 5.2, and 5.3 respectively. A 1 s moving average is presented to demonstrate the variation of the acceleration measurement while the sensor package is left at rest. In the figures, it is shown that the acceleration in the *z*-axis is approximately equal to gravitational acceleration as expected with the sensor package sitting approximately level. Likewise, the acceleration in the *x*-axis and *y*-axis is approximately 0 m/s^2. Comparing the standard

deviation, minimum, and maximum values of the tri-axial accelerometer, the variation in the signals that can be expected from the sensor when the sensor package is at rest can be evaluated.

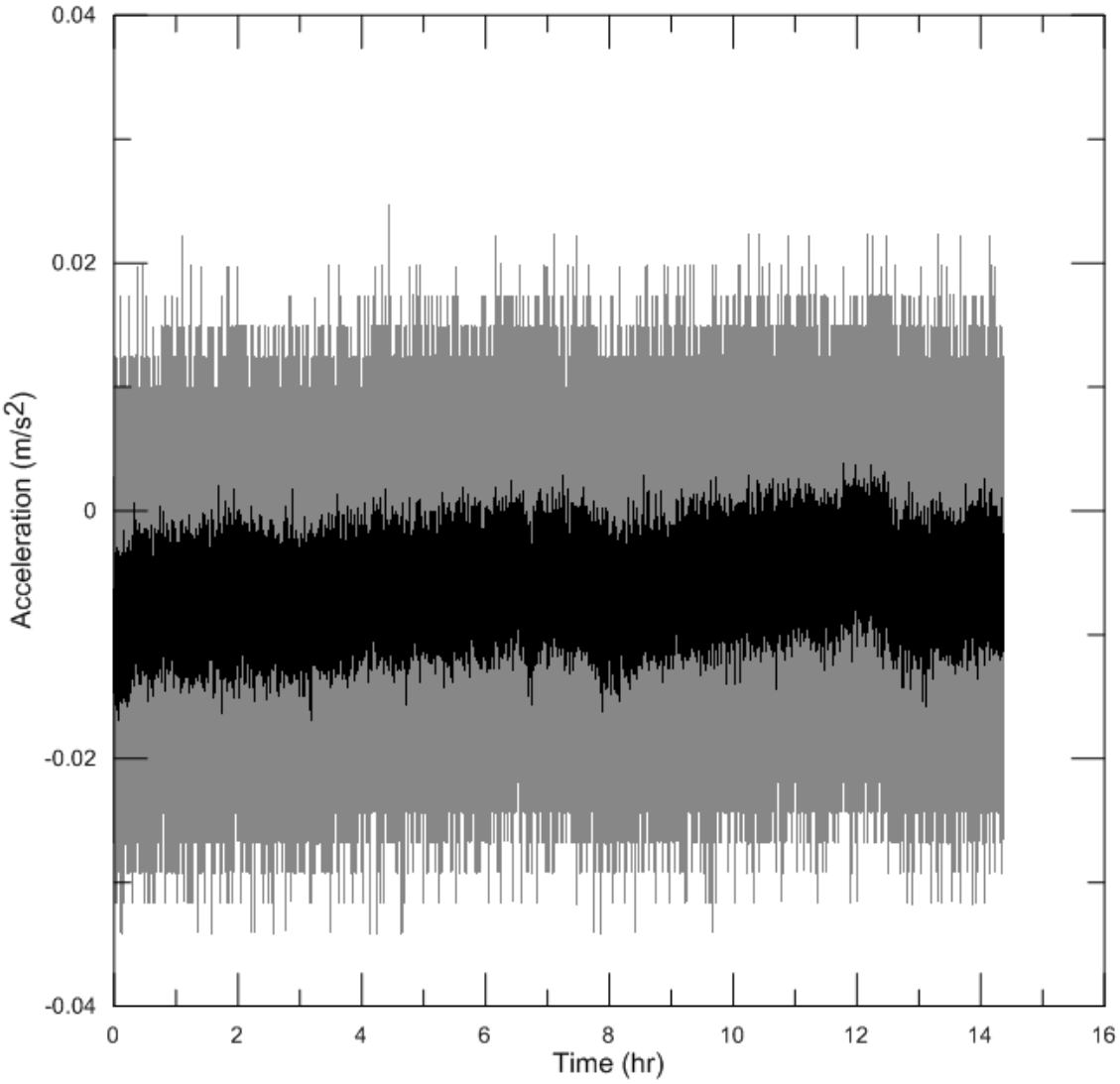

Figure 5.1 Acceleration in *x*-axis sensor package at rest.

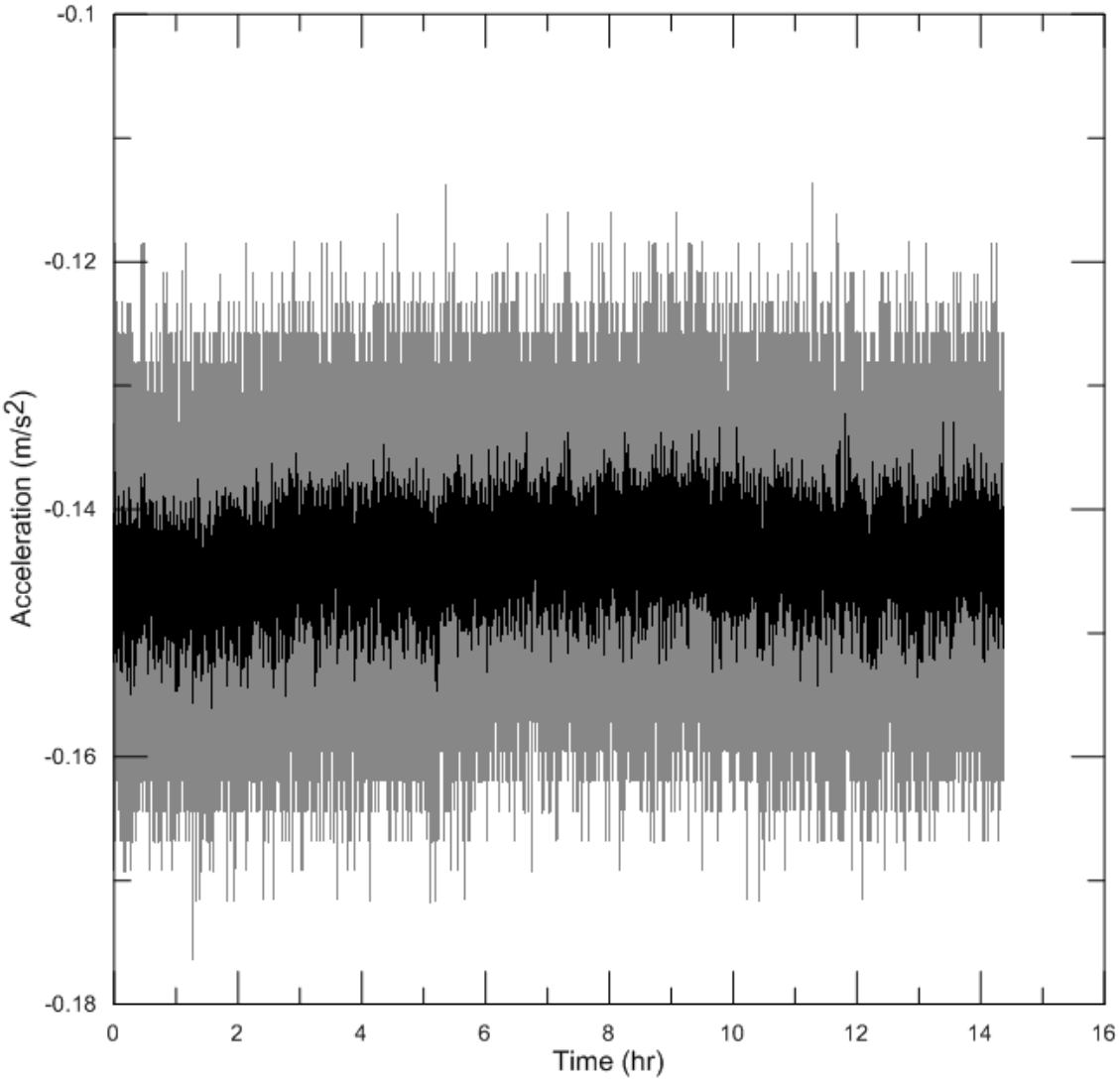

Figure 5.2 Acceleration in *y*-axis sensor package at rest.

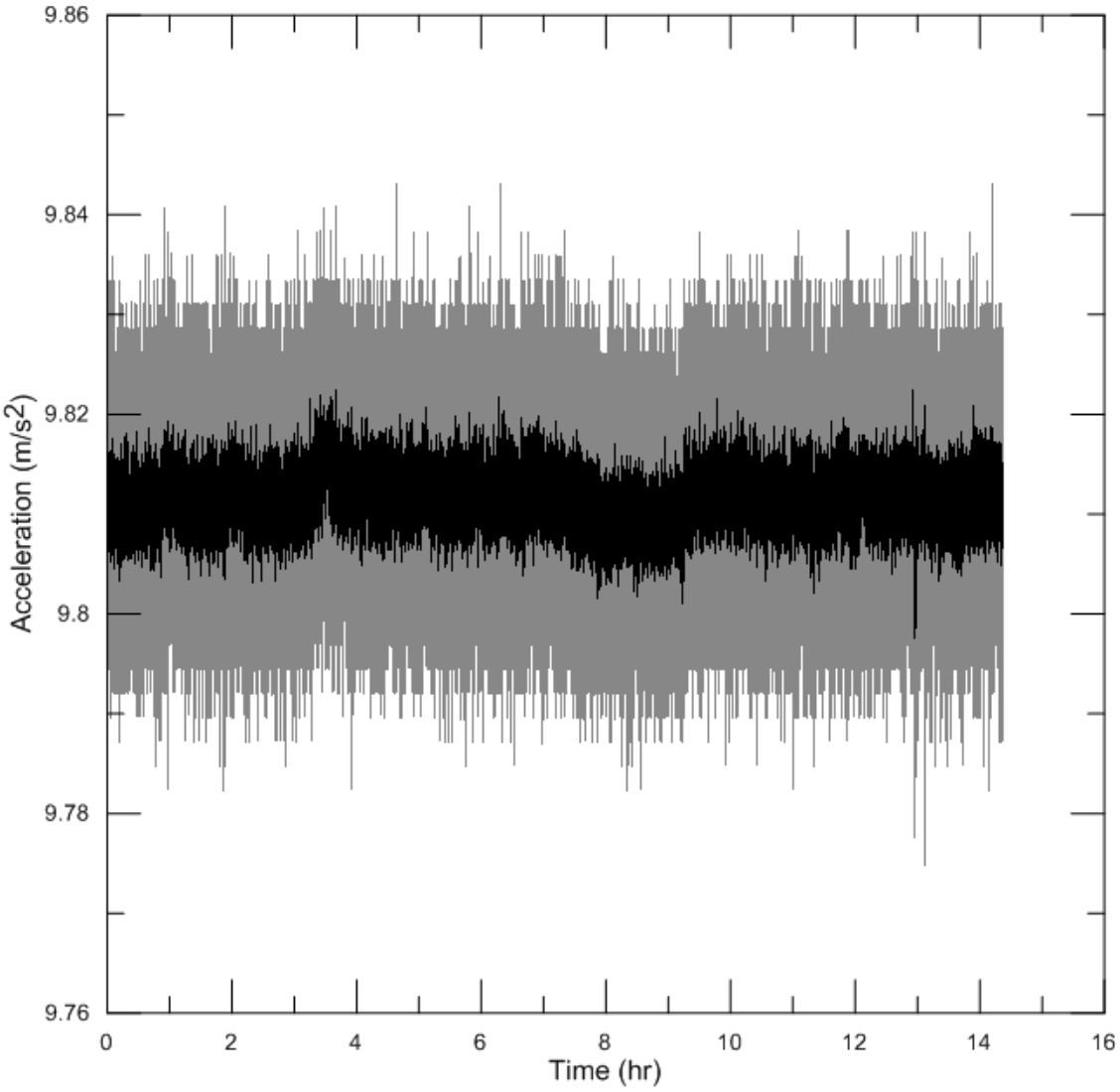

Figure 5.3 Acceleration in *z*-axis sensor package at rest.

The noise density specification for the IG-500A sensor listed in Table 3.2 is 0.25 mg/√Hz where mg is units of mili-gravity per the sampling frequency of the sensor acceleration signal. For a sampling frequency of 10 Hz, as used for collecting data from the sensor plate at rest in Figs. 5.1, 5.2, and 5.3, the noise density gives an RMS noise value of 0.01 m/s^2 as shown in Eq. (5.1). The RMS noise is equal to the standard deviation of the signal. The standard deviations of acceleration signals A_x, A_y, and A_z of the sensor plate at rest are listed in Table 5.1. The table shows that the maximum standard deviation measured is 0.01 m/s^2. This measured standard deviation agrees with the value calculated from the sensor specifications.

$$RMS_{Noise} = 0.25 \frac{mg}{\sqrt{Hz}} \sqrt{10\ Hz} \left(0.001 \cdot 9.81 \frac{m}{s^2}\right) = 0.01 \frac{m}{s^2} \quad (5.1)$$

Table 5.1 Standard deviations of accelerations signals of sensor plate at rest

Standard deviation of x-axis acceleration	0.01 m/s^2
Standard deviation of y-axis acceleration	0.01 m/s^2
Standard deviation of z-axis acceleration	0.01 m/s^2

Using the known maximum standard deviation expected from the acceleration signals the maximum peak to peak values in the signals can be determined. A z-value of 3.3 for a confidence of 99.9% gives an interval of ±0.03 m/s^2 from the mean of acceleration signal. This gives peak to peak difference of 0.05 m/s^2. The measured signal peak to peak values are compared in Table 5.2. The measured peak to peak differences exceed what was predicted using the noise density specification or measured standard deviation. This indicates that in addition to noise in the accelerometer signal there are also changes due to the bias instability of the accelerometer measurements. The shifts in the bias of the accelerometer bias cause the difference of the minimum and maximum value to exceed what is predicted by the noise specification.

Table 5.2 Maximum and minimum acceleration signals of sensor plate at rest

	Maximum	**Minimum**	**Difference**
***x*-axis acceleration**	0.02 m/s^2	-0.03 m/s^2	0.06 m/s^2
***y*-axis acceleration**	-0.11 m/s^2	-0.18 m/s^2	0.06 m/s^2
***z*-axis acceleration**	9.84 m/s^2	9.77 m/s^2	0.07 m/s^2

The root sum acceleration of the sensor package at rest is illustrated in Fig. 5.4. The mean acceleration over the 14 hour period is 9.81 m/s^2. This is equal to the acceleration due to gravity as expected when the sensor package is at rest with no forces acting on it in addition to gravity. Comparing the minimum and maximum values in the signal to the individual acceleration components A_x, A_y, and A_z in Table 5.3 shows that the difference from the maximum to minimum is 0.07 m/s^2. This demonstrates a similar result to A_z as expected due to the orientation of the sensor lying with the z-axis approximately perpendicular to the horizontal such that this component accounts mainly for the gravitational acceleration. Changes in the acceleration measurement can be attributed to changing temperature over the 14 hour measurement period.

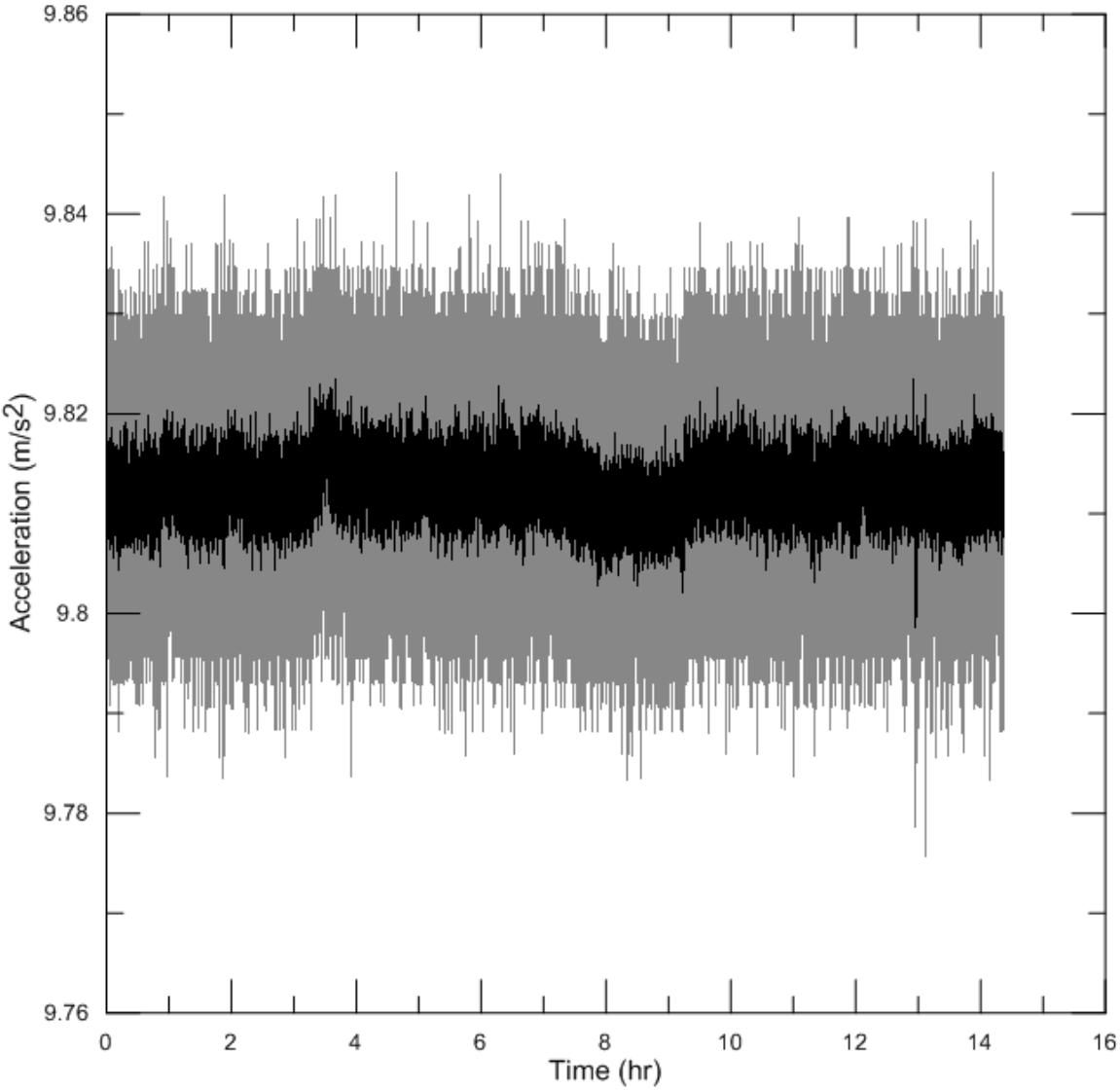

Figure 5.4 Root sum acceleration of sensor package at rest.

Table 5.3 Values of the root sum acceleration of the sensor package at rest

	Mean	SD	Min	Max	Difference
Acceleration (m/s^2)	9.81	0.01	9.78	9.85	0.07

5.1.1.2. Orientation Measurements

In addition to acceleration, the orientation measurements were also analysed. The values of the pitch angle in Fig. 5.5 are listed in Table 5.4. The difference between the minimum and maximum pitch angle measured while the sensor package was at rest is 2.00°. The standard deviation of the pitch angle during the measurement period is 0.27°. Using a *t*-

distribution value of 3.291 for a confidence level of 99.9%, the peak to peak difference from the maximum to the minimum is expected to be 1.80°. However, this difference falls within the 2.00° RMS accuracy of the IG-500A sensor.

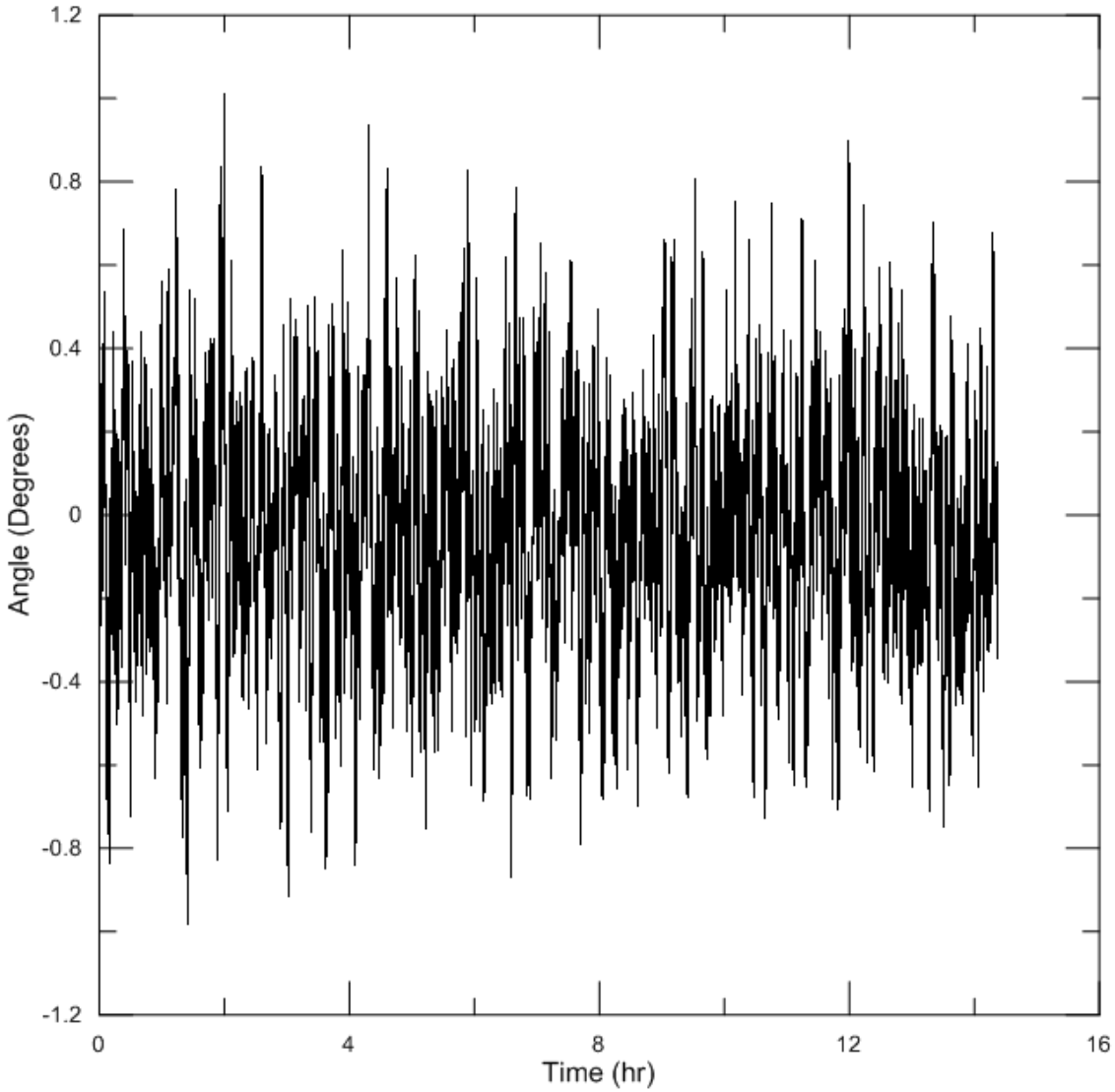

Figure 5.5 Pitch angle sensor package at rest.

Table 5.4 Pitch angle values sensor package at rest

	Mean	SD	Min	Max	Difference
Pitch Angle (deg)	-0.04	0.27	-0.99	1.01	2.00

The values of the roll angle in Fig. 5.6 are listed in Table 5.5. the difference from the maximum to the minimum roll angle measured while the sensor package was at left at rest is 1.71°. The standard deviation of the roll angle signal during the measured period is 0.24°.

Using a *t*-distribution value of 3.291 for a confidence of 99.9%, the peak to peak difference is predicted to be 1.57°. This is less than the measured peak to peak value by 0.13°. This result is consistent with the 2.0° RMS accuracy given by SBG Systems for the sensor. Increasing the confidence percentage would expand the predicted interval and contain the minimum and maximum values that were measured by the sensor. Determining the maximum variation of the roll angle signal when the sensor package is at rest is necessary to determine if the sensor package detects movement without a false positive detection.

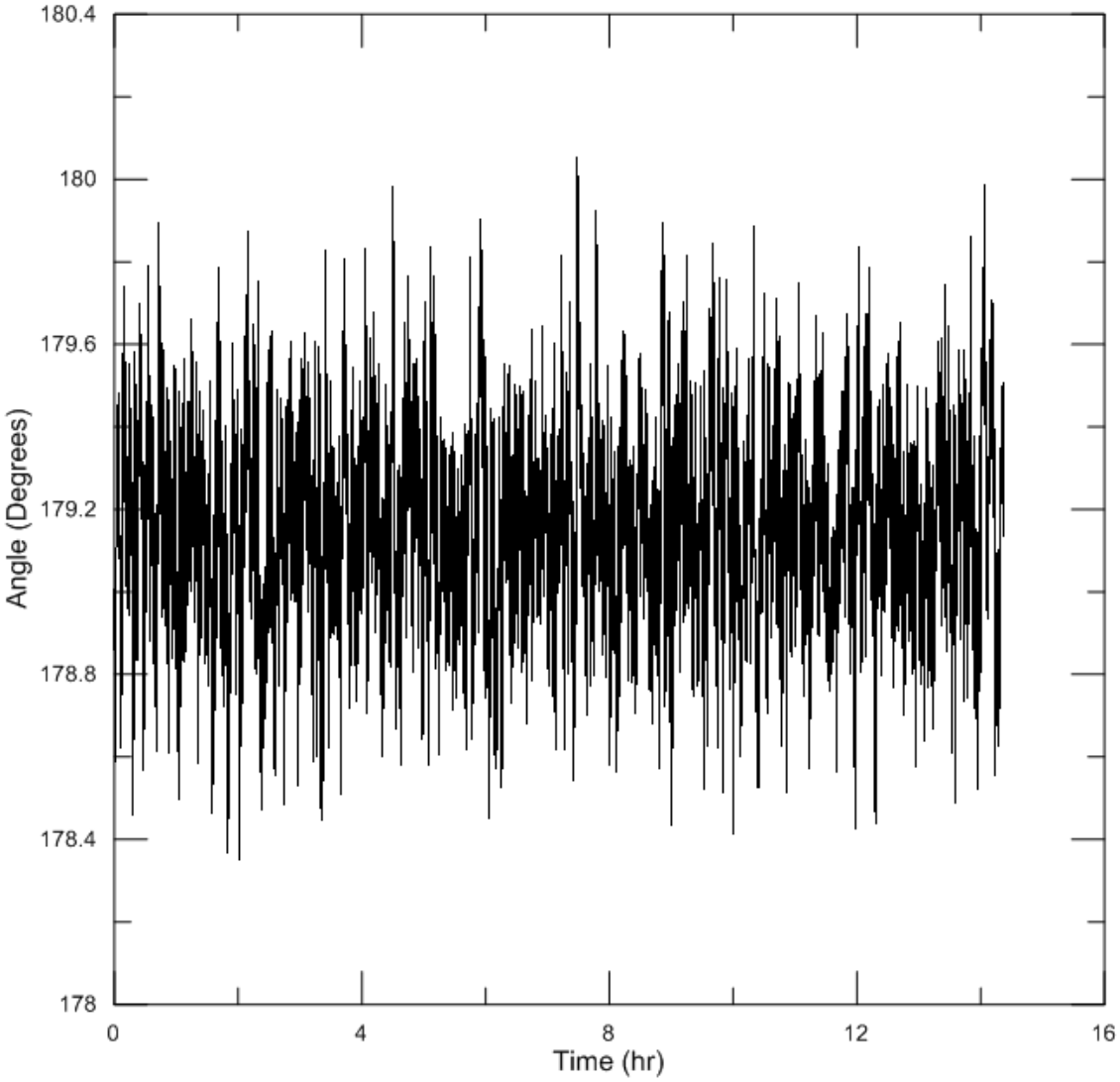

Figure 5.6 Roll angle sensor package at rest.

Table 5.5 Roll angle values sensor package at rest

	Mean	SD	Min	Max	Difference
Roll Angle (deg)	179.16	0.24	178.35	180.06	1.71

The yaw angle while the package is left at rest is shown in Fig. 5.7. As listed in Table 5.6, the yaw angle peak to peak difference from the maximum to minimum is 6.22°. Using a *t*-distribution value of 3.291 for a confidence of 99.9% and the standard deviation of 1.01°, the measured yaw angle is expected to be contained in an interval of ±3.32° from the sample mean of -107.96°. This interval is a difference of 6.63° which is greater than the measured peak to peak difference.

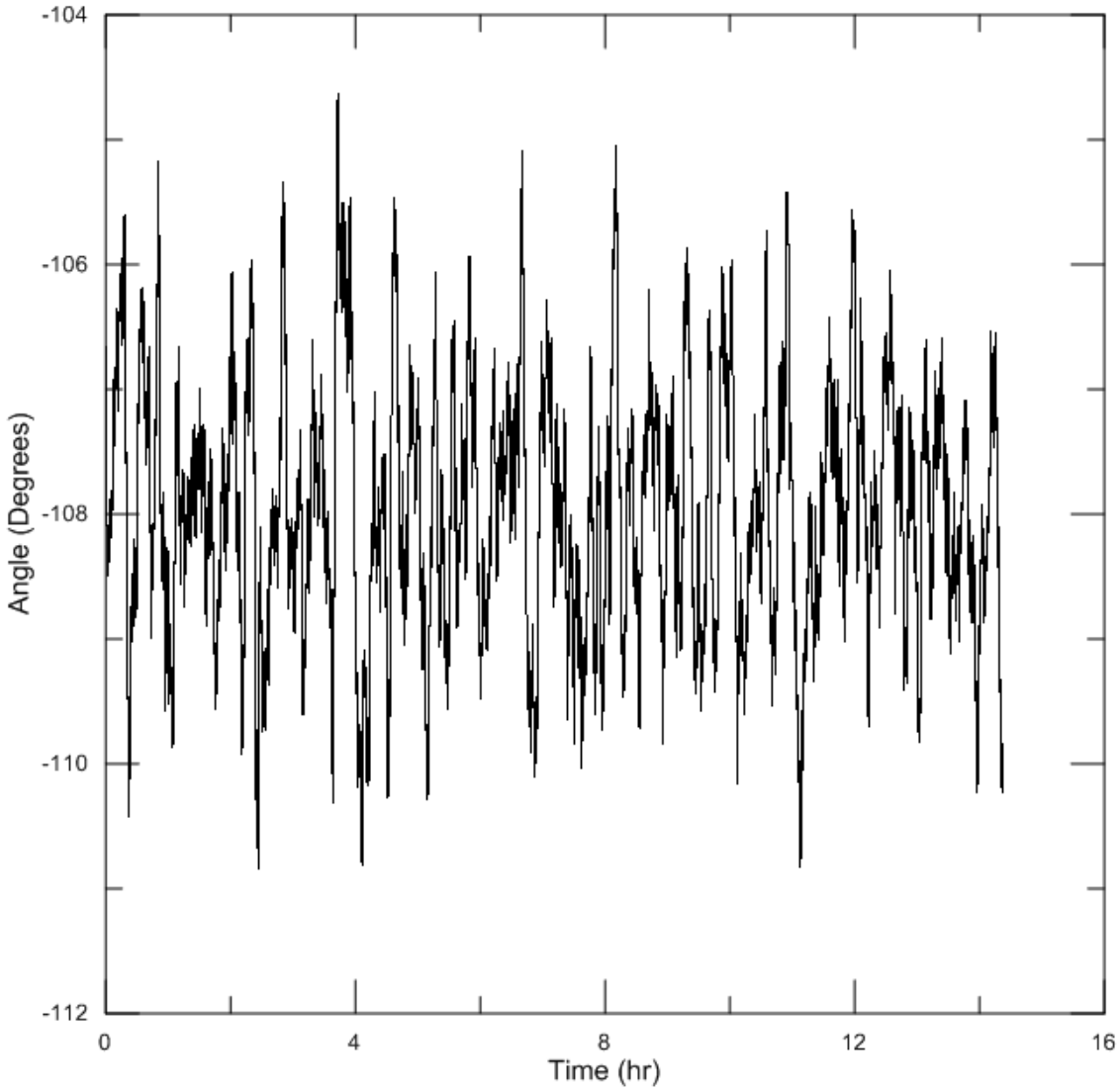

Figure 5.7 Yaw angle sensor package at rest.

Table 5.6 Yaw angle values sensor package at rest

	Mean	SD	Min	Max	Difference
Yaw Angle (deg)	-107.96	1.01	-110.84	-104.62	6.22

The accuracy specification of the IG-500A given by SBG Systems is 2.0° RMS for yaw, pitch, and roll. In comparison, this RMS value than the standard deviations from the measurements made while the sensor package was at rest. Using the 2.0° RMS value to determine the expected range of peak to peak measurements gives ±3.92° with 95% confidence. This is greater than the difference that was measured with the sensor package under static conditions for pitch and roll. However, the yaw angle was found to vary by as much as 3.34° from the mean measurement.

5.2. Implementation

In order to parse the files to determine if a change in the orientation or acceleration measurements from the sensor packages have been recorded, the measurements must be compared against a baseline. The baseline selected is the mean of the initial measurements collected from the sensor packages following the deployment of the cables to their respective berths. Thresholds must be selected for each parameter to determine when a change in the cable abandonment orientation has occurred. When the measurement exceeds or falls below these upper or lower thresholds, movement of the cable will be registered and the timestamp recorded, allowing for further inspection of the data. The thresholds selected for the pitch and roll are based on the accuracy specification for the IG-500A of 2.0° RMS. Given the accuracy 2.0° RMS of the sensor for a 95% confidence level the values of measured pitch and roll can be expected to vary by as much as ±3.9°. This gives an upper and lower threshold of ±3.9° from the baseline pitch and roll measurements to ensure against false positive detections. The yaw angle will not be considered since the IG-500A sensor is being operated in an environment with magnetic distortions due to the ferrous metals of the cable abandonment termination against the recommendation of the sensor manufacturer. The thresholds for the accelerometer are selected based on the bias uncertainty of 0.05 m/s^2. This gives an upper and lower threshold from the baseline measurement of ±0.05 m/s^2 for the accelerometer measurements. A moving average of the sensor measurements will be taken to reduce the impact of noise from the sensor

measurements. When measurements are taken from the deployed sensor packages, data will be collected at a sample rate of 50 Hz. A moving average window of 5 samples will be used equivalent to 10 averages per second.

5.3. Summary

To observe the orientation of the cable abandonment termination for long periods of time measurements are taken from the IG-500A sensor over long periods of time. The measurements over a 14 hour period demonstrated larger variations than those observed over the short time periods in Chapter 4. Thresholds were selected to determine when the measurement has changed beyond the expected variation from the sensor indicating movement of the able abandonment termination.

Chapter 6 Measurements from Deployed Cable

6.1. Baseline measurements

The baseline measurements are the orientation angles and tri-axial accelerations measured by the sensor package when the sensor package was first connected to the shore station unit to retrieve data following cable deployment.

The baseline measurements for Cable A listed in Table 6.1 were retrieved on April 24, 2015. From these values it can be determined that the cable is lying flat on the seafloor at an angle of 1.99 ± 3.92°. Due to the IG-500A sensor being mounted in the termination such that the *x*-axis of the sensor coordinate system is aligned with the longitudinal axis of the cable abandonment termination, the angle is determined as the angle between the sensor *y*-axis in the earth reference frame and its projection onto the *xy*-plane of the earth reference frame.

Table 6.1 Cable A Baseline Measurements

Baseline Measurements	
Roll (deg)	1.95
Pitch (deg)	-22.48
Yaw (deg)	94.61
A_x **(m/s^2)**	-3.72
A_y **(m/s^2)**	-0.29
A_z **(m/s^2)**	-9.06

The baseline measurement for Cable C listed in Table 6.2 were retrieved on February 20, 2015. From the roll angle measurement it can be determined that the termination is lying on the seafloor at an angle 5.02 ± 3.92°, a greater angle from the horizontal than the Cable A abandonment termination. The seabed conditions at berth site C are more uneven with areas of cobbles of boulders.

Table 6.2 Cable C baseline measurements

Baseline Measurements	
Roll (deg)	18.59
Pitch (deg)	73.92
Yaw (deg)	-107.28
A_x **(m/s^2)**	9.42
A_y **(m/s^2)**	-0.84
A_z **(m/s^2)**	-2.55

The baseline measurement for Cable A and Cable C were taken approximately six and four months respectively after the cable deployments that were completed on Oct. 28, 2014. Over the this time when the cable abandonment orientation was not measured it is possible that the abandonment terminations moved on the seabed before settling into the orientation observed at the time of the baseline measurements.

6.2. Cable A

A twelve hour period of data collected at a rate of 50 Hz from the sensor package in the abandonment termination of Cable A on April 29, 2015 is presented to characterise the behavior measured by the sensor package. The data collected between the dates of April 25, 2015 to June 5, 2015 is presented to demonstrate the stability of the cable abandonment termination over a longer measurement period.

The root sum acceleration is shown in Fig. 6.1. The mean of the measured acceleration is 9.80 m/s^2. From the values in Table 6.3 it is shown that the maximum standard deviation was observed in the root sum acceleration with a value of 0.01 m/s^2. This compares closely with the maximum 0.01 m/s^2 observed in the *x*-axis acceleration while the sensor package was at rest. For a sample rate of 50 Hz the RMS noise calculated from the IG-500A specification is 0.02 m/s^2. The difference in the minimum and maximum signal is 0.08 m/s^2. These measurements indicate that there is no additional acceleration acting on the cable abandonment termination beyond gravitational acceleration.

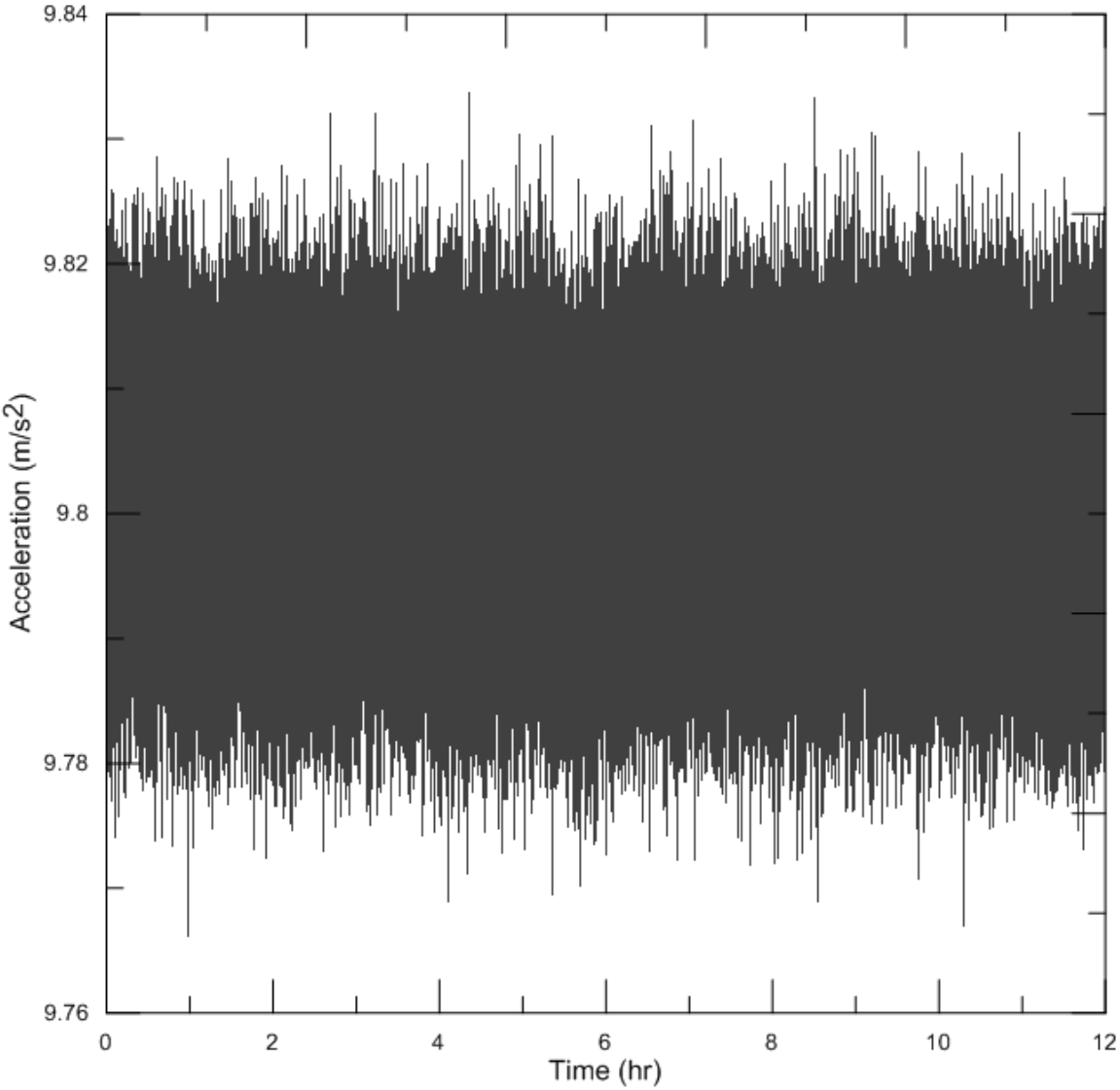

Figure 6.1 Cable A root sum acceleration.

Table 6.3 Standard deviation of acceleration Cable A

Standard deviation of *x*-axis acceleration	0.01 m/s^2
Standard deviation of *y*-axis acceleration	0.01 m/s^2
Standard deviation of *z*-axis acceleration	0.01 m/s^2
Standard deviation of root sum acceleration	0.01 m/s^2

Table 6.4 Minimum and maximum accelerations Cable A

	Mean	**Maximum**	**Minimum**	**Difference**
***x*-axis acceleration**	-3.71 m/s^2	-3.67 m/s^2	-3.75 m/s^2	0.08 m/s^2
***y*-axis acceleration**	-0.31 m/s^2	-0.27 m/s^2	-0.34 m/s^2	0.07 m/s^2
***z*-axis acceleration**	-9.06 m/s^2	-9.03 m/s^2	-9.10 m/s^2	0.07 m/s^2
Root sum acceleration	9.80 m/s^2	9.84 m/s^2	9.76 m/s^2	0.08 m/s^2

In addition to the acceleration measurement from the IG-500A, the orientation measurements are also considered. As observed from the measurements taken of the sensor package at rest prior to installation in the cable abandonment terminations the orientation measurements display greater variation than the acceleration measurements.

The pitch angle of Cable A is shown in Fig. 6.2. The mean value of the pitch angle during the data collection period is -22.27° as listed in Table 6.5. The standard deviation of the collected samples is 0.20°. The signal varied between a maximum of -21.46° to -23.09° giving a maximum observed difference of 1.63°. From the data collected with the sensor package at rest a maximum difference in the pitch angles measured was 2.00°. This difference indicates the changes in the pitch angle measurement are within the expected variation while the sensor package is at rest.

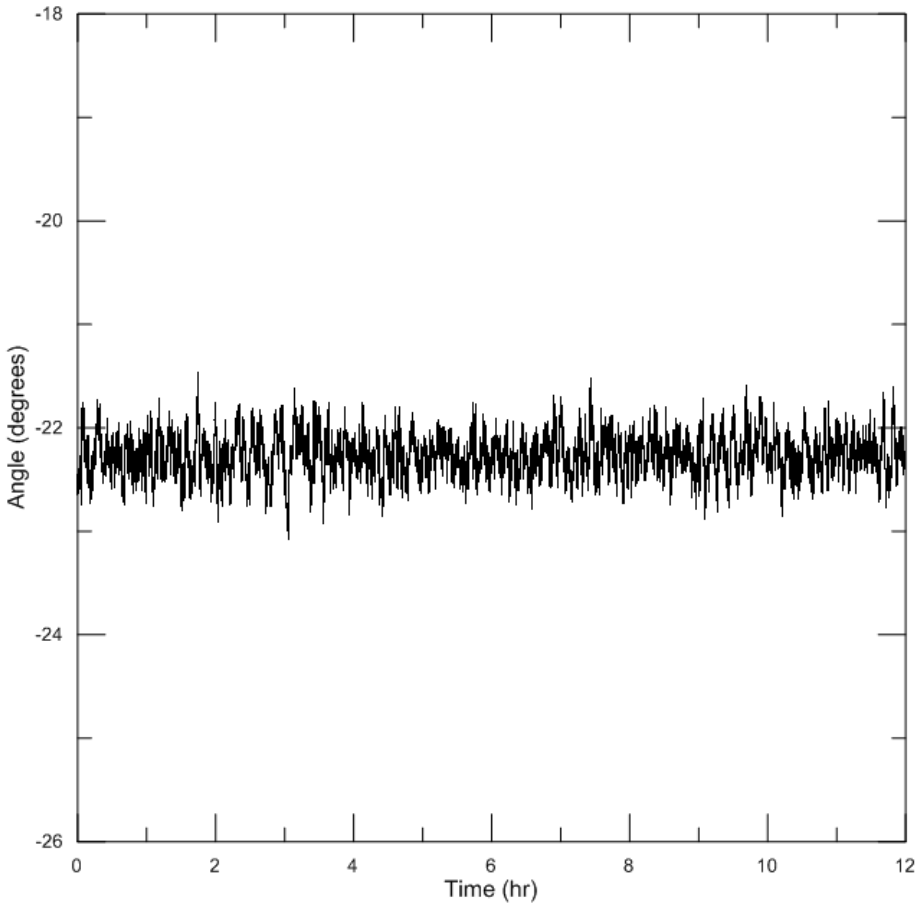

Figure 6.2 Cable A pitch angle.

Table 6.5 Cable A pitch angle

	Mean	SD	Min	Max	Difference
Pitch Angle (deg)	-22.27	0.20	-23.09	-21.46	1.63

The roll angle is presented in Fig. 6.3. The mean of the roll angle measurements over this time period is 1.92° with a standard deviation of 0.24° as shown in Table 6.6. The roll angle signal varied between a maximum of 2.77° and a minimum of 1.17°, giving a maximum difference of 1.60°. Like the pitch angle measurement, this falls below the maximum difference of 1.70° observed while the sensor was at rest in section 5.1.1. This indicates the changes in the roll angle measurement are within the expected variation while the sensor package is at rest.

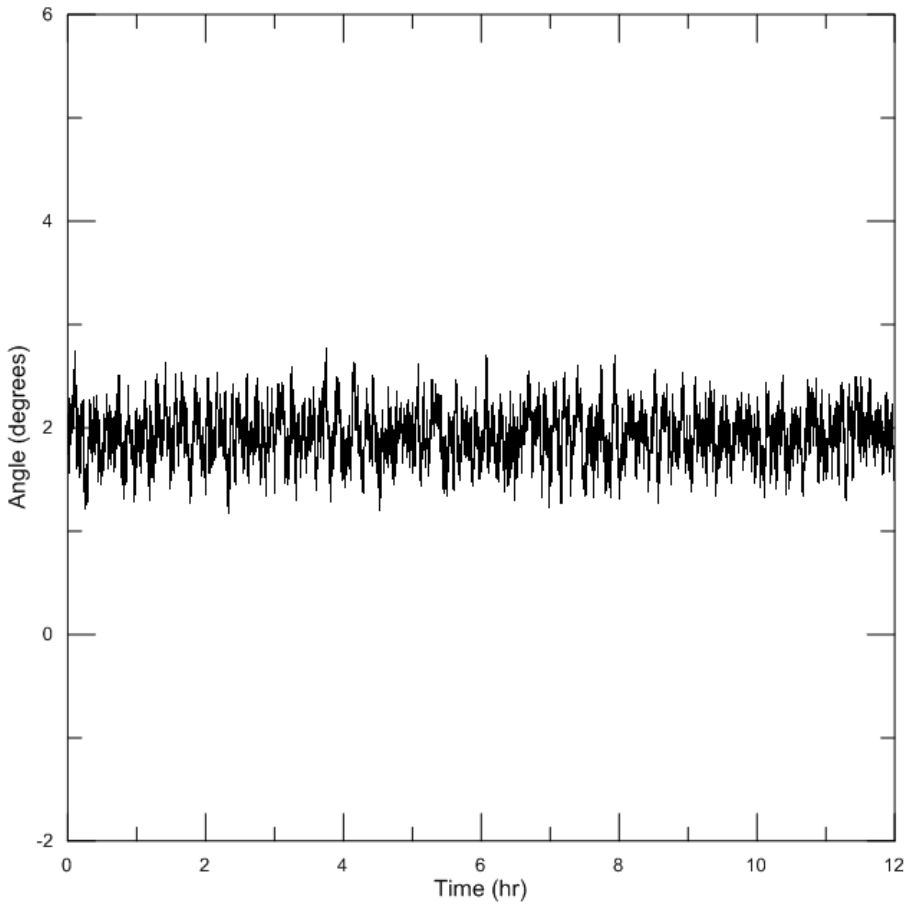

Figure 6.3 Cable A roll angle.

Table 6.6 Cable A roll angle

	Mean	SD	Min	Max	Difference
Roll Angle (deg)	1.93	0.24	1.17	2.77	1.60

In addition to the pitch and roll measurements the yaw measurements of Cable A, depicted in Fig. 6.4, are also considered. The mean of the yaw angle measurement over the measurement period is 95.01° with a standard deviation of 0.31° as shown in Table 6.7. The yaw signal varied between a maximum of 96.07° and a minimum of 95.75°. This gives a maximum difference in yaw angle measurements during the period of 2.32°. As expected, the yaw angle measurement shows a greater variation than the pitch and roll angles. This is smaller in comparison to the yaw angle measurements observed with the sensor package at rest where the maximum difference measured was 6.22°. This indicates the changes in the yaw angle measurement are within the expected variation while the sensor package is at rest.

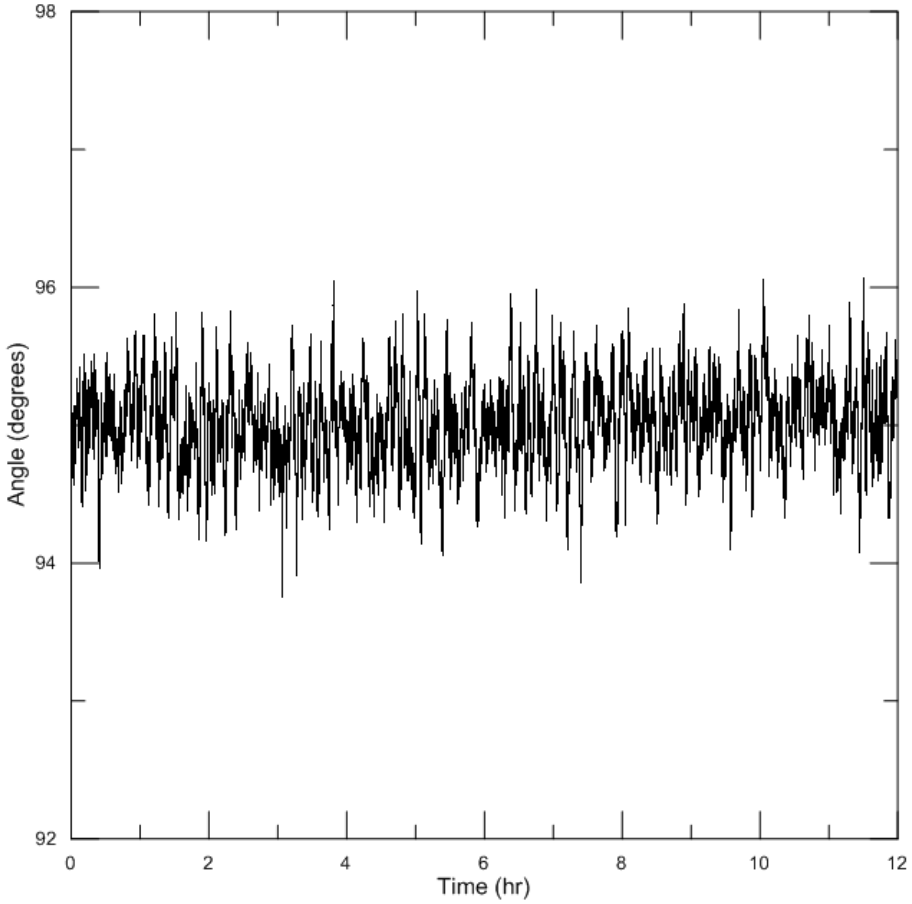

Figure 6.4 Cable A yaw angle.

Table 6.7 Cable A yaw angle

	Mean	SD	Min	Max	Difference
Yaw Angle (deg)	95.01	0.31	93.75	96.07	2.32

Measurements of acceleration and pitch, roll, and yaw angle measurements were taken from the sensor package installed in the cable abandonment termination of Cable A. The root sum acceleration measurement did not exceed the maximum changes, observed from the sensor package at rest. The pitch, roll, and yaw orientation angles also did not exceed the difference in minimum and maximum measurements. These measurements indicate that, during the data collection period, no movement of the cable abandonment termination of Cable A was measured within the accuracy of the IG-500A sensor.

The data collected from Cable A from the dates of April 25, 2015 to May 8, 2015 in Figs. 6.5 and 6.6 show measurements consistent with what was observed in the twelve hour period on April 29, 2015. There is some variation in the pitch and roll signal but it does not exceed the thresholds defined in section 5.2. No shifts in the orientation of cable abandonment termination are indicated by these measurements.

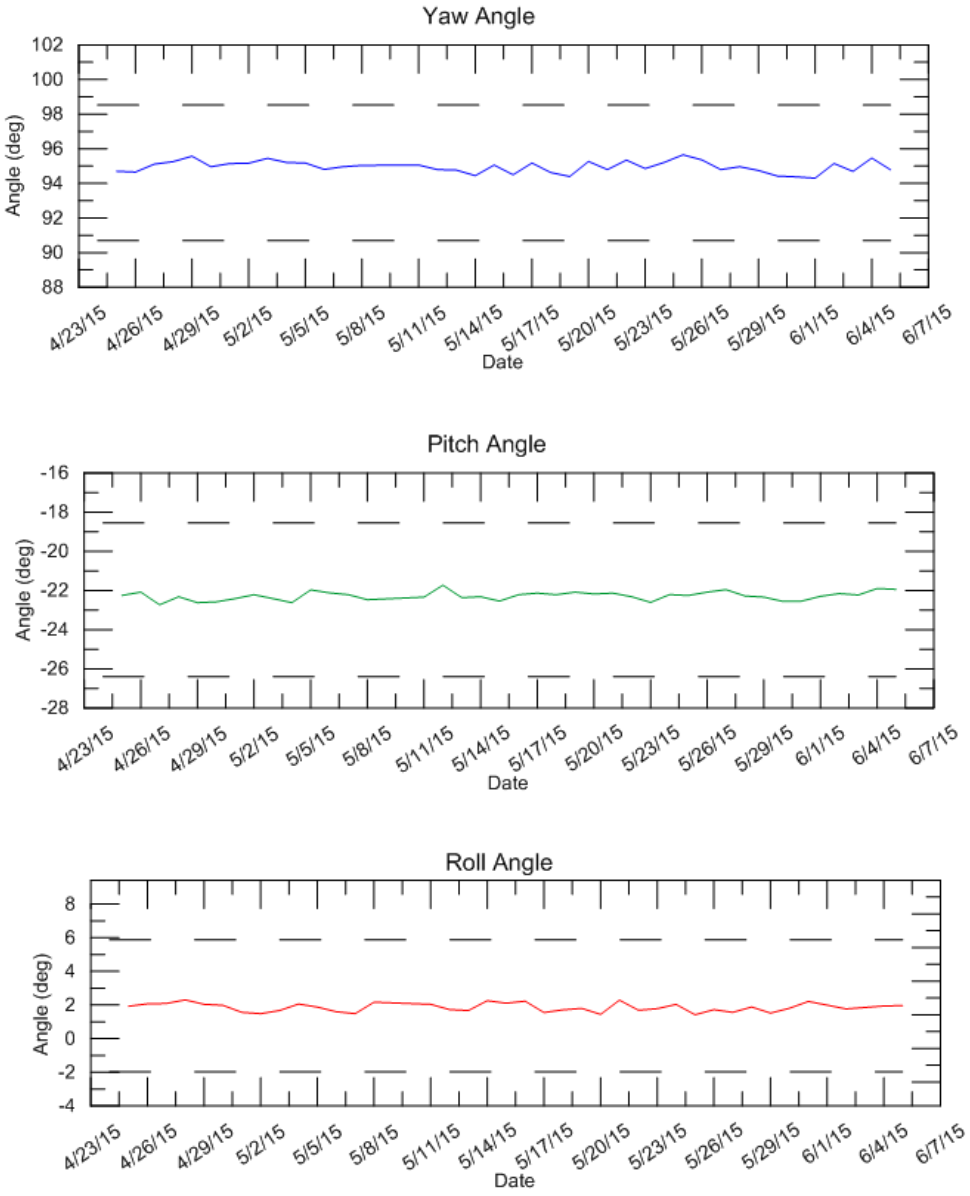

Figure 6.5 Cable A orientation angles April 25, 2015 5o May 8, 2015.

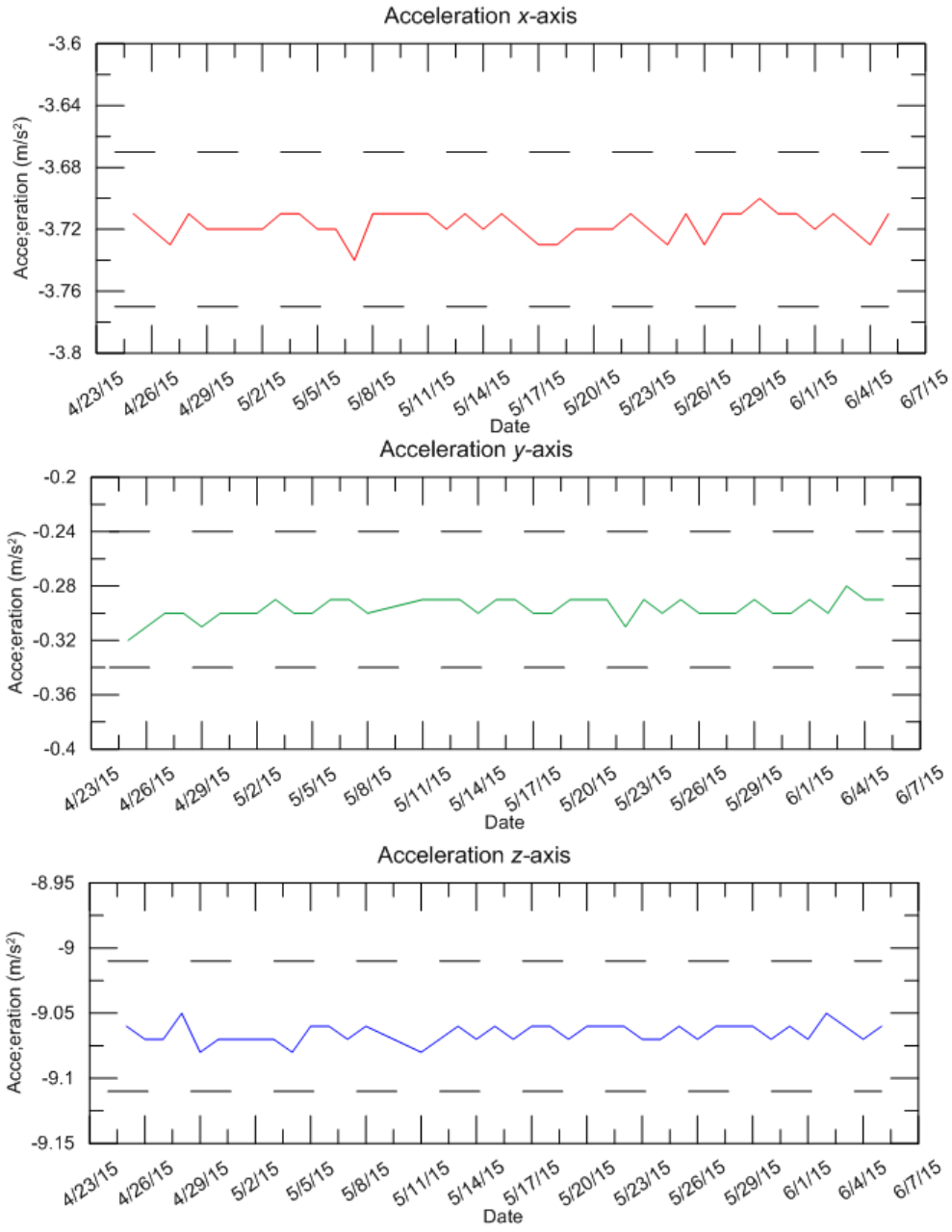

Figure 6.6 Cable A acceleration April 25, 2015 5o June 5, 2015.

The most recent data collected from Cable A on November 17, 2016 gave the values listed in Table 6.8. These values show no significant difference from the initial baseline values first measured from the Cable A sensor package and indicate that the abandonment termination is resting in the same orientation.

Table 6.8 Cable A Orientation and Accelerometer values November 17, 2015

Cable A November 17, 2015	
Roll (deg)	1.95
Pitch (deg)	-22.15
Yaw (deg)	94.79
***Ax* (m/s^2)**	-3.6992
***Ay* (m/s^2)**	-0.3099
***Az* (m/s^2)**	-9.0823

6.3. Cable C

A twelve hour period of data collected at a rate of 50 Hz from the sensor package in the abandonment termination of Cable C on April 24, 2015 is presented to characterise the behavior measured by the sensor package. The data collected between the dates of March 28, 205 to April 24, 2015 is presented to demonstrate the stability of the cable abandonment termination over a longer measurement period. The root sum acceleration signal is presented in Fig. 6.7. The mean of the measured acceleration is 9.80 m/s^2. From the values in Table 6.10, it is shown that the maximum standard deviation was observed in the *z*-axis acceleration with a value of 0.01 m/s^2. This compares below with the maximum 0.01 m/s^2 observed in the *x*-axis acceleration while the sensor package was at rest. For a sample rate of 50 Hz the RMS noise calculated from the IG-500A specification is 0.02 m/s^2. The difference in the minimum and maximum root sum acceleration is 0.06 m/s^2. These measurements indicate that there is no additional acceleration acting on the cable abandonment termination beyond gravitational acceleration.

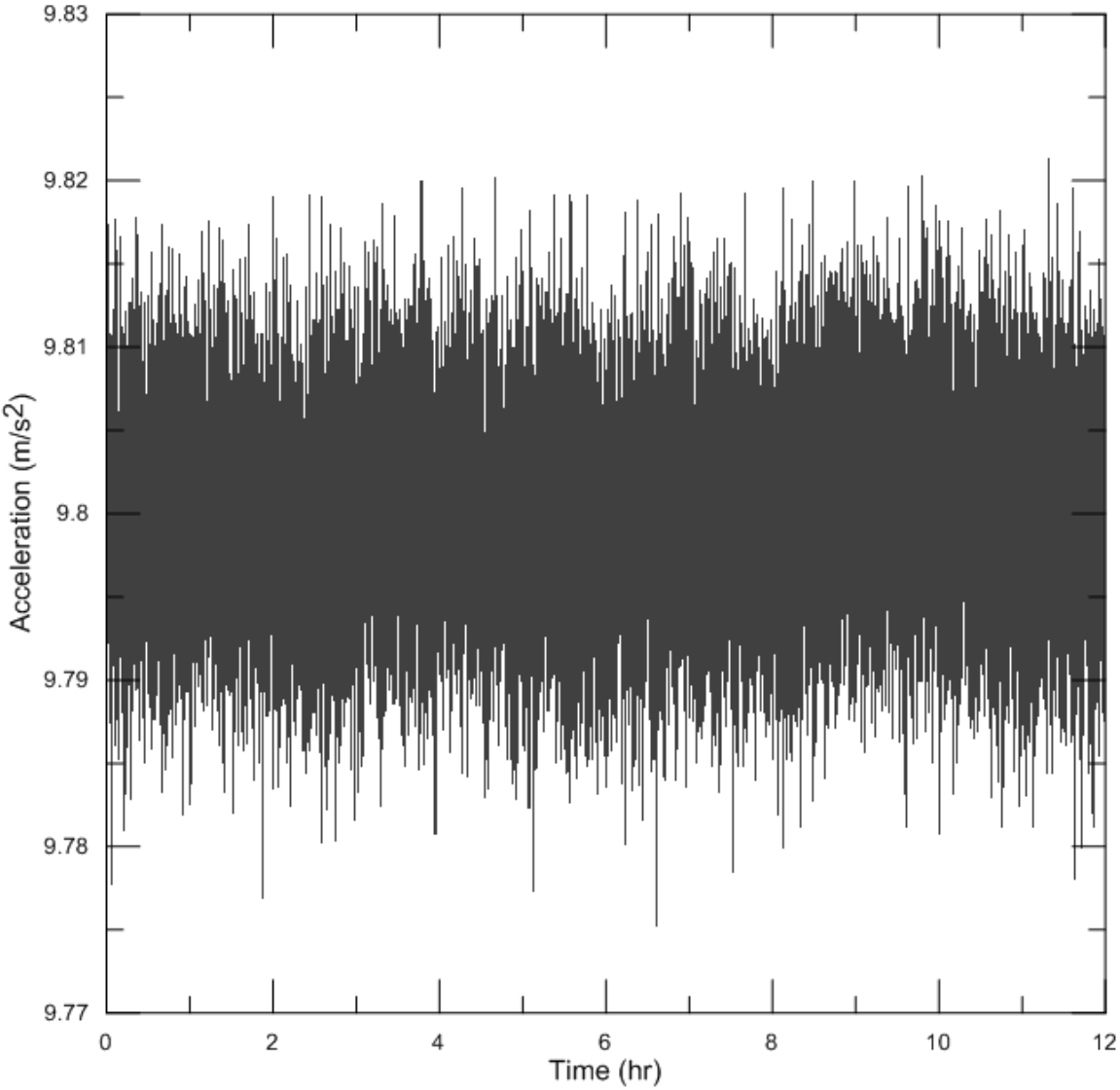

Figure 6.7 Cable C root sum acceleration.

Table 6.9 Cable C acceleration standard deviation

Standard deviation of x-axis acceleration	0.01 m/s^2
Standard deviation of y-axis acceleration	0.01 m/s^2
Standard deviation of z-axis acceleration	0.01 m/s^2
Standard deviation of root sum acceleration	0.01 m/s^2

Table 6.10 Acceleration Cable C

	Mean	**Maximum**	**Minimum**	**Difference**
x-axis acceleration	9.42 m/s^2	9.46 m/s^2	9.39 m/s^2	0.07 m/s^2
y-axis acceleration	-0.84 m/s^2	-0.81 m/s^2	-0.88 m/s^2	0.07 m/s^2
z-axis acceleration	-2.55 m/s^2	-2.52 m/s^2	-2.59 m/s^2	0.07 m/s^2
Root sum acceleration	9.80 m/s^2	9.83 m/s^2	9.77 m/s^2	0.06 m/s^2

The pitch angle of Cable C is shown in Fig. 6.8. The mean value of the pitch angle during the data collection period is 74.09° as listed in Table 6.11. The standard deviation of the collected samples is 0.13°. The signal varied between a maximum of 74.63° to a minimum of 73.57°, giving a maximum observed difference of 1.06°. From the data collected with the sensor package at rest, a maximum difference in the pitch angles measured was 2.00°. This indicates the changes in the pitch angle measurement are within the expected variation while the sensor package is at rest.

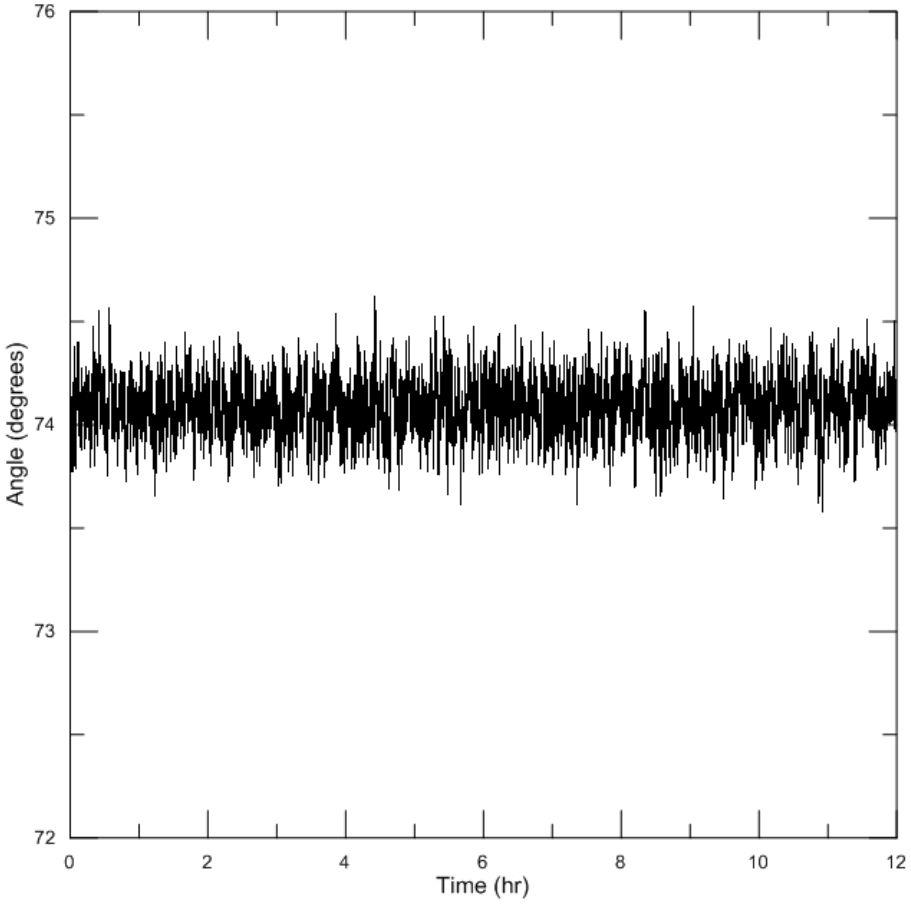

Figure 6.8 Cable C pitch angle.

Table 6.11 Cable C pitch angle values

	Mean	SD	Min	Max	Difference
Pitch Angle (deg)	74.09	0.13	73.57	74.63	1.06

The roll angle is presented in Fig. 6.9. The mean of the roll angle measurements over this time period is 18.33° with a standard deviation of 0.54° as shown in Table 6.12. The roll angle signal varied between a maximum of 20.48° and a minimum of 16.43°, giving a maximum difference of 4.04°. This difference is greater than the maximum difference of 1.70° observed while the sensor was at rest in section 5.1.1. This could indicate a change of pitch angle of the cable abandonment termination. However, it is necessary to analyse the measurements collected further to determine if this measurement is a result of a change of orientation or a result of variation in the pitch angle from the sensor. The range of the measurement over the samples collected during the twelve hour measurement period is 2.14° above the mean and 1.90° below the mean. The RMS accuracy of the sensor's pitch angle measurement is 2.0°, indicating that the maximum measurement only slightly exceeds this RMS accuracy. With a 95% confidence level the measurements can be expected to fall between ±3.92°. If the abandonment termination were shifting in pitch a change in the accelerometer signals would also be expected. However, there are no shifts in the accelerometer signals observed during the measurement period.

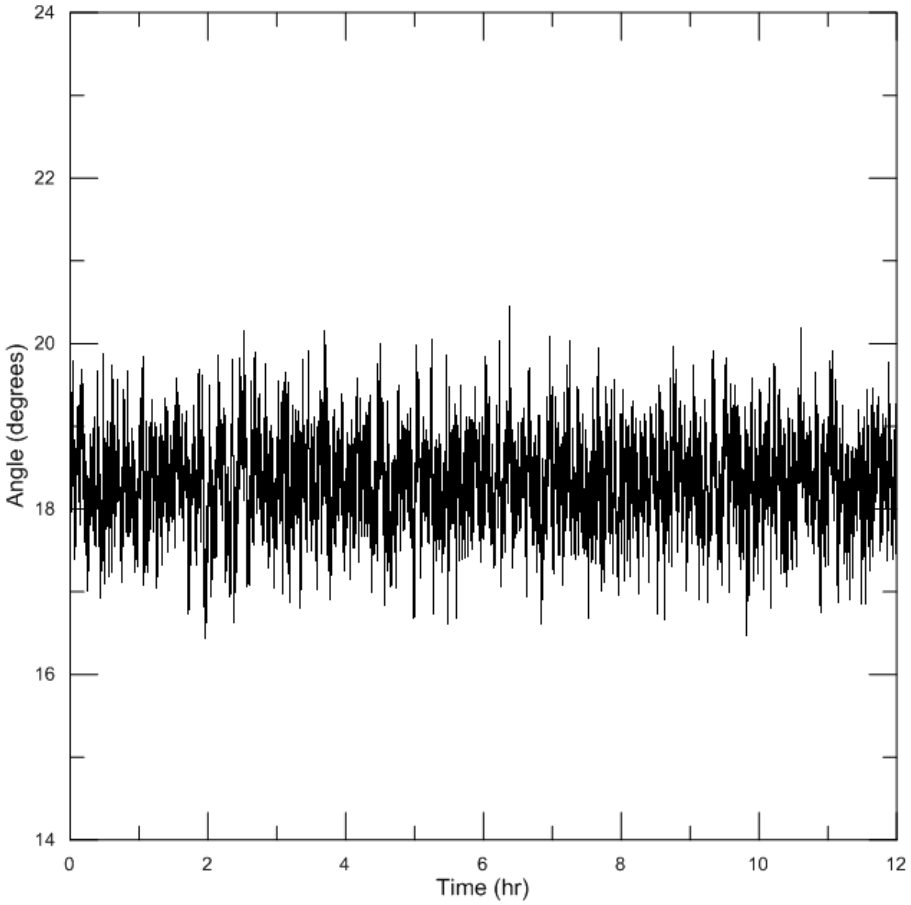

Figure 6.9 Cable C roll angle.

Table 6.12 Cable C roll angle values

	Mean	SD	Min	Max	Difference
Roll Angle (deg)	18.33	0.54	16.43	20.48	4.04

In addition to the pitch and roll measurements, the yaw measurements of Cable A, depicted in Fig. 6.10, were also considered. The mean of the yaw angle measurement over the measurement period is -107.50° with a standard deviation of 0.58° as shown in Table 6.13. The yaw signal varied between a maximum of -105.20° and a minimum of -109.66°. This gives a maximum difference in yaw angle measurements during the period of 4.45°. As expected the yaw angle measurement shows the greatest variation in comparison to the pitch and roll. This is smaller in comparison to the yaw angle measurements observed with the sensor package at rest where the maximum difference measured was 6.22°. This indicates the changes in the yaw angle measurement are within the expected variation while the sensor package is at rest.

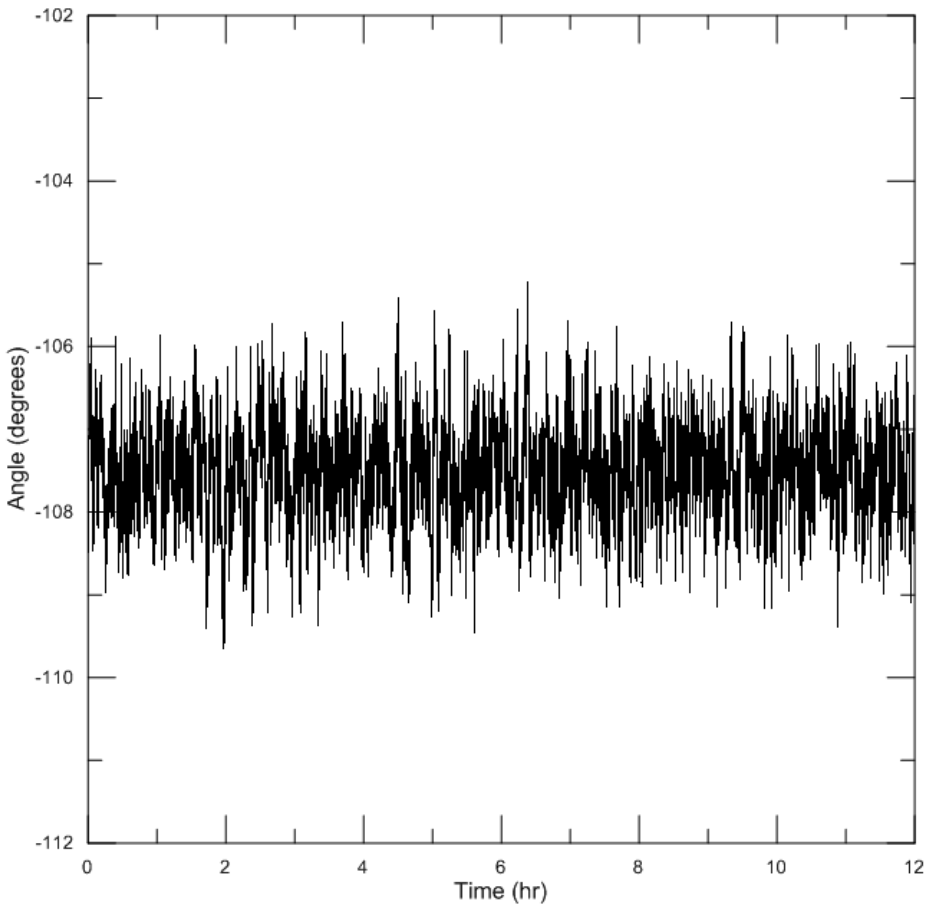

Figure 6.10 Cable C yaw angle.

Table 6.13 Cable C yaw angle values

	Mean	SD	Min	Max	Difference
Yaw Angle (deg)	-107.50	0.58	-109.66	-105.20	4.45

Within in another twelve hour period of measured data from Cable A collected on April 17, 2016, short spikes in the acceleration are measured in the data. This is likely caused by movements of gravel or cobble stones on the seabed striking the cable abandonment termination. The change of acceleration is expected based on the nature of the seabed at site C where gravel, pebbles, cobbles, and boulders are found (AECOM, 2009). When analysing the recordings made by the microphone in the sensor package occasional strikes against the abandonment termination can be heard. These changes in acceleration do not coincide with a change in the orientation measurements, as shown in Fig. 6.11. Figure 6.12 displays the same measurements in a 4 s time window at the time of the change in acceleration signal.

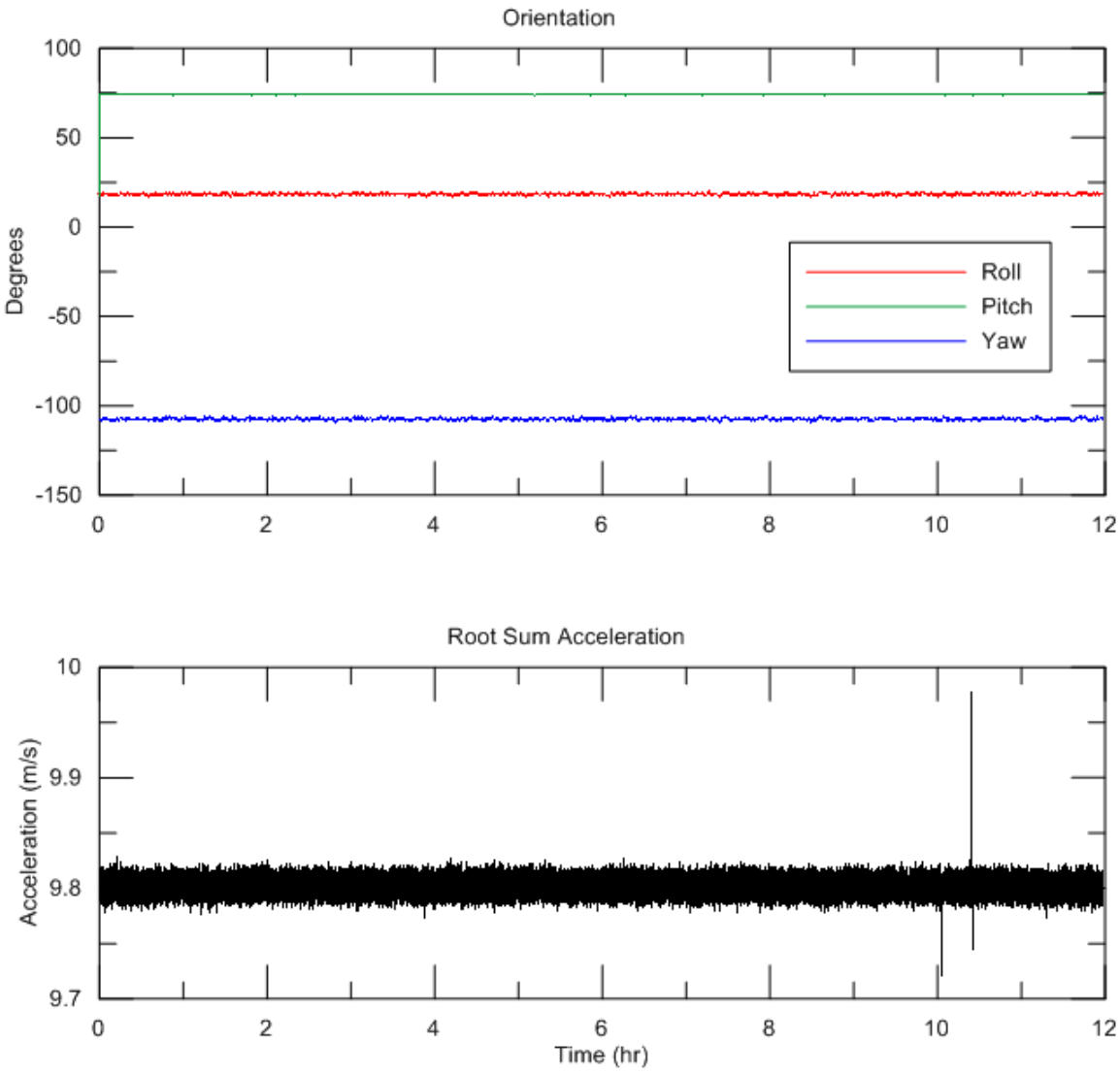

Figure 6.11 Cable C April 17, 2015 acceleration impact.

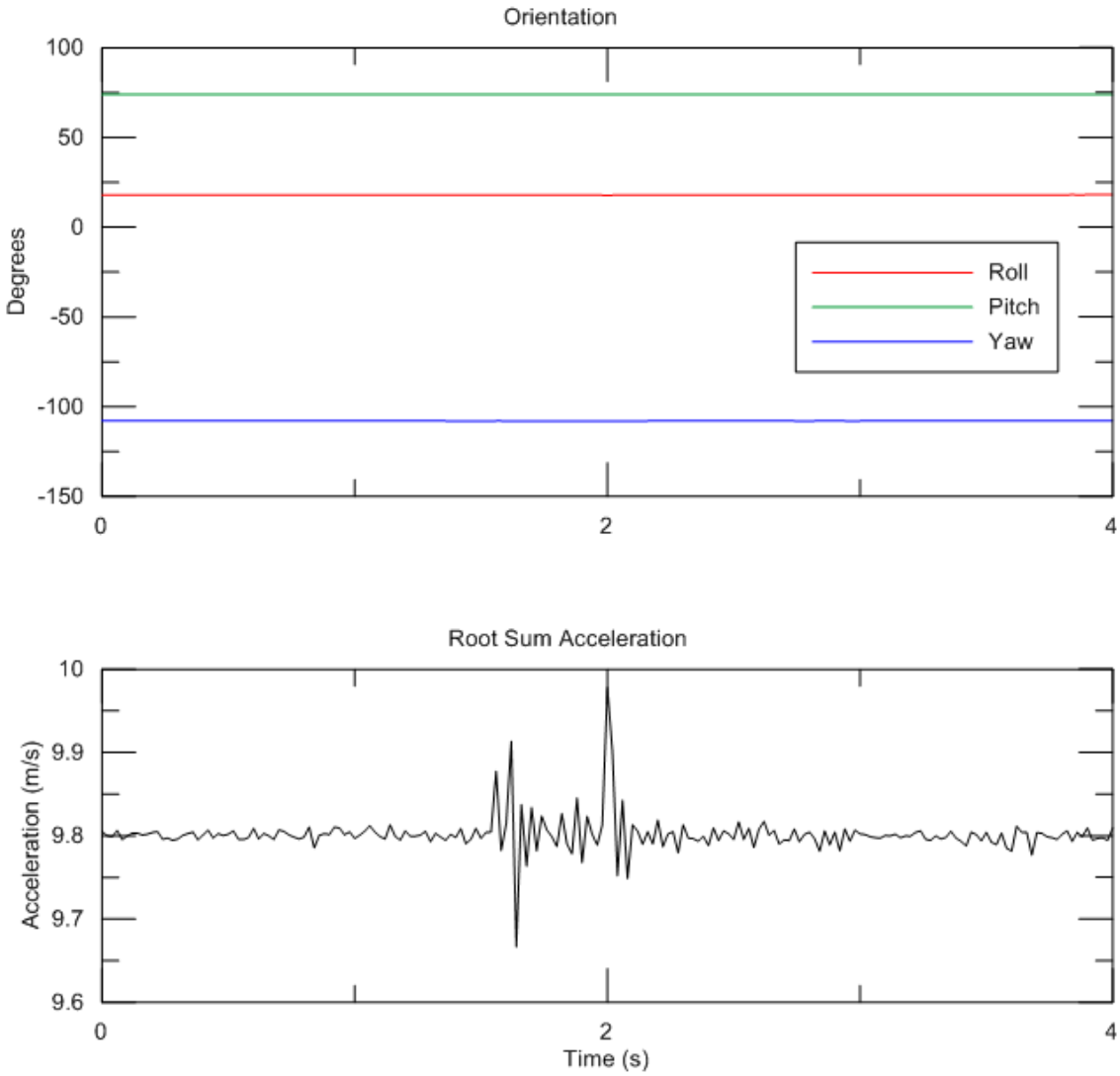

Figure 6.12 Cable C April 17, 2015 acceleration impact.

The data collected from Cable A from the dates of March 28, 2015 to April 24, 2015 in Figs. 6.13 and 6.14 show consistent measurements with what was observed in the twelve hour period. There is some variation in the roll signal but it does not exceed the thresholds defined in section 5.2. No shifts in the orientation of the cable abandonment termination are indicated by this measurement.

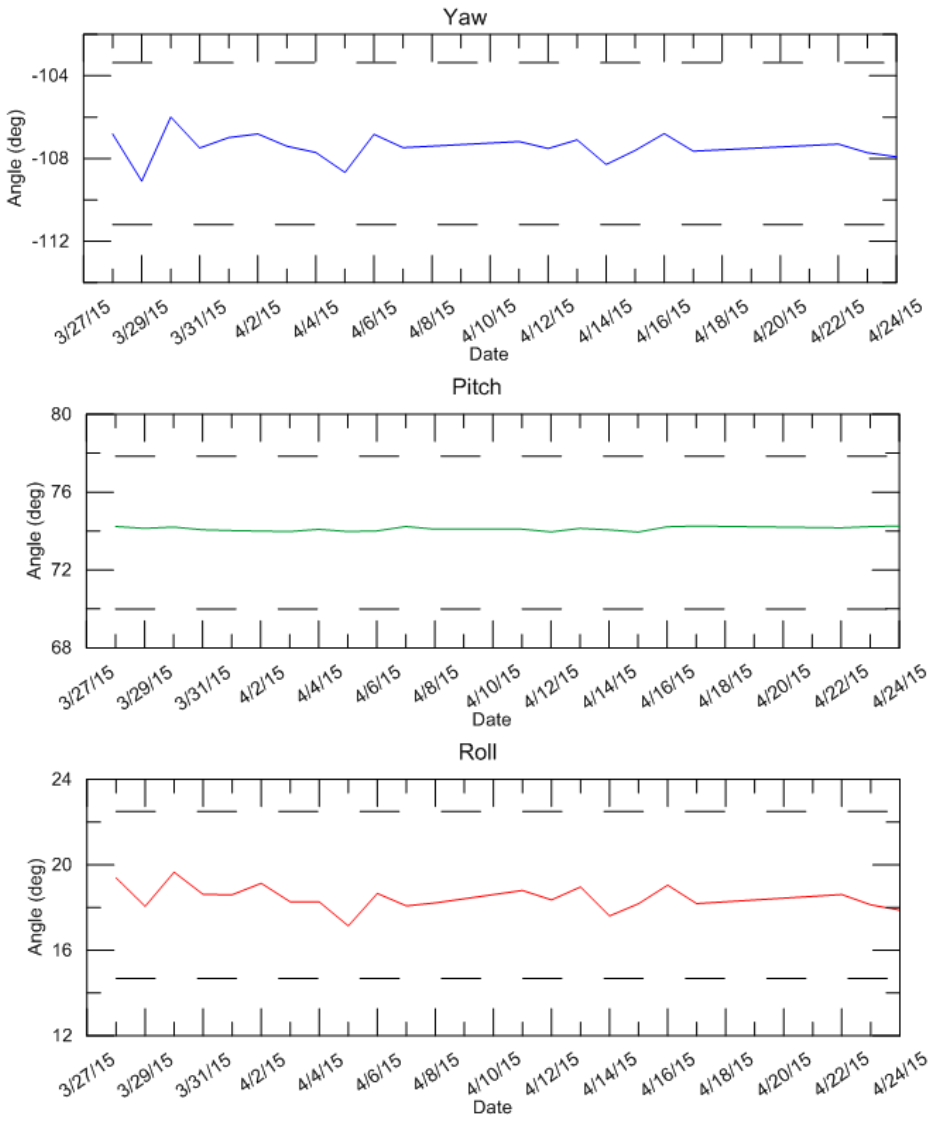

Figure 6.13 Cable C orientation measurements March 28, 205 to April 24, 2015.

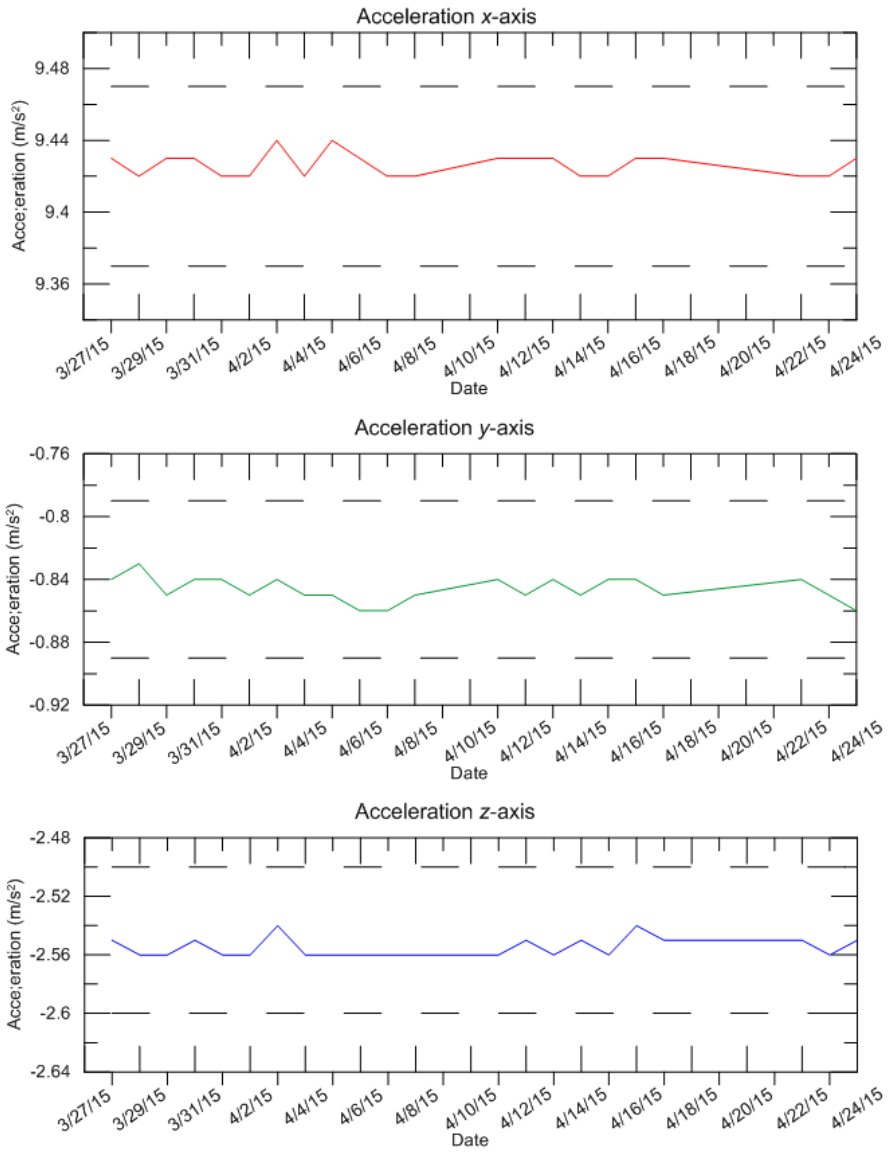

Figure 6.14 Cable C acceleration measurements March 28, 205 to April 24, 2015.

6.4. Summary

The data collected from Cable A and Cable C at the initial time of communication with the shore station unit is used as a baseline measurement for the position of the cable. Comparing data collected from each cable over a twelve hour period, no changes from the baseline measurements beyond the thresholds identified for the presence of movement from the sensor package were identified. Over a data collection period of April 25, 2015 to

June 5, 2015, the Cable A sensor package indicates that the cable abandonment termination remains in the same orientation as the initial baseline measurement recorded. Over a data collection period of March 28, 205 to April 24, 2015 the sensor package also indicates that the Cable C abandonment termination remains in the same orientation as the initial baseline measurement recorded. The baseline measurements were not collected until several months following the deployment of the cables. Therefore it is unknown whether there was movement of the either cable prior to the time when the baseline measurements were made.

Chapter 7 Conclusion and Recommendations

7.1. Conclusions

A sensor package was installed in the subsea abandonment termination of two tidal power transmission cables deployed at the FORCE tidal energy test site, located in the Minas Passage, Nova Scotia, Canada. Prior to the deployment of the cables, the sensor packages were tested in a laboratory setting. The orientation measurements were found to agree with measurements made on a rotary table and the acceleration signal was used to measure velocity of the sensor package moving along an inclined plane. These measurements were made in short periods of time. The sensor package was left at rest for 14 hours to determine the variation of the measurement made over a larger time window. Measurements in this larger period of time exhibited greater variation than observed in the smaller time period due to bias instability from the AHRS sensor.

The measurements from the sensor package installed in the cable abandonment terminations of the FORCE subsea transmission cables A and C indicate that the terminations are stable on the seabed. These measurements are limited to the accuracy of the AHRS sensor that was used. Detecting smaller shifts in the orientation would require a sensor with a finer orientation accuracy and bias stability. However, it can be concluded that no orientation shifts beyond the accuracy of the AHRS sensor were recorded. No shifts in the orientation measurements coinciding with changes in the acceleration measurements for either the Cable A or C abandonment terminations that indicate mobility of either cable abandonment terminations on the seabed were recorded. Some accelerometer measurements were made that indicate impacts made to the Cable A abandonment termination by materials moving along the seabed. Audio files collected from the microphone included in the sensor package also recorded impacts to the Cable A abandonment termination. However, these acceleration measurements were not shown to coincide with shifts in the orientation signals of the sensor.

The sensor packages in either cable abandonment termination were not communicated with until several months after the deployment of the cables. Therefore, it is unknown whether movement of the cable abandonment terminations occurred in this time. It is possible that

movement of the abandonment terminations occurred in this time window before settling into a stable position on the seabed when regular measurement from the sensor packages began.

A sensor package containing an AHRS was shown to offer a method to measure the orientation and accelerations which may occur due to movement or impacts of the FORCE cable abandonment terminations. However, this is limited in only providing information at the location of the sensor. The use of a sensor in the abandonment termination of the cables is limited as it only indicates the stability of the abandonment termination itself. This does not determine the stability of the cable along the complete length of its run from the shore to the tidal turbine berth location.

7.2. Recommendations

It is recommended that FORCE continue to monitor the cable abandonment terminations at the berth sites before they are connected to deployed tidal turbines. This will allow FORCE to continue to ensure the stability of the cable ends and analyse the collected data under varying annual and seasonal conditions. Further surveying by ROV to assess wear to the cable abandonment terminations that may have occurred from movement at the time elapsed between deployment of the cables to the tidal berths and data collection from the abandonment termination sensor packs.

The sensor package is limited in that it only tracks the seabed stability of the abandonment terminations of the two instrumented cables. It is important to monitor the stability and condition of the subsea transmission cables along the entire length. Vibrations that occur at the contact points of cable suspensions are a likely source of wear for subsea cables. Understanding how cables wear due to the environment is important in the assessment of the life cycle for subsea transmission cables. Distributed fiber optic sensors could be used to monitor strain along the entire length of the subsea transmission cables at the FORCE site.

This research was primarily focused on the data collected from the AHRS sensor included in the cable abandonment termination sensor packages and made limited use of the data

collected from the microphone. Further analysis of the data collected by the microphone included in the sensor packages could be used to better understand the transport of materials along the seabed at the tidal berth sites and around the cable abandonment terminations.

Bibliography

AECOM (2009). Environmental Assessment Registration Document – Fundy Tidal Energy Demonstration Project Volume I: Environmental Assessment. Halifax, NS, Canada, AECOM Canada Ltd.

Amara-Madi, S., C. A. Price, et al. (2013). Autonomous sensor system for deep-sea pipeline monitoring. 2013 IEEE 11th International New Circuits and Systems Conference, NEWCAS 2013, June 16, 2013 - June 19, 2013, Paris, France, IEEE Computer Society.

Andreassen, J. S. and J. Vlekken (2005). Fibre Bragg gratings in cables for remotely operated vehicles. 17th International Conference on Optical Fibre Sensors, OFS-17, May 23, 2005 - May 27, 2005, Bruges, Belgium, SPIE.

Bland, M. J. and D. G. Altman (1986). "Statistical methods for assessing agreement between two methods of clinical measurement." The Lancet **327**(8476): 307-310.

Bourke, A. K., J. V. O'Brien, et al. (2007). "Evaluation of a threshold-based tri-axial accelerometer fall detection algorithm." Gait \& Posture **26**(2): 194-199.

Bourke, A. K., P. Van De Ven, et al. (2010). Assessment of waist-worn tri-axial accelerometer based fall-detection algorithms using continuous unsupervised activities. 2010 32nd Annual International Conference of the IEEE Engineering in Medicine and Biology Society, EMBC'10, August 31, 2010 - September 4, 2010, Buenos Aires, Argentina, IEEE Computer Society.

Brower, D., J. D. Hedengren, et al. (2012). Fiber optic monitoring of subsea equipment. ASME 2012 31st International Conference on Ocean, Offshore and Arctic Engineering, OMAE 2012, July 1, 2012 - July 6, 2012, Rio de Janeiro, Brazil, American Society of Mechanical Engineers.

Chao, P.-K., H.-L. Chan, et al. (2009). "A comparison of automatic fall detection by the cross-product and magnitude of tri-axial acceleration." Physiological Measurement **30**(10): 1027.

Correia, M. D. and A. C. Matod (2003). A high performance IMU based navigation system for a small size ROV. Celebrating the Past... Teaming Toward the Fututre, September 22, 2003 - September 26, 2003, San Diego, CA., United states, Institute of Electrical and Electronics Engineers Inc.

Earle, M. D., J. C. Cranford, et al. (1998). Hand-deployable wave buoy utilizing triaxial accelerometer, angular rate, and magnetometer sensors. Proceedings of the 1997 3rd International Symposium on Ocean Wave Measurement and Analysis, WAVES, November 3, 1997 - November 7, 1997, Virginia Beach, VA, USA, ASCE.

EMEC (2015). PFOW Enabling Actions Project: Sub-sea Cable Lifecycle Study, The Crown Estate.

Fromme, M., W. Christiansen, et al. (2011). Distributed temperature monitoring of long distance submarine cables. 21st International Conference on Optical Fiber Sensors, May 15, 2011 - May 19, 2011, Ottawa, ON, Canada, SPIE.

Google Earth V 7.1.2.2041. (December 15, 2015). Bay of Fundy, NS, Canada. 45° 14' 45.90"N, 63° 51' 52.04"W, Eye alt 730 m. Data SIO, NOAA, US Navy, NGA, GEBCO. Image Landsat Data LDEO-Colombia, NSF, NOAA [November 11, 2016].

Heo, Y., G.-H. Lee, et al. (2012). EKF-based localization for the underwater structure inspection robot using depth sensor and IMU. 2012 9th International Conference on Ubiquitous Robots and Ambient Intelligence, URAI 2012, November 26, 2012 - November 29, 2012, Daejeon, Korea, Republic of, IEEE Computer Society.

Hwang, A., S. Yoon, et al. (2011). Performance evaluation of AHRS based MEMS for unmanned underwater vehicle. 21st International Offshore and Polar Engineering Conference, ISOPE-2011, June 19, 2011 - June 24, 2011, Maui, HI, United states, International Society of Offshore and Polar Engineers.

Jiang, Q. and Q. Sui (2009). Technological study on distributed fiber sensor monitoring of high voltage power cable in seafloor. 2009 IEEE International Conference on Automation and Logistics, ICAL 2009, August 5, 2009 - August 7, 2009, Shenyang, China, IEEE Computer Society.

Jin, W.-L., J.-W. Shao, et al. (2003). Basic strategy of health monitoring on submarine pipeline by distributed optical fiber sensor. 22nd International Conference on Offshore Mechanics and Arctic Engineering; Safety and Reliability Pipeline Technology, June 3, 2001 - June 13, 2001, Cancun, Mexico, American Society of Mechanical Engineers.

Jones, K., C. Staveley, et al. (2014). Condition monitoring of a subsea pump using fibre optic sensing. 23rd International Conference on Optical Fibre Sensors, June 2, 2014 - June 6, 2014, Santander, Spain, SPIE.

Joordens, M., J. Serna, et al. (2008). "Low cost underwater robot sensor suite." 2008 IEEE International Conference on System of Systems Engineering, SoSE 2008.

Kangas, M., A. Konttila, et al. (2008). "Comparison of low-complexity fall detection algorithms for body attached accelerometers." Gait & Posture **28**(2): 285-291.

Karsten, R. H., J. M. McMillan, et al. (2008). "Assessment of tidal current energy in the Minas Passage, Bay of Fundy." Proceedings of the Institution of Mechanical Engineers, Part A: Journal of Power and Energy **222**(5): 493-507.

Kennedy, D., M. Walsh, et al. (2015). Development of a miniature, low-cost wave measurement solution. 2014 Oceans - St. John's, OCEANS 2014, September 14, 2014 - September 19, 2014, St. John's, NL, Canada, Institute of Electrical and Electronics Engineers Inc.

King, D. and S. Ukani (2011). "Structural integrity monitoring of subsea systems." Measurement and Control (United Kingdom) **44**(7): 212-216.

Kurashima, T., T. Horiguchi, et al. (1991). "Design and sea trial results of a 48-fiber submarine optical fiber cable." Electronics and Communications in Japan, Part I: Communications (English translation of Denshi Tsushin Gakkai Ronbunshi) **74**(11): 76-87.

Mufti, A. (2009). Installation, Use and Repair of Fibre Optic Sensors. Winnipeg, Manitoba, Canada, ISIS Canada Corporation.

Nishimoto, T., T. Miyahara, et al. (1995). "Development of 66kv Xlpe Submarine Cable Using Optical-Fiber as a Mechanical Damage Detection Sensor." Ieee Transactions on Power Delivery **10**(4): 1711-1717.

Ohno, H., H. Naruse, et al. (2001). "Industrial Applications of the BOTDR Optical Fiber Strain Sensor." Optical Fiber Technology **7**(1): 45-64.

Roberts, D. (2007). Subsea pipeline monitoring using fibre optic strain sensors. 26th International Conference on Offshore Mechanics and Arctic Engineering 2007, OMAE2007, June 10, 2007 - June 15, 2007, San Diego, CA, United states, American Society of Mechanical Engineers.

SBG Systems (2012). IG-500A Sub-miniature AHRS User Manual. 3bis, chemin de la Jonchère 92500 Rueil Malmaison France, SBG Systems**:** 62.

Seaforth Geosurveys (2015). FORCE Submarine Power Cables Detailed As-Found Positions. Halifax, NS, FORCE.

Steele, K. E., D. W. Wang, et al. (1998). "Buoy pitch and roll computed using three angular rate sensors." Coastal Engineering **35**(1-2): 123-139.

Svoma, R., C. Smith, et al. (2009). Integrated condition monitoring for subsea power cable systems. 20th International Conference and Exhibition on Electricity Distribution, CIRED 2009, June 8, 2009 - June 11, 2009, Prague, Czech republic, Institution of Engineering and Technology.

Tarbotton, M. and M. Larson (2006). Canada Ocean Energy Atlas (Phase 1) Potential Tidal Current Energy Resources Analysis Background Triton Consultants Ltd.

Tayama, H., O. Fukuda, et al. (1995). "6.6kv Xlpe Submarine Cable with Optical-Fiber Sensors to Detect Anchor Damage and Defacement of Wire Armor." Ieee Transactions on Power Delivery **10**(4): 1718-1723.

Thivend, G. (2010). Subsea sensors for non-intrusive monitoring of temperature, pressure and asset integrity. Offshore Technology Conference 2010, OTC 2010, May 3, 2010 - May 6, 2010, Houston, TX, United states, Offshore Technology Conference.

Williams, A. J., A. T. Morrison, et al. (2013). Vector averaging in a wave field. OCEANS 2013 MTS/IEEE Bergen: The Challenges of the Northern Dimension, June 10, 2013 - June 13, 2013, Bergen, Norway, IEEE Computer Society.

Zhang, Q. B., G. H. Tian, et al. (2013). "A Fall Detection Study Based on Neural Network Algorithm Using AHRS." 2013 Ieee International Conference on Information and Automation (Icia): 773-779.

Zhao, L., Y. Li, et al. (2014). "On-line monitoring system of 110 kV submarine cable based on BOTDR." Sensors and Actuators, A: Physical **216**: 28-35.

Zhao, X.-F., L. Li, et al. (2012). "Scour monitoring system of subsea pipeline using distributed Brillouin optical sensors based on active thermometry." Optics and Laser Technology **44**(7): 2125-2129.

Appendix A MATLAB Code

```
%Find number of data poinrs
n = size(time);

%Rotation matrix from quaternions
for i = 1:n

    rotm(:,:,i) = [2*(quatW(i)^2)+2*(quatX(i)^2)-1,
(2*quatX(i)*quatY(i))-(2*quatW(i)*quatZ(i)),
(2*quatW(i)*quatY(i))+(2*quatX(i)*quatZ(i));
                   (2*quatX(i)*quatY(i))+(2*quatW(i)*quatZ(i)),
2*(quatW(i)^2)+2*(quatY(i)^2)-1, (2*quatY(i)*quatZ(i))-
(2*quatW(i)*quatX(i));
                   (2*quatX(i)*quatZ(i))-(2*quatW(i)*quatY(i)),
(2*quatY(i)*quatZ(i))+(2*quatW(i)*quatX(i)),
2*(quatW(i)^2)+2*(quatZ(i)^2)-1];
end

%Angle of sensor y-axis
posy = [0;1;0];

%Transfrom to earth reference frame
eposy = rotm(:,:,1)*posy;


%Projection of vector to earth xy-plane
eposgg = eposy - dot(eposy,[0;0;1])*[0;0;1];
eposgg = eposgg/norm(eposgg);

%Angle between vectors
angtoy = acosd(dot(eposy,eposgg));

%Moving Averages

rollmv = conv(roll', ones(1,10), 'valid');
rollmv = rollmv/10;

pitchmv = conv(pitch', ones(1,10), 'valid');
pitchmv = pitchmv/10;

yawmv = conv(yaw', ones(1,10), 'valid');
yawmv = yawmv/10;

accelXmv=conv(accelX, ones(1,10), 'valid');
accelXmv=accelXmv/10;

accelYmv=conv(accelY, ones(1,10), 'valid');
accelYmv=accelYmv/10;

accelZmv=conv(accelZ, ones(1,10), 'valid');
accelZmv=accelZmv/10;
```

```
%Multiply acceleration by rotation matrix to transform to earth frame
%{
for i = 1:n
    accel(i,:) = [accelX(i) accelY(i) accelZ(i)];
end
%}

%{
for i = 1:n
    accelearth(i,:) = (rotm(:,:,i)*accel(i,:)')';
end
%}

%Baseline measurements for Cable A

bslaccelX = -3.7225;
bslaccelY = -0.2947;
bslaccelZ = -9.0635;
bslroll = 1.95;
bslpitch = -22.48;
bslyaw = 94.61;
accelplm = .05;
angleplm = 3.92;

for i=1:n
    if (accelXmv(i) > (bslaccelX + accelplm)) | (accelXmv(i) <
(bslaccelX - accelplm))
        disp('accelX at ')
        disp(time(i))
        break
    end
end

for i=1:n
     if (accelYmv(i) > (bslaccelY + accelplm)) | (accelYmv(i) <
(bslaccelY - accelplm))
        disp('accelY at ')
        disp(time(i))
        break
     end
end

for i=1:n
     if (accelZmv(i) > (bslaccelZ + accelplm)) | (accelZmv(i) <
(bslaccelZ - accelplm))
        disp('accelZ at ')
        disp(time(i))
        break
     end
end

for i=1:n
     if (rollmv(i) > (bslroll + angleplm)) | (rollmv(i) < (bslroll -
angleplm))
```

```
        disp('roll at ')
        disp(time(i))
        break
    end
end

for i=1:n
     if (pitchmv(i) > (bslpitch + angleplm)) | (pitchmv(i) < (bslpitch
- angleplm))
        disp('pitch at ')
        disp(time(i))
        break
    end
end

or i=1:n
     if (yawmv(i) > (bslyaw + angleplm)) | (yawmv(i) < (bslyaw -
angleplm))
        disp('yaw at ')
        disp(time(i))
        break
    end
end
```

Appendix B Copyright Permission

17/11/2016

I am preparing my Masters of Applied thesis for submission to the Faculty of Graduate Studies at Dalhousie University, Halifax, Nova Scotia, Canada. I am seeking your permission to include following material in the thesis:

From the IG-500A Sub-miniature AHRS User Manual:
Figure 12: 3D Accelerometer physical location in box version.
8.2.1. Mechanical outline

Canadian graduate theses are reproduced by the Library and Archives of Canada (formerly National Library of Canada) through a non-exclusive, world-wide license to reproduce, loan, distribute, or sell theses. I am also seeking your permission for the material described above to be reproduced and distributed by the LAC(NLC). Further details about the LAC(NLC) thesis program are available on the LAC(NLC) website (www.nlc-bnc.ca).

Full publication details and a copy of this permission letter will be included in the thesis.

Yours sincerely,

Sean Campbell

Permission is granted for:

a) the inclusion of the material described above in your thesis.

b) for the material described above to be included in the copy of your thesis that is sent to the Library and Archives of Canada (formerly National Library of Canada) for reproduction and distribution.

Name: Christophe Nicolopoulos Title: Senior Field Application Engineer

Signature: [redacted] Date: November 17 2016